Efficient PEM fuel cells for portable applications

Zhenxiao Chen

Supervised by

Prof. Mohammed Pourkashanian

Prof. Lin Ma

Dr. Kevin Hughes

Dr. Mohammed Ismail

A thesis submitted to the University of Sheffield in partial fulfilment of the requirement for the degree of Master of Philosophy

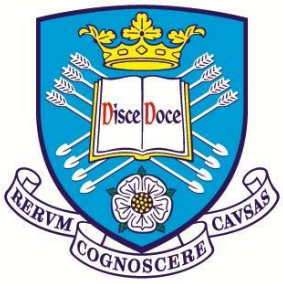

Department of Mechanical Engineering

University of Sheffield

January 2019

Declaration

The candidate confirms that the work submitted is his own, except where work which has formed part of jointly authored publications has been included. The contribution of the candidate and the other authors to this work has been explicitly indicated below. The candidate confirms that appropriate credit has been given within the thesis where reference has been made to the work of others.

The work in Chapter 4 of the thesis has been published in *Journal of the Energy Institute*, and the work in Chapter 3 of the thesis has been accepted for publication in *International Journal of Numerical Methods for Heat and Fluid Flow*.

I developed the fuel cell models and conducted all the experimental and modelling work. My supervisors, Dr Mohammed Ismail, Prof Derek Ingham, Prof Lin Ma, Dr Kevin Hughes and Prof Mohammed Pourkashanian helped me improve the models, provided helpful suggestions for my research and helped revise the paper drafts.

Acknowledgements

First and foremost, I would like to express my deepest appreciation to my supervisors, Dr Mohammed Ismail, Prof Derek Ingham, Prof Lin Ma, Dr Kevin Hughes and Prof Mohammed Pourkashanian for their patience and guidance. Special thanks to Dr Mohammed Ismail, who provided me with helpful advices on my research. I am also grateful to the senior technician, Dmitry Govorukhin, who gave me many practical suggestions and guidance in the lab. I also had great pleasure of working with other members in our research group.

Many thanks to my parents and family, who have always been there for me and helped me through difficult times.

Publications from this thesis

Publications in scientific journals

Z.X. Chen, D.B. Ingham, M.S. Ismail, L. Ma, K.J. Hughes, M. Pourkashanian. Dynamics of liquid water in the anode flow channels of PEM fuel cells: A numerical parametric study. *Journal of the Energy Institute* (In press, 2018).

Z.X. Chen, D.B. Ingham, M.S. Ismail, L. Ma, K.J. Hughes, M. Pourkashanian. Effects of hydrogen relative humidity on the performance of an air-breathing PEM fuel cell: a numerical study. *International Journal of Numerical Methods for Heat and Fluid Flow* (Accepted for publication, 2019).

Abstract

Fuel cells (FCs) have attracted considerable attention for replacing batteries in many electronic devices. Among different types of fuel cells, the proton exchange membrane fuel cell (PEMFC) is most widely investigated. Air-breathing proton exchange membrane fuel cells (AB-PEMFCs) have received more attention in recent years because of the simplifications in the fuel cell system, which makes it a good choice for portable applications. However the simplifications also causes a rather low performance and this is attributed to the low mass and heat transfer coefficients. In this thesis, a mathematical model has been developed in order to investigate the overall performance of the fuel cell system, and the local performances of two important components, i.e. the gas channel (GC) and gas diffusion layer (GDL) have been studied by a CFD model and a gas permeability experiment, respectively.

The mathematical model presented in this thesis is based on the conservation of the mass and heat transfer in order to investigate the effects of the different parameters on the fuel cell overall performance. A new revised water transport relation is applied in this model, which makes it possible to study the effect of the hydrogen relative humidity (RH). The results show that, among all the different operating parameters, the hydrogen RH can significantly improve the performance of AB-PEMFCs and the GDL is an important component in improving the transport and water management issues.

In addition, a computational fluid dynamics (CFD) model for the anode channels in AB-PEMFCs is developed by employing the Volume of Fluid (VOF) method. The dynamics of the liquid water are studied under different flooding conditions. The modelling results show that the initial position of the accumulated droplet and the hydrogen velocity have little effect while the droplet size and the channel wettability can largely influence the local performance in the channels, e.g. the water removal time and the pressure drop. Also it is found that the trade-off between the pressure drop and the removal time should be considered when designing practical products.

Further, the GDL thickness is found to be important in determining the performance of the AB-PEMFCs in the modelling work. In order to produce the GDLs with different thicknesses, an experimental investigation has been conducted to study the effect of the stacking of single GDL layers, and the through-plane gas permeability is investigated, which is one of the most important properties of GDLs. Compared with previous studies, the gas permeability of the GDL stacks is investigated instead of a single GDL layer. The calculation results show that the stacking of layers has only a small influence on the overall gas permeability of the GDL stack. In addition, a tighter contact between each layer in the GDL stacks is found to increase the overall gas permeability of the GDL stacks.

Contents

List of figures

List of tables

Nomenclature

Abbreviations

AAEMFC	alkaline anion exchange membrane fuel cell
AB-PEMFC	air-breathing proton exchange membrane fuel cell
AFC	alkaline fuel cell
BEV	battery electric vehicle
CC	current collector
CCM	catalyst-coated membrane
CFD	computational fluid dynamics
CHP	combined heat and power
CL	catalyst layer
CSF	continuum surface force
DEFC	direct ethanol fuel cell
DMFC	direct methanol fuel cell
FC	fuel cell
FCEV	fuel cell electric vehicle
GC	gas channel
GDL	gas diffusion layer
GDM	gas diffusion media
LB	Lattice Boltzmann
M^2	multi-phase mixture
MCFC	molten-carbonate fuel cell
MEA	membrane electrode assembly
MFC	microbial fuel cell
MPL	microporous layer
MRI	Magnetic Resonance Imaging
NG	natural gas

OCV	open circuit voltage
PAFC	phosphoric acid fuel cell
PEM	proton exchange membrane
PEMFC	proton exchange membrane fuel cell
PH	potential of hydrogen
PN	pore-network
PTFE	polytetrafluoroethylene
RH	relative humidity
RRPS	remote-region power supply
SOFC	solid-oxide fuel cell
TEG	thermal expandable graphite
VOF	volume of fluid
μDMFC	micro direct methanol fuel cell

Roman alphabet

a	water activity	-
A	active area of fuel cell	m^2
C	molar concentration	mol m^{-3}
D	diffusion coefficient	m^2 s^{-1}
e	emissivity	-
E	cell voltage	V
E_o	thermodynamic equilibrium voltage	V
F	Faraday's constant	C mol^{-1}
$\vec{F}$	momentum source term	N m^{-3} s^{-1}
g	magnitude of gravitational acceleration	m s^{-2}
h	hear transfer coefficient	W m^{-2} K^{-1}
h_m	mass transfer coefficient	mol s^{-1}
H	enthalpy	kJ mol^{-1}

I	current density	A m^{-2}
I_o	exchange current density	A m^{-2}
j_w	water flux	mol m^{-2} s^{-1}
k	thermal conductivity	W m^{-1} K^{-1}
K	permeability	m^2
L	characteristic length	m
M	molecular weight	g mol^{-1}
n	number of electrons per mole of species of interest	mol^{-1}
$\vec{n}$	surface normal	-
n_d	electro-osmotic coefficient	-
N	molar flux	mol m^{-2} s^{-1}
Nu	Nusselt number	-
P	pressure	Pa
P_{sat}	saturation pressure of water vapour	Pa
q	heat flux	W m^{-2}
R	universal gas constant	J mol^{-1} K^{-1}
Ra	Rayleigh number	-
RH	relative humidity	%
R_{elec}	electrical resistance	Ω
R_{mem}	ionic resistance of membrane	Ω
S	entropy	J mol^{-1} K^{-1}
Sh	Sherwood number	-
$\vec{t}$	surface tangent	-
T	temperature	K
$\vec{u}$	velocity	m s^{-1}
x	molar fraction	-

Greek alphabet

α	thermal diffusivity	$m^2\ s^{-1}$
α_{ch}	charge transfer coefficient	-
α_{vf}	volume fraction	-
β	thermal expansion coefficient	K^{-1}
β_m	volumetric expansion coefficient	-
δ	thickness	m
ε	porosity	-
η_{act}	activation loss	V
η_{ohmic}	ohmic loss	V
θ	contact angle	°
κ	surface curvature	-
λ	water content	-
μ	viscosity	Pa s
ν	kinematic viscosity	$m^2\ s^{-1}$
ρ	density	$kg\ m^{-3}$
σ	surface tension	$N\ m^{-1}$
σ_{Bolt}	Stephan-Boltzmann constant	$W\ m^{-2}\ K^{-4}$
σ_{mem}	ionic conductivity	$S\ m^{-1}$

Chapter 1: Introduction

Summary

This chapter introduces the current state of energy consumption in the world and the development of fuel cells (FCs). The energy consumption state is shown in Section 1.1. The development of FCs is introduced in Section 1.2, where the classification and application of FCs are discussed separately. Finally, the aims, significance and limitations of this work are summarized in Section 1.3.

1.1 Current state of energy consumption

Energy is closely related to the development of society and people's daily life. In the last few decades, with the rapid increase of population in the world, the consumption of energy has received more and more attention. Especially in the last twenty years, the environmental pollution caused by the use of energy has become a serious problem, since the burning of fossil fuels can produce a large amount of carbon dioxide and some other harmful gases. But, in general, nowadays fossil fuels, e.g. oil, coal and natural gas, still account for the largest proportion of energy consumption in the market. Fig. 1-1 and 1-2 have shown the energy consumption in last few years, from the BP's Statistical Review of World Energy 2018 [1], it can be seen that the total consumption of energy has been evidently increasing in the last years and fossil fuels still account for nearly 85% of the world energy consumption by fuel in 2017. In addition, it is also clear that the percentage of renewables in total energy consumption has shown a great increase in the last ten

years, which indicates the big potential of renewables in the energy market. The use of fossil fuels will cause many environmental issues, such as climate change and environment pollution. In addition, these fuels are unsustainable, and the reserves are limited. Regarding this situation, many renewable and clean energies have received more attention.

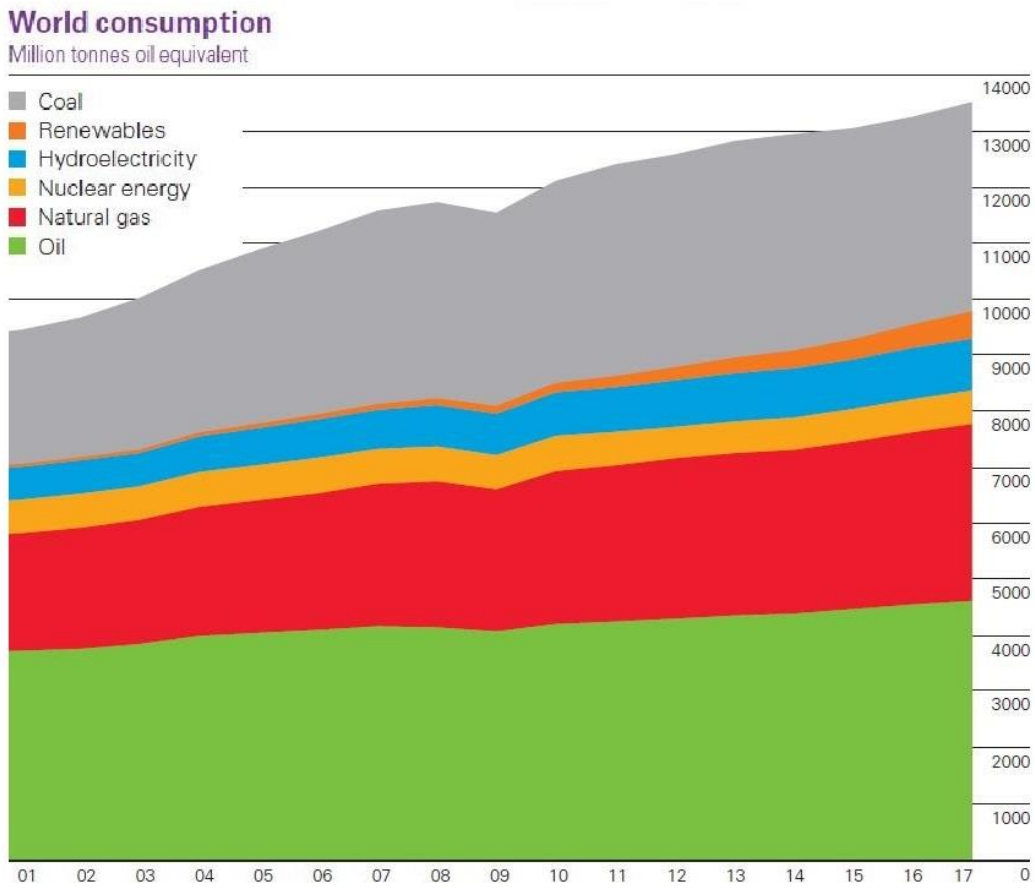

Figure 1-1 The state of energy consumption in recent years (total quantities) [1].

As mentioned, renewables have shown a great potential in the energy market. Fig. 1-3 shows the development and prediction of the total power generation by different

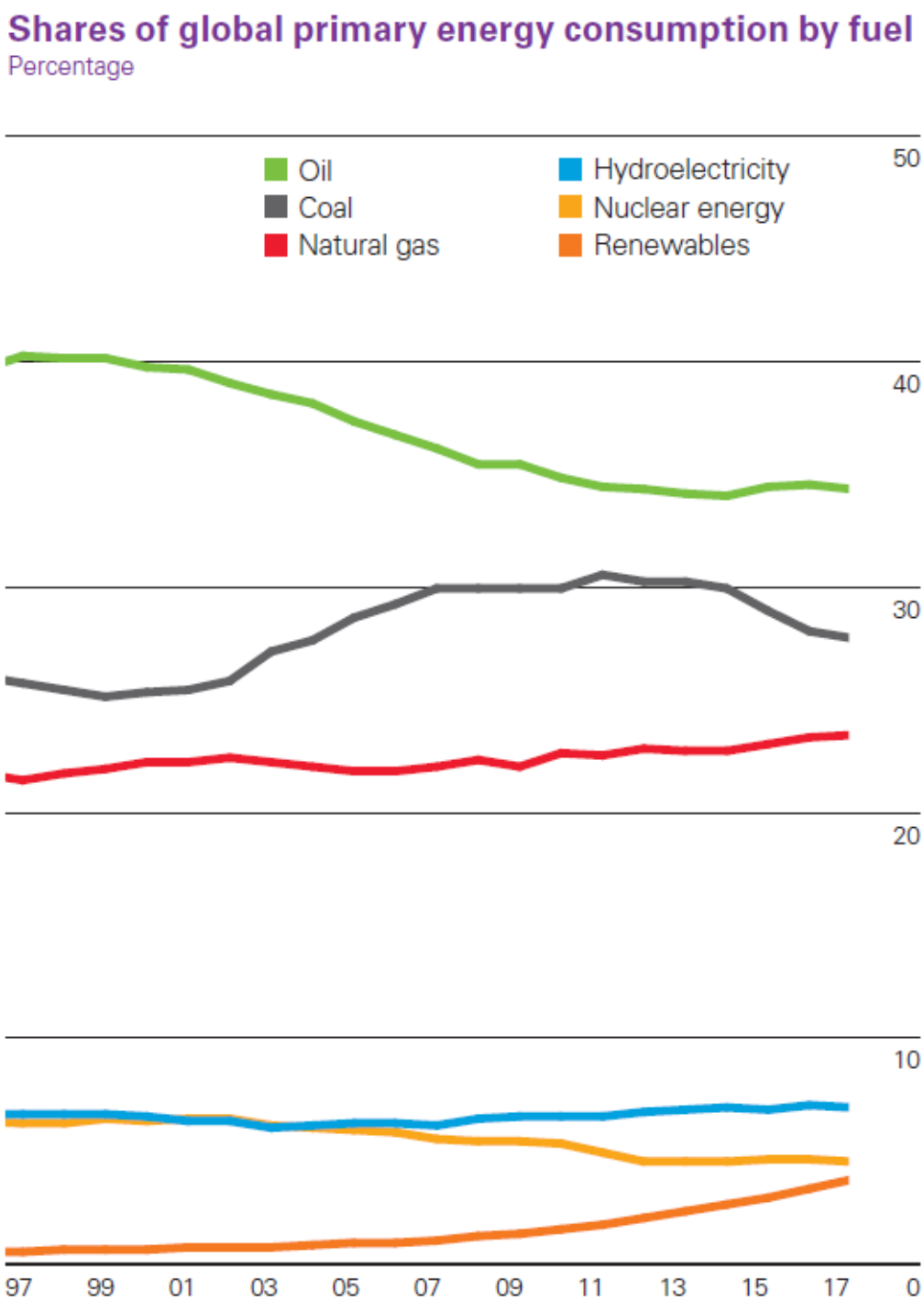

Figure 1-2 The state of energy consumption in recent years (percentage) [1].

energies. The percentage of power generated by renewables accounts for only 7% in 2017 of the total power generation, but it will be almost 25% in 2040. From 2017 to 2040, the percentage of total power generated by fossil fuels will decrease from around 68% to 53%. Based on this situation, in order to reduce the use of fossil fuels and solve the environmental problems, the development of renewable and clean energies is important and urgent.

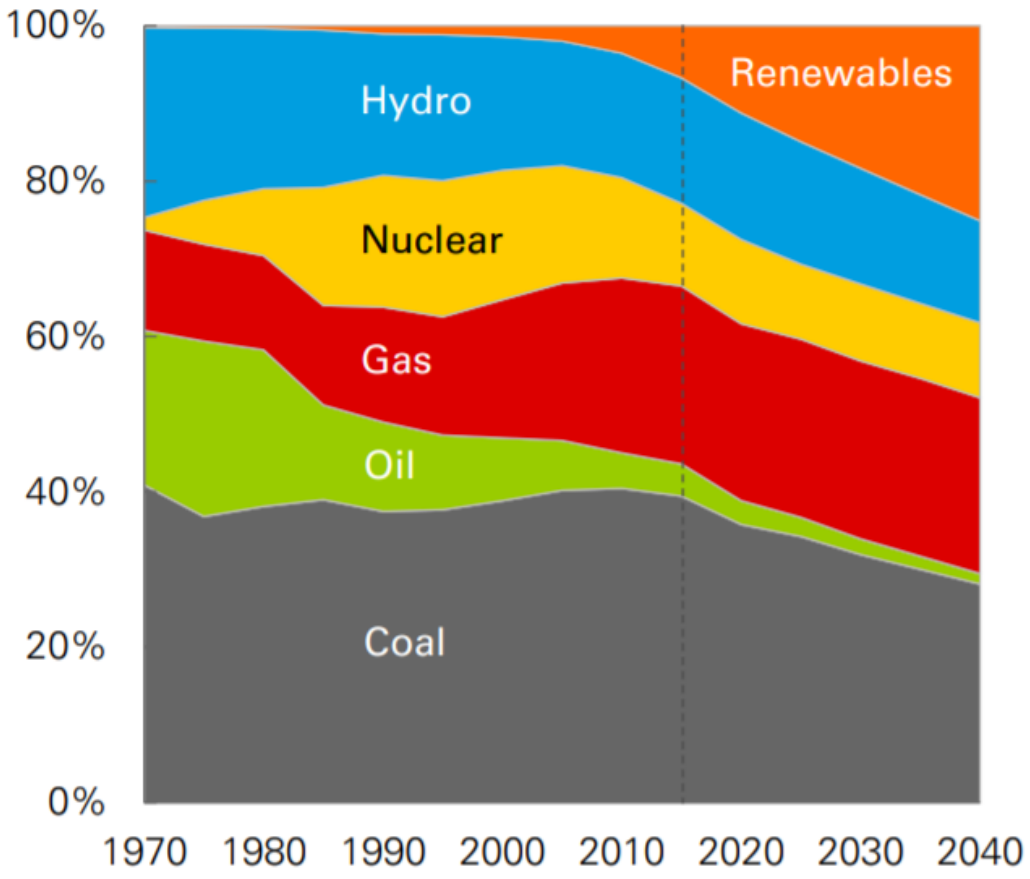

Figure 1-3 The prediction of the total power generation by different energies [2].

1.2 Fuel cell development

Among the different devices for producing power, the FC is one of the most promising devices, where the chemical energy from a fuel is converted to electricity through electrochemical reactions [3]. Compared with other electricity-generating facilities, the FC has many advantages, e.g. high efficiency, fast response and high-power density. In addition, FC systems employ many common and renewable fuels, such as hydrogen, methanol, ethanol and natural gas (NG).

1.2.1 Fuel cell classification

Based on the nature of the electrolytes and the working temperature, FCs can be classified as: low-temperature proton exchange membrane fuel cells (PEMFCs), alkaline fuel cells (AFCs), microbial fuel cells (MFCs) and phosphoric acid fuel cells (PAFCs); high-temperature molten-carbonate fuel cells (MCFCs) and solid-oxide fuel cells (SOFCs). Details of different types of FCs are shown in Fig. 1-4, such as the operating temperatures, general cost, reaction processes and etc. It can be seen that the efficiency increases with increasing the operating temperature, and this is due to the large amount of generated heat which can be used in other combined systems. Among these FCs, SOFCs and PEMFCs are considered to be the most competitive products in future commercial markets because of high durability and mature technologies.

1.2.1.1 Proton exchange membrane fuel cell

PEMFC is the most-widely discussed FC and is already employed in many commercial products. The running mode of PEMFCs is shown in Fig. 1-5(a). The

only final reaction product is water, and this has made PEMFCs become one of the most favourable green power sources. In addition to hydrogen, fuels such as ethanol and methanol can also be used at the anode side. The operating temperature is about 20-100 °C, which enables PEMFCs to start and operate under a normal atmospheric temperature without a preheating process. Due to these characteristics, PEMFCs have shown a great potential to replace conventional batteries in electronic devices in our daily life.

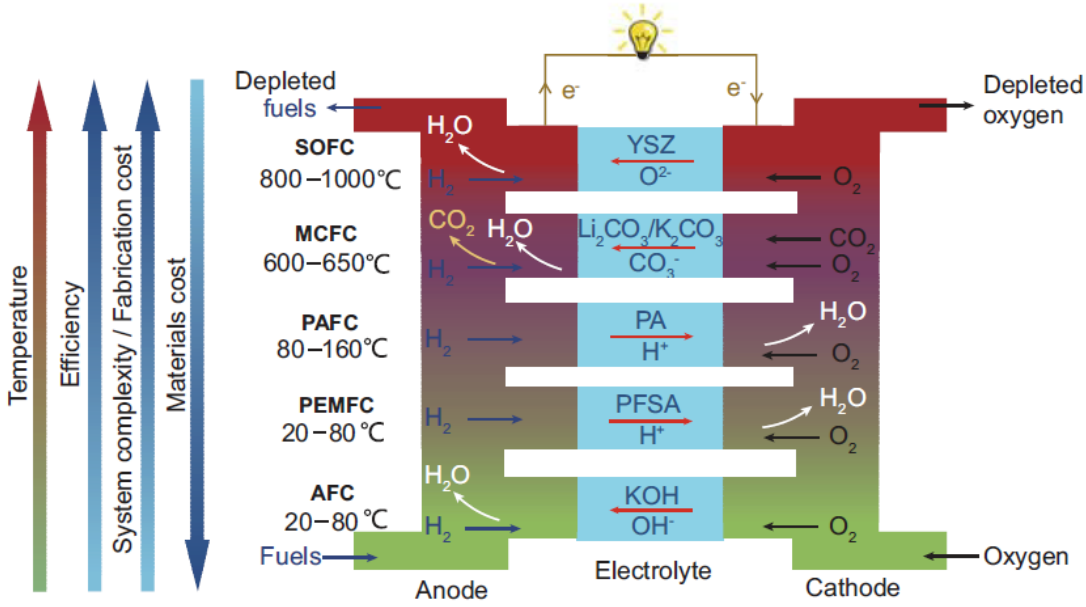

Figure 1-4 Details of various FCs, e.g. temperature, efficiency and material cost [4].

An illustration of the components in FCs is presented in Figure 1-6. A FC normally consists of current collectors (CC), gas diffusion media (GDM), catalyst layers (CLs) and a membrane. CC is linked to external electrical systems and works as pathways for electrons transfer. GDM consists of the GDL and MPL, and plays an

important role in the mass transport and water management. CL is the place where the electrochemical reactions occur, and the properties of the catalysts can

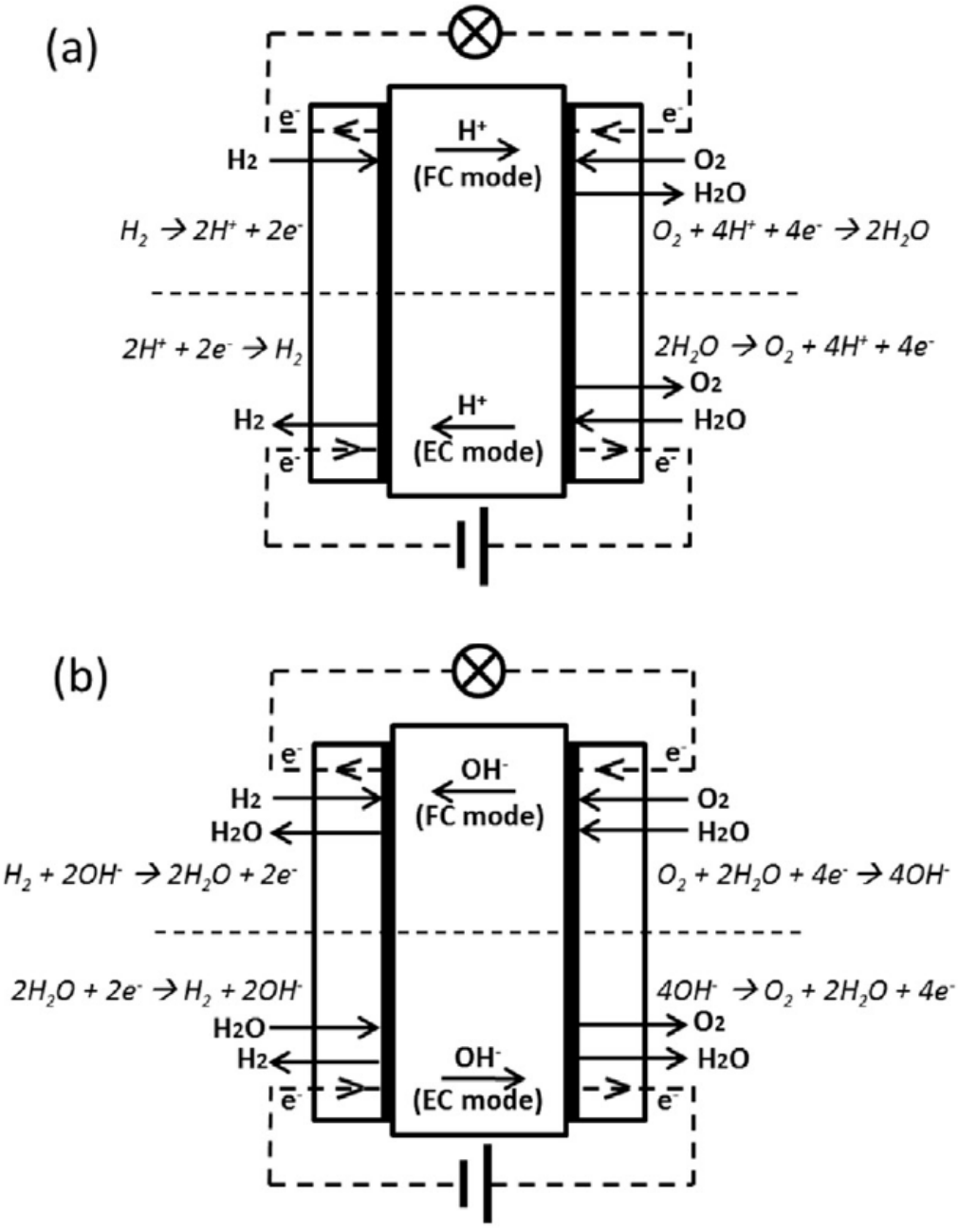

Figure 1-5 A schematic diagram of various FCs: (a) PEMFCs; (b) AFCs [5].

significantly influence the kinetics of the reaction. A selective membrane is normally chosen according to the employed fuels.

Although the development of PEMFCs is already mature, there are still many important problems that need resolving. For example, water management is an important issue in PEMFCs because water is produced at the cathode catalyst layer. This problem is closely related to both the flooding at the cathode and the dry-out of the membrane. Both of these problems reduce the performance of PEMFCs. Another widely-mentioned problem is the high cost of the electrodes and membranes, e.g. noble metal platinum is used as the catalyst in almost all commercial products.

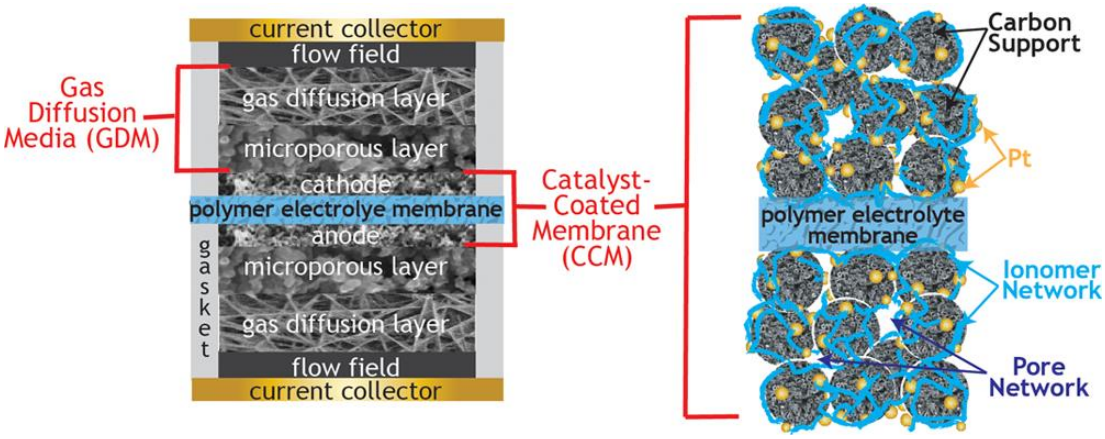

Figure 1-6 Illustration of the components in FCs (left) and the catalyst-coated membrane (CCM) (right) [6].

1.2.1.2 Alkaline fuel cell

The AFC is another kind of the most discussed FCs and has been studied since the early 20th century [7]. As shown in Fig. 1-5(b), hydroxyl (OH^-) is the conducting

ion and this moves from the cathode to the anode, and this is different from PEMFCs, where the protons (H^+) serve as the conducting ion and this moves from the anode to the cathode. Unlike the solid electrolyte use in FCs, the alkaline liquid electrolyte is normally used in AFCs. Since this electrolyte can be made from various inexpensive materials, AFC is almost the cheapest kind of FCs. Another advantage of the AFC is that it can achieve a relative high electricity efficiency, about 65%, without the use of precious metal catalysts. However, the use of an alkaline liquid electrolyte causes some problems. One is the carbonate problem, AFC is very sensitive to CO_2, and a side reaction often occurs. From Eq. (1-1), it is shown that the carbonate is produced by the reaction between OH^- and CO_2, which may reduce the concentration of OH^- and block the pores for transport. Flooding and drying problems also occur in AFCs since the liquid electrolyte is difficult to control [8]. In order to solve these difficulties, the use of a solid electrolyte in the alkaline anion exchange membrane fuel cells (AAEMFCs) have received more attention in recent years, but the technology for this kind of FC is still developing.

$$CO_2 + 2OH^- \rightarrow {CO_3}^{2-} + H_2O \quad (1\text{-}1)$$

1.2.1.3 Phosphoric acid fuel cell

PAFCs are moderately high temperature fuel cells, whose operating temperature is about 200-300 °C. For this reason, although the electricity efficiency for PAFCs is usually 36% to 45%, it can reach 85% if PAFCs are with cogeneration. In PAFCs, liquid phosphoric acid (H_3PO_4) in silicon carbide (SiC) is used as the electrolyte, which is a common and inexpensive fuel. This makes the PAFC a possible choice

for commercialization. However, hydrocarbon fuels that are used in PAFCs may cause greenhouse gas emissions and this may lead to catalyst poisoning. Therefore how to replace hydrocarbon fuels in PAFCs is still a problem before it can achieve a wide utilization.

1.2.1.4 Microbial fuel cell

The MFC is a new type of FCs that has been developed in recent years and it has received more attention and thus becoming a potential alternative energy source in the future. The system of MFCs is similar to that of conventional FCs. However, various microorganisms with possible catalytic capabilities have replaced the widely-used metal catalysts in MFCs. These microorganisms are able to convert the chemical energy from organic fuels to electricity. A schematic of a two-chamber MFC is shown in Figure 1-7. It can be been seen that a proton exchange membrane is employed in MFCs in order to provide a pathway for protons to transfer from the anode chamber to the cathode chamber. It should be noted that, although carbon dioxide is produced as products in MFCs, there is no net carbon emission since the produced CO_2 initially comes from the atmosphere. A significant characteristic of MFCs is that microorganisms can make use of the chemical energy from various organic fuels, such as biomass and even wastewater. This means that MFCs can assist with biodegradation/treatment of biodegradable products as well as produce electricity, which can reduce the waste pollution in our cities [9].

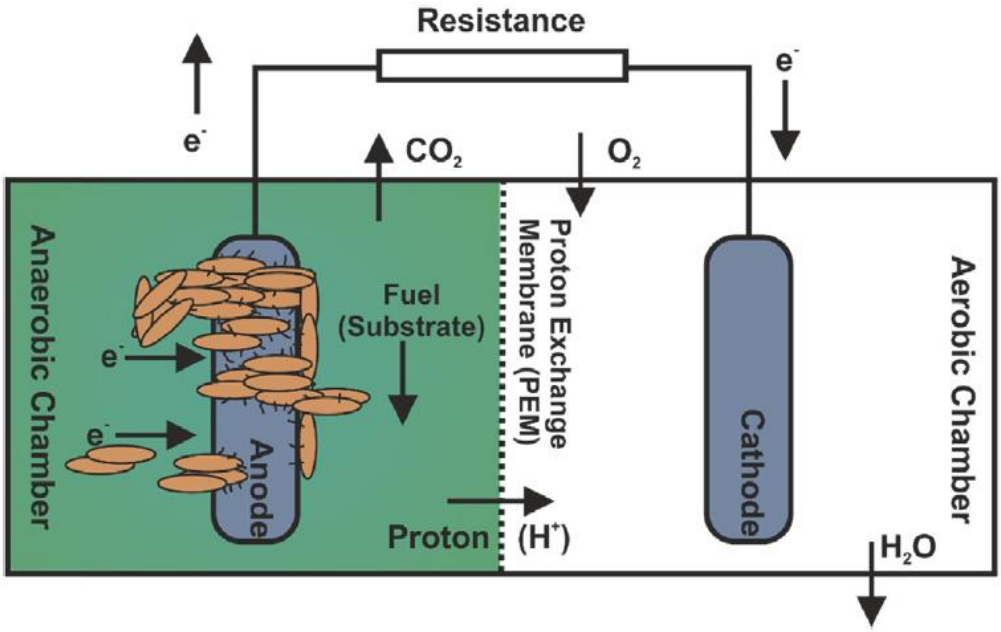

Figure 1-7 A schematic of a typical two-chamber MFC with the illustration of different electro-microbiological and electrochemical processes [10].

However MFCs still face many difficulties before commercialization. One key issue is the low output power and efficiency, the average power output of MFCs is still not comparable to that of PEMFCs. Another problem is the high cost of MFC systems due to the cost of the electrode materials. In addition, microorganisms are usually very sensitive to the operating conditions, e.g. temperature and potential of hydrogen (PH), which leads to a short lifetime of MFCs.

1.2.1.5 Molten carbonate fuel cell

MCFCs are high temperature FCs, whose working temperature is about 600-700 °C. Similar to PAFCs, the electricity efficiency of MCFCs is usually 55%-65%, however this percentage increases to nearly 85% when the waste heat is captured in the MCFC systems. An important characteristic of MCFCs is that the natural gas,

biogas and coals are used as the fuel in this FC, and these reserves are large. For this reason, use of MCFCs to produce electricity has shown a great potential in replacing conventional coal-based power plants. As shown in Fig. 1-4, the carbonate serves as the charge carriers in MCFCs and this diffuses to the anode electrode, and CO_2 reacts with the oxygen (O_2) in the cathode and it returns to the cathode after the anode reaction. As in other high-temperature FCs, MCFCs do not require precious metals to be used as catalysts and the fuels employed in MCFC systems can be reformed within the system, thus eliminating the need for an expensive, external reformer system. Both of these reduce the cost of MCFCs. Another benefit is that MCFCs are not likely to be affected by CO or CO_2 poisoning since platinum is not used in these systems. However, the use of coals may lead to sulphur poisoning since some types of coals contain a large amount of sulphur. In addition to this disadvantage, high temperatures can influence the durability and reduce the life of MCFCs.

1.2.1.6 Solid-oxide fuel cell

SOFC is a widely-discussed high temperature FC. As shown in Fig. 1-8(a, b), oxygen ions or protons work as the charge carriers in SOFCs and water is the only product. Since SOFCs work at high temperatures, i.e. 800-1000 °C, the catalysts are not essential to accelerate the reaction in SOFCs, and the lack of catalysts also avoids various poisoning problems. In addition, the fuels used in SOFCs also do not need the reform process before entering SOFC systems [11]. However, the high operating temperature introduces some issues when applying SOFCs. The most

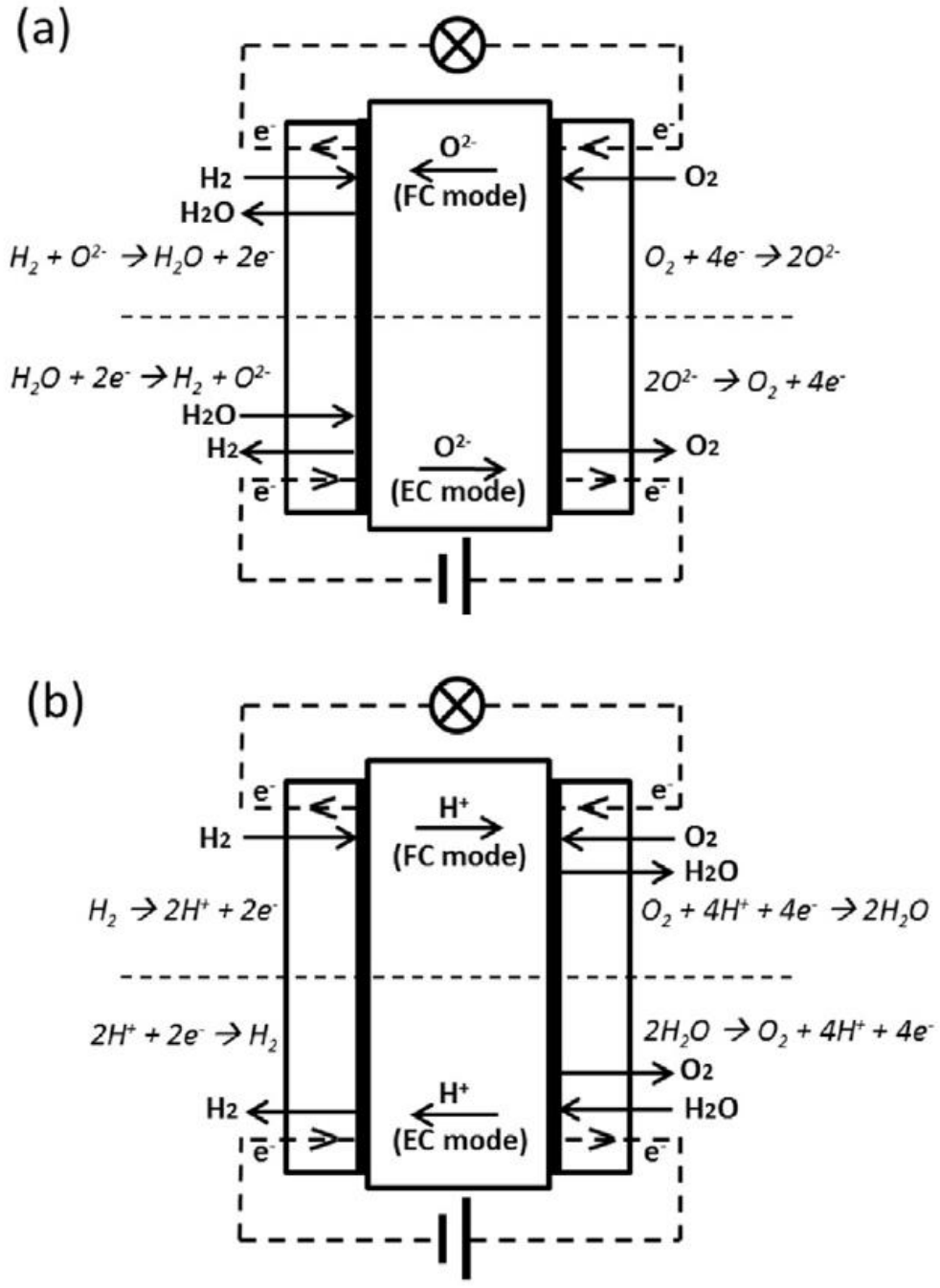

Figure 1-8 A schematic diagram of SOFCs: (a) SOFCs with oxygen ion conducting electrolyte; (b) SOFCs with proton conducting electrolyte [5].

important issue is that the SOFC requires a very long preheat process after the startup and this largely limits the application in transportation. Another problem associated with the working temperature is that the preheat process is often achieved by high-temperature steams. In order to reach the operating temperature, the heat generation equipment is necessary, and this increases the complexity and reduces the efficiency of the SOFC system. At present, a large number of studies focus on decreasing the working temperature of SOFCs, and the lower temperatures also enable the use of various inexpensive materials [12,13].

1.2.2 Fuel cell applications

The history of FCs dates back to 1838 when the principle of FCs was first published in the "Philosophical Magazine." This led to studies on different kinds of FCs and there are, in general, four main applications of FCs, i.e. stationary, transportation, portable and micro power.

1.2.2.1 Stationary

Stationary power systems are the most common application of FCs, in which the PEMFC is the most popular. However AFCs, PAFCs and even high-temperature SOFCs have also been employed in building stationary power systems. The output power for stationary systems can range from a few Watts up to 20 MW [14], and this is decided by the scale of the stationary systems. Large stationary systems (output power from 300 kW to 20 MW) are normally employed in building power systems for a large residential region. In order to improve the energy efficiency, these are usually used for combined heat and power (CHP) generation [15]. For this

reason, high-temperature SOFCs are more competitive than PEMFCs and PAFCs. Also the fuels used in SOFC do not require a reform process, and this simplifies the system. For medium (output power from 10 kW to 30 kW) and small (output power from a few Watts to 10 kW) stationary systems, these are served as power sources for individual buildings, such as hospitals, schools and etc. Remote-region power supply (RRPS) is another important application for those relative small stationary systems. In some remote regions, e.g. deserts and islands, small stationary FCs can generate electricity for running facilities in these regions. Among all small FCs stationary systems, the PEMFC is the most popular.

1.2.2.2 Transportation

The application of FCs in transportation has received more attention in recent years, and this is because of the low-emission character of FCs can solve air pollution problems in cities. So far, mass-produced fuel cell electric vehicles (FCEVs) are designed based on PEMFCs. Compared with battery electric vehicles (BEVs), FCEVs have advantages of longer driving distances (over 500 km) and these have a quicker refuelling process (3-5 minutes for the hydrogen refuelling process). However FCEVs account for a very small proportion in total of the electric vehicle (EV) sales, for example FCEVs only occupy 0.5% of the total EV sales in 2016 [16]. The high cost of FCEVs is the main limitation for its commercialization, and this is attributed to expensive materials, e.g. platinum and carbon fibre. Fig. 1-9 illustrates the vehicle cost as a function of driving distance for two typical vehicles using BEVs and FCEVs. It can be seen that BEVs are more attractive in the

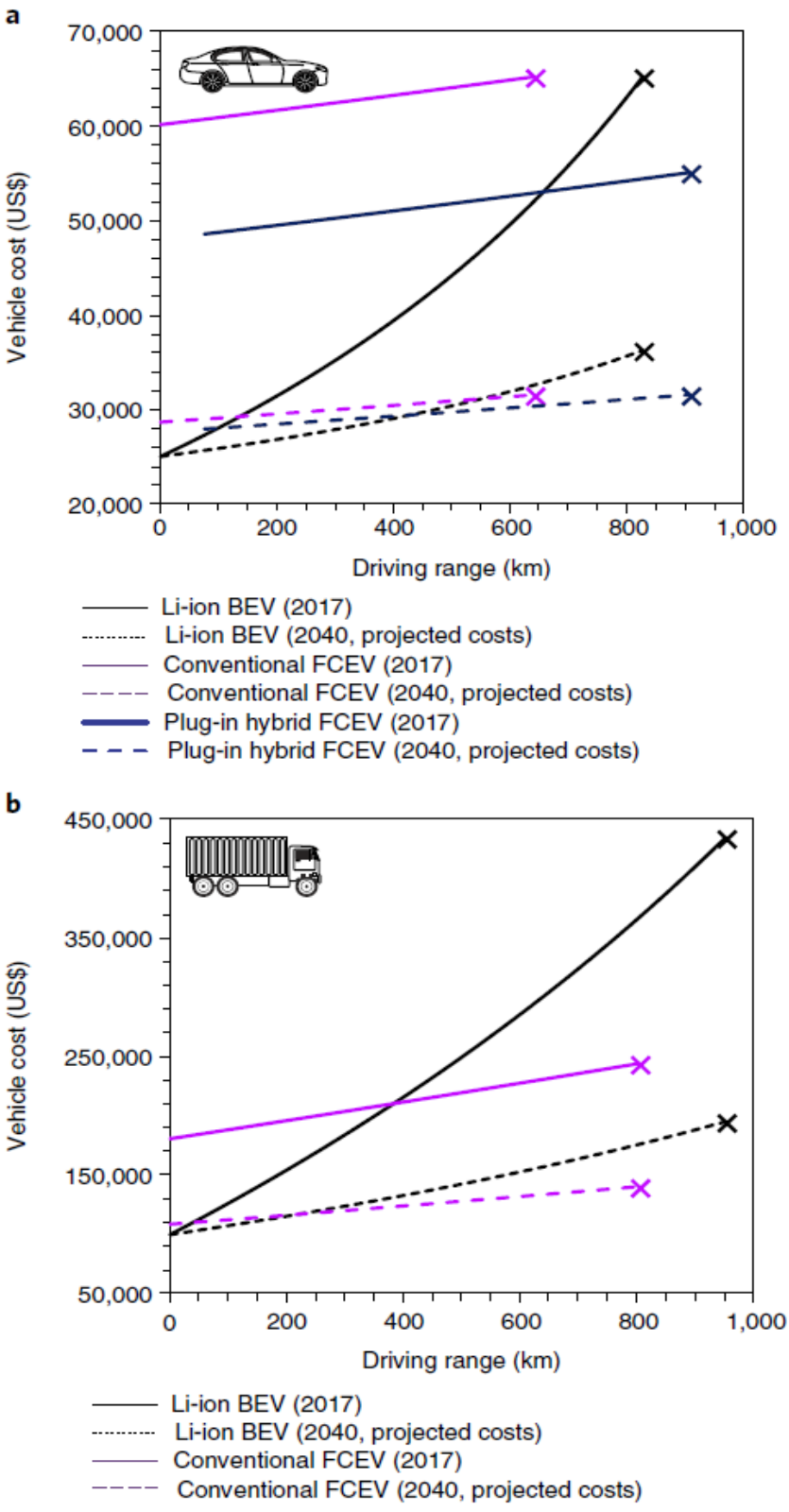

Figure 1-9 Cost as a function of driving distance for two typical vehicles: (a) mid-size vehicle and (b) semi-trailer truck [16].

mid-size vehicles with a long driving range. However, FCEVs are competitive in the high-utilization transportation with a long driving range, such as trucks. Unlike BEVs, energy and power are decoupled in FCEVs and this makes FCEVs more cost-effective than BEVs in long-range driving transportation. Another advantage of FCEVs is that, they have a quicker refuelling process and this makes FCEVs a competitive choice for high-utilization transportation. In addition, the rapid development of hydrogen production and storage technologies makes FCEVs more attractive in high-utilization transportation.

1.2.2.3 Portable

Use in portable devices is another application of FCs. With the development of portable electronic devices, the requirement for batteries has become ever increasingly more strict. Regarding this situation, some kinds of FCs have been shown to have a great potential in replacing conventional batteries, e.g. PEMFC, air-breathing proton exchange membrane fuel cell (AB-PEMFC) and direct-methanol/ethanol fuel cell (DMFC/DEFC) [17,18]. The main advantages of these FCs are the relative high power density, simple refuelling process, silent operation and low weight. However, the generation and storage of hydrogen and the potential leak of liquid fuels are still big problems before the wide use of these FCs in portable devices. Typically, FCs can generate electricity in consumer electronics (e.g. laptops and cell phones), some portable power generators and military applications. In order to simplify the FC system in portable devices, the cathode side of the FC is often designed to be air-breathing, which means that the cathode

is open to the ambient, and air can flow into the FC and be used as the fuel. This design largely facilitates the production of the FC and reduces the cost of it.

1.2.2.4 Micro

The main barrier for the development of microelectronic devices is the micro power source and thus it is important to produce micro power sources with a small volume, long life and acceptable power density. The FC is a possible choice for a micro power source, e.g. micro direct methanol fuel cells (μDMFCs). Fig. 1-10 presents a fabricated μDMFC, which is used as the power source for microelectronic devices. The total size of this μDMFC is 25.4 mm × 17 mm × 6.2 mm, and the maximum power density and open circuit voltage (OCV) can reach 3.86 mW/cm^2 and 0.47 V, respectively [19]. In addition to the μDMFC, hydrogen PEMFC is also employed in producing micro power sources.

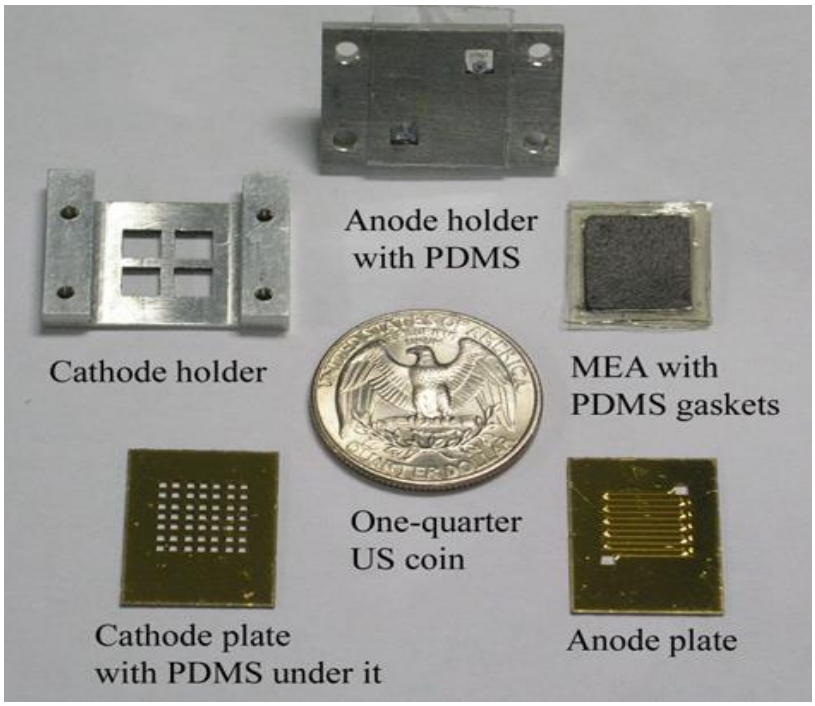

Figure 1-10 A fabricated μDMFC [19].

1.3 Thesis structure

1.3.1 Research aims and objectives

The research aims and objectives of this research are as follows:

- To investigate the effects of different component properties and operating conditions on the AB-PEMFC performance. In order to investigate the relative humidities of both oxygen in the ambient and hydrogen in the anode, revised water transportation relations are applied in the presented model. In addition, the sensitivity of the fuel cell performance to the heat transfer coefficient is investigated, the limiting reason for AB-PEMFCs at high current densities is investigated under different heat dissipation situations.
- To study the local performance of anode channels in AB-PEMFCs in order to provide information on water removal in real designs of the channels. The CFD model is based on a 3-D VOF method, and the operating conditions and the water properties are changed in order to represent different flooding conditions.
- To investigate the effect of stacking on the GDL permeability, experiments are conducted to prepare GDL stacks with different amounts of GDL samples. The gas permeabilities for different GDL stacks are calculated and then compared.

The research highlights of this research are as follows:

- An efficient mathematical model for AB-PEMFCs has been developed and new revised water transportation equations are employed in this present model. The limiting reason for AB-PEMFCs at high current densities is investigated under different heat dissipation situations, which is found to be different from the situations in conventional PEMFCs. Further, the commonly-neglected hydrogen humidity is investigated in detail and it is found to be important in determining the performance of the AB-PEMFC.
- A 3D volume of fluid model for PEM fuel cell anode channels has been built. The sensitivity of the dynamics of the liquid water droplets to their position in the channel is studied for the first time. In addition, the effects of the hydrogen velocity, droplet size and channel wettability are studied in order to provide information on the water removal in the anode channels in AB-PEMFCs.
- The effect of stacking on the GDL permeability is investigated. In previous studies, only the effects on single GDL layer have been studied in detail. However, the GDL stack is different from the single GDL, the stacking of GDLs may cause gaps between each layer in the stacks and thus influence the gas permeability of the GDL stacks. During the experiment, the gas permeabilities of different GDL stacks are calculated and then compared.

1.3.2 Significance and limitation of the work

The first part of this research mainly studies the overall performance of AB-PEMFCs. The limiting mode is investigated in AB-PEMFCs under various heat dissipation situations. Further, in order to study the effects of the components properties and operating conditions on the AB-PEMFC performance, an efficient

mathematical model is built based on the heat and mass transfer. The main improvement in this model is that the water transportation is revised and the mass transfer in the anode and cathode are combined, and this is usually simplified in the AB-PEMFC models. However, a significant limitation is that the liquid phase is not considered in the present model, although the effects of these liquid phase is discussed. The inclusion of liquid phase and relevant corrections can help the present model generate more accurate polarisation curves for the AB-PEMFC, especially at moderate current densities.

The second part of the research is focused on the anode channels in AB-PEMFCs, which is not included in the first model. Although flooding is not common at the anode side in PEMFCs, the anode channels can suffer heavy flooding if the relative humidity of the hydrogen is too high. In order to investigate the effects of the initial position of the water droplet, its size as well as the wettability of the GDL under different operating conditions, the 3D VOF model is built. The findings of the study provide important and insightful information when designing AB-PEMFCs which are vulnerable to water flooding at their anode. In order to further study the effects of water in the anode channels, it will be of interest to correlate the VOF model with the electrochemical reaction of the fuel cell, thus enabling the evaluation of the effects of all the parameters investigated in this study on the overall performance of the AB-PEMFCs.

The third part of the research is about GDL experiments and the stacking of GDLs is studied in this research. Unlike previous studies, the through-plane gas permeability of the GDL stacks, instead of single GDL layer, is investigated.

However, other properties of the GDL stacks, such as the in-plane gas permeability, electrical resistance and thermal conductivity, have not been studied.

Chapter 2: Literature review

Summary

This chapter reviews the main problems of limiting the performance of AB-PEMFCs and relevant improvement methods. The investigations on the overall performance of AB-PEMFCs are presented in Section 2.2. In addition, investigations on the performance of the components employed in AB-PEMFCs is reviewed in Section 2.3.

2.1 Main problems in AB-PEMFCs

AB-PEMFCs have attracted considerable attention for replacing batteries in some portable devices, such as laptops and smartphones [20]. Unlike conventional PEMFCs, the mass and heat transfer at the cathode side is governed by natural convection in the AB-PEMFCs, thus simplifying the fuel cell system. Namely, the AB-PEMFC system normally consists of only the fuel cell (or the fuel cell stack) and a storage device for hydrogen. However, this simplification produces a rather low performance when compared with that of the conventional PEMFCs and this is due to the low mass and heat transfer coefficients at the open cathode of the AB-PEMFC [21,22].

In addition to the low performance, water management is another important issue in AB-PEMFCs and this is closely related to both flooding at the cathode and dry-out of the membrane. The flooding at the cathode significantly increases the concentration losses because it hinders the transport of oxygen from the ambient

(in the case of the air-breathing mode of operation) or the flow channel to the catalyst layer, while the dry-out of the membrane causes large ionic resistance in the fuel cell [23,24]. The flooding situation is sometimes more severe in AB-PEMFCs when compared with PEMFCs, since the mass transfer coefficients are relatively low and thus water is more difficult to be removed.

2.2 Investigations on the overall performance of the AB-PEMFCs

In order to improve the performance of AB-PEMFCs, there have been a number of both modelling and experimental investigations to examine the effects of structure designs and operational parameters on the performance of AB-PEMFCs.

2.2.1 Component designs

Fig. 2-1 shows a schematic of an AB-PEMFC. It can been seen that there is no flow channel in the cathode side and the cathode GDL is exposed to the ambient air, while hydrogen flows through the channels and then enters the anode side. Since water is produce at the cathode side of the membrane electrode assembly (MEA), more investigations have focused on improving the water management at the cathode components. In order to improve the performance of AB-PEMFCs, the properties of the components in AB-PEMFCs have been investigated in detail. For example, the thermal conductivity of the GDLs was investigated in [25], and these results showed that a lower thermal conductivity can lead to a higher cell temperature and thus the produced water is more easy to be removed. Schmitz et al. [26] have discussed the effects of the GDL thicknesses and opening ratios. It

was found that the use of thicker GDLs can decrease the contact resistances and an optimal opening ratio is favoured for the GDL; similar findings can be found in [27–29]. In addition to the properties, use of different materials for these components in AB-PEMFCs were also discussed by many research groups; see for example [30–32]. Further, some new designs for AB-PEMFCs have been widely studied. Fabian et al. [33,34] reported new AB-PEMFCs systems with both active and passive water management devices, and the results showed that the efficiency

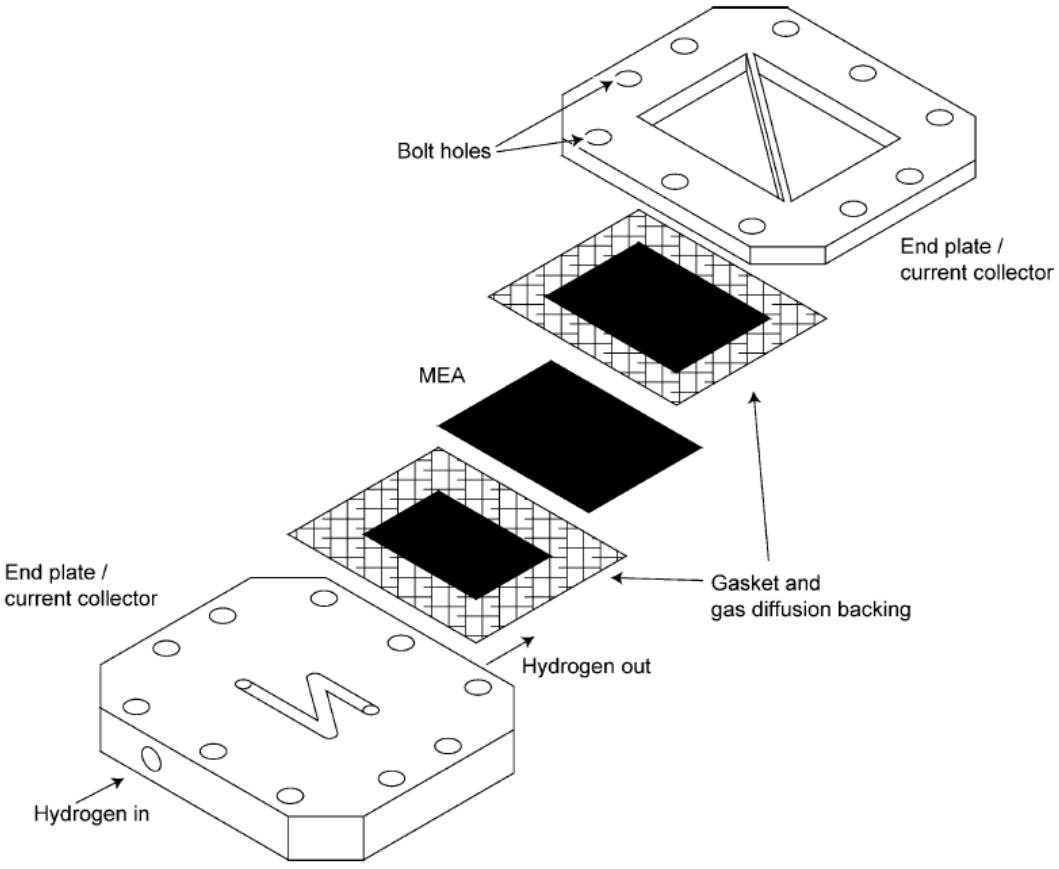

Figure 2-1 A schematic of an AB-PEMFC.

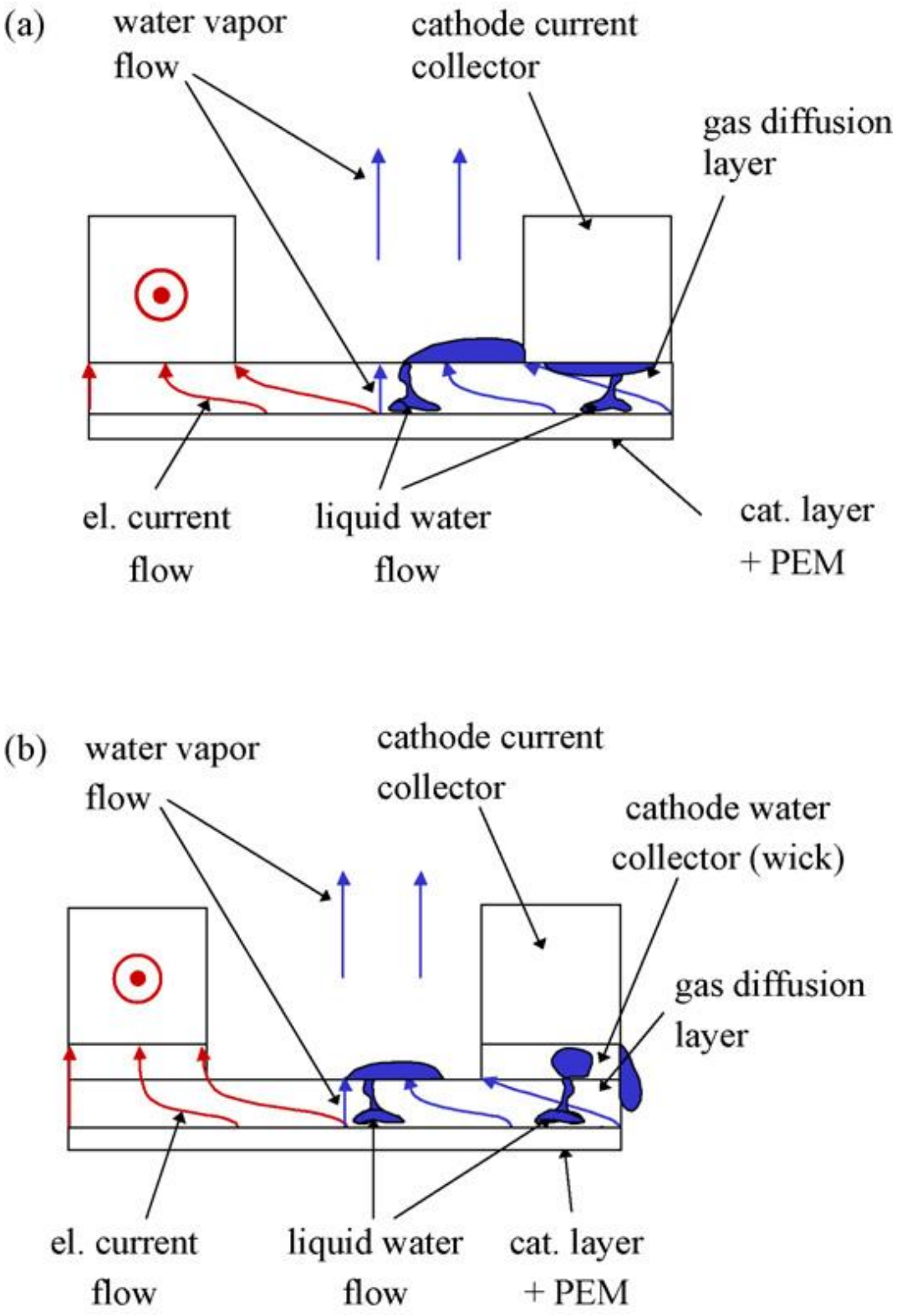

Figure 2-2 A schematic of passive water management design shown in [34]. An AB-PEMFC cathode (a) without and (b) with a porous and hydrophilic wick serving as a water collector.

of the AB-PEMFC can be substantially improved. The passive water management design is shown in Fig. 2-2, where a hydrophilic wick works as a water collector. Jung et al. [35] and Dean et al. [36] have employed silicon structures in AB-PEMFCs, and they found that these structures can prevent liquid water accumulation in the GDLs and thus the performance of the AB-PEMFC can be improved.

2.2.2 Operating conditions

The change in the operating conditions, e.g. RH and temperature, has a significant influence on the water content of the membrane and the condensation of water. Therefore, many studies have investigated the effects of the operating conditions. Some experimental results have showed that the cell performance increases as the RH increases at relatively low humidity conditions. However, for high humidity conditions, an increase in the RH reduces the performance of the fuel cell as it usually leads to water flooding; see for example [37–39]. Also many modelling studies have investigated the effect of the RH and have obtained similar findings; see for example [40,41]. While for the temperatures, an optimal temperature is favoured in order to maintain high-hydration of the membrane and prevent liquid water generation at the same time; see for example [42,43].

2.3 Investigations on the local performance of the components in the AB-PEMFCs

2.3.1 Flow channels

Over the past decade, water flooding in the gas channels has attracted much attention and this is due to the influential role of the flow channels in transporting the reactants to the reactive sites in the catalyst layers through the GDLs. Liquid water accumulation in the channels may increase the pressure drop along the channel and, if severe, may cause blockage to the flow of the reacting gases, thus decreasing the efficiency of the fuel cell system.

2.3.1.1 Visualization experiment

Many experimental studies have employed different visualization methods to investigate the two-phase flows [44], e.g. direct visualization [45–47], X-ray [48–50], Magnetic Resonance Imaging (MRI) [51] and neutron imaging [52–54]. In addition to the channels, visualization methods are also employed in studying the water behaviour in GDLs and MEAs. The results from the visualization methods can provide useful information about the water behaviour in PEMFCs and assist in the design of the commercial products. A main limitation associated with these methods is that transparent materials are often used in these experiments, and this may cause different heat transfer and water behaviour when compared with conventional materials. Although this problem has been overcame by using some leading-edge equipment, the cost caused by using the equipment is still a big problem when performing visualization experiments in PEMFCs.

2.3.1.2 Numerical methods

Compared with visualization experiments, modelling investigations of the water behaviour are sometimes more time-saving and cost-effective. In the early studies, the multi-phase mixture (M^2) model and the multi-fluid model have been employed to investigate the two-phase flows [55–58]. However these two methods cannot describe the form and the motion of the liquid water. In order to track the dynamics of the liquid water, the two-phase flow is investigated by other methods, e.g. the pore-network (PN), Lattice Boltzmann (LB), and the volume of fluid (VOF) methods. More details about these methods can be found in the review paper [59]. The VOF method is chosen in this study because it is better at considering the surface tension and wall adhesion effects when compared with the above-mentioned methods.

The VOF method models two or more immiscible fluids by solving a set of momentum equations and tracking the volume fraction of each phase throughout the domain. There are two phases in the computational domain of PEMFCs, and subscripts 1 and 2 are used to represent phase 1 and phase 2, respectively. The sum of the volume fractions is equal to one in each computational cell; therefore, the volume fractions of phase 1 and phase 2 can be obtained by:

$$\alpha_{\mathrm{vf}1} + \alpha_{\mathrm{vf}2} = 1 \tag{2-1}$$

The continuity and momentum equations are as follows:

$$\frac{\partial \rho}{\partial t} + \nabla \cdot \left(\rho \vec{u} \right) = 0 \tag{2-2}$$

$$\frac{\partial(\rho\vec{u})}{\partial t}+\nabla\cdot(\rho\vec{u}\vec{u})=-\nabla p+\nabla\cdot\left[\mu\left(\nabla\vec{u}+\nabla\vec{u}^{T}\right)\right]+\vec{F} \tag{2-3}$$

where $\vec{u}$ is the velocity, p is the pressure, ρ and μ are the volume averaged density and dynamic viscosity, respectively, and are given by:

$$\rho=\alpha_{\mathrm{vf1}}\rho_1+\alpha_{\mathrm{vf2}}\rho_2 \tag{2-4}$$

$$\mu=\alpha_{\mathrm{vf1}}\mu_1+\alpha_{\mathrm{vf2}}\mu_2 \tag{2-5}$$

and $\vec{F}$ is the momentum source term. In order to capture the effects of the surface tension, the continuum surface force (CSF) is employed to calculate $\vec{F}$ [60]:

$$\vec{F}=\sigma\frac{\rho\kappa_1\nabla\alpha_{\mathrm{vf1}}}{0.5(\rho_1+\rho_2)} \tag{2-6}$$

where σ is the surface tension coefficient, and κ_1 is the surface curvature defined in terms of the divergence of the unit normal $\vec{n}_1$:

$$\kappa_1=\nabla\cdot\vec{n}_1 \tag{2-7}$$

$$\vec{n}_1=\frac{\nabla\alpha_{\mathrm{vf1}}}{|\alpha_{\mathrm{vf1}}|} \tag{2-8}$$

The curvature of the surface near the wall are adjusted in order to reflect the effects of the wall adhesion force. In the cells near the wall, the modified surface normal $\vec{n}$ is given by:

$$\vec{n}=\vec{n}_{wall}\cos\theta_{wall}+\vec{t}_{wall}\sin\theta_{wall} \tag{2-9}$$

where θ_{wall} is the contact angle of the wall, and $\vec{n}_{wall}$ and $\vec{t}_{wall}$ are the unit vectors normal and tangential to the wall, respectively.

Based on VOF method, the channel geometry and property have been widely studied since they can influence the dynamics of the water in the channels. In commercial flow channels, straight, U-shape and serpentine designs are often used,

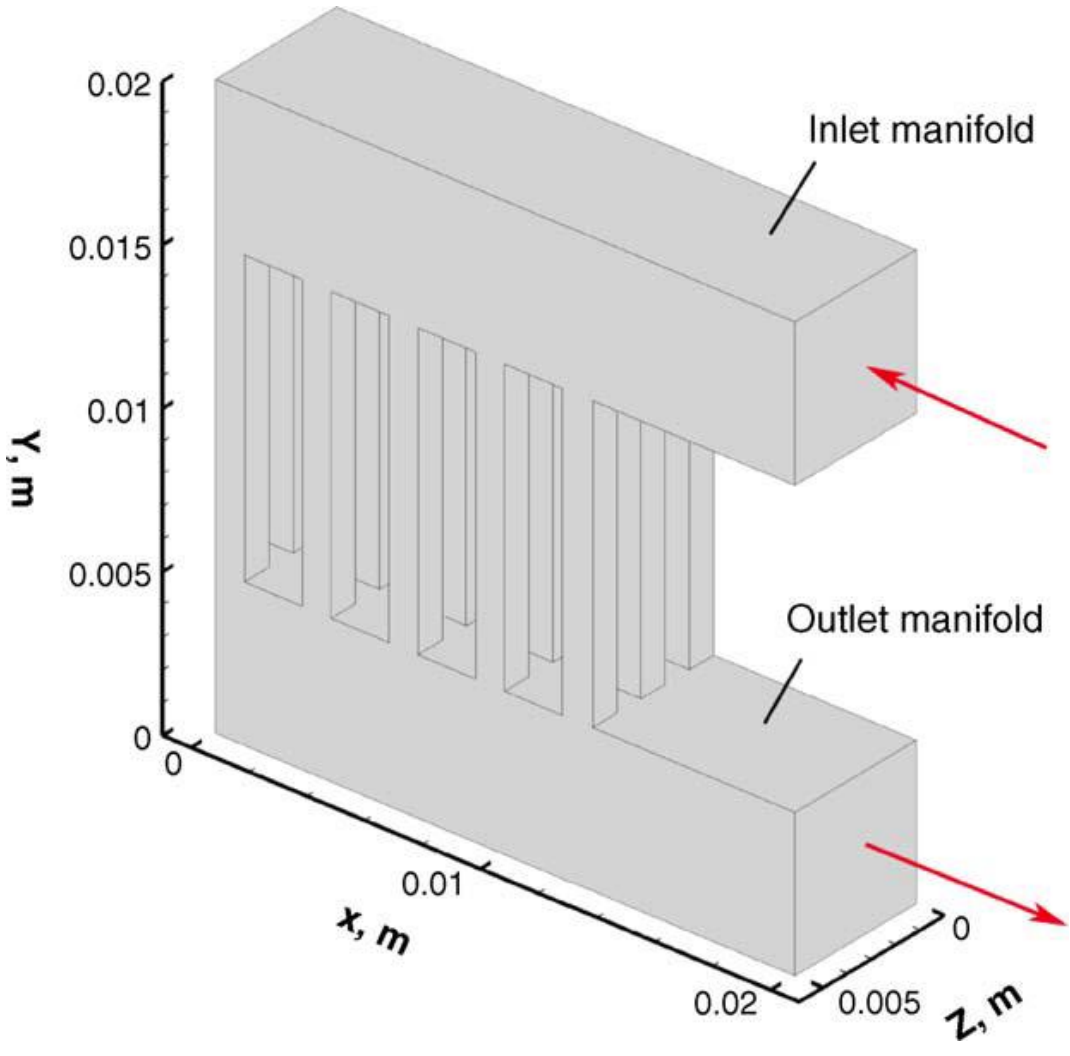

Figure 2-3 A schematic design of serpentine channels with the manifolds as proposed in [61].

while other new shapes of channels are also investigated. For example, Kui et al. [61,62] have proposed a design of serpentine channels with manifolds, which is shown in Fig. 2-3. It was found that the water blockage is improved in this channel when compared with above-mentioned traditional channels. In addition to shape, the effects of the properties of the channels, e.g. wettability and length, have been also investigated by many groups; see for example [63–65]. Further, some studies have focused on the behaviour of the water droplets in the channels. Processes, such as emergence, detachment and merging of the water droplets, can be tracked through modelling [66–68] and some useful information, e.g. pressure drop in the channel, can be recorded at any time [69,70].

The above-mentioned investigations of the channels only focus on the channels. In order to determine the effect of different water dynamics on the cell performance, electrochemical reactions are coupled with the present VOF models [71]. Le and Zhou [72,73] proposed a three-dimensional and unsteady model with the VOF interface tracking method. The effects of the liquid phase on reactant concentration and current density distribution were investigated. Chen et al. [74] built a three-dimensional VOF model with an extra surface to represent the CL. The current density and oxygen concentration distributions were investigated under various operating conditions. Ferreira et al. [75] proposed a 1D + 3D model, where the VOF method in the gas channel (GC) is coupled with the electrochemical reactions and the water balance in the membrane. In addition to the current density, the water distribution within the GDL was described. The model proposed in this research is shown in Fig. 2-4.

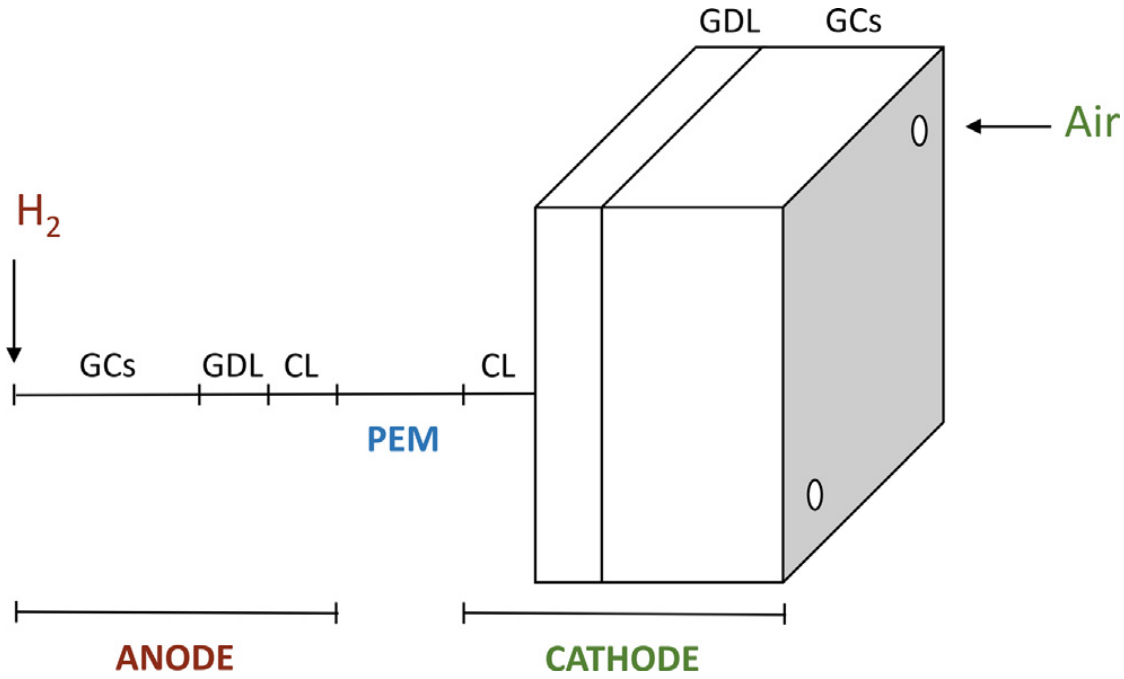

Figure 2-4 A schematic of a 1D + 3D model proposed in [75].

2.3.2 Gas diffusion layers

The GDL is a key component in PEMFCs. The main roles of GDLs are improving the transport and facilitating a uniform distribution of both reactants, i.e. hydrogen and oxygen, and the product, i.e. water, between the active area and the flow field [76], and its electrical and thermal conductivity also influence the performance of the PEMFC. Therefore GDLs with high gas permeability and low electricity resistance are usually recommended in PEMFCs. A commercial GDL is usually composed of a macroporous substrate with or without a MPL. The macroporous substrate plays an important role in transporting the reactants and providing sufficient mechanical support for the MEA. While the MPL, which comprises carbon black powder and hydrophilic/hydrophobic agent, can reduce the contact resistance between the substrate and the CL and this enhances the water

management under different operating conditions. A SEM cross-section image of a GDL is shown in Fig. 2-5.

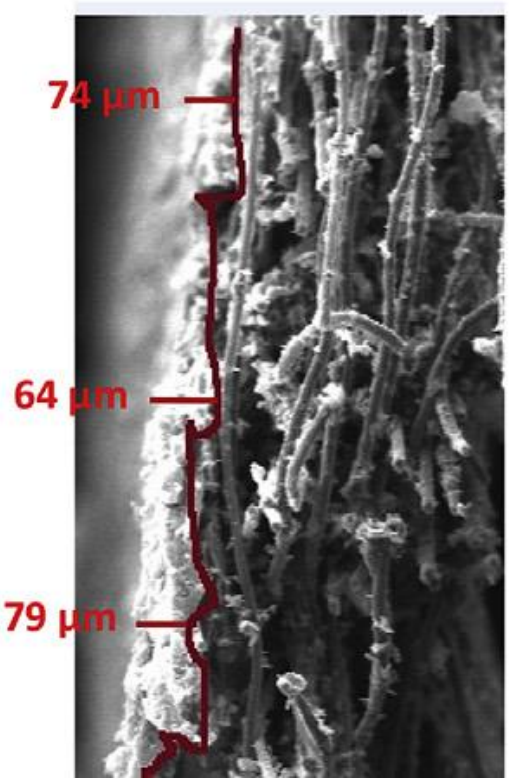

Figure 2-5 A SEM cross-section image of a GDL. Note that the values are the thicknesses of the MPL layer [77].

2.3.2.1 Materials and properties

Carbon-based GDLs have been widely used in PEMFCs because of their relative high permeability and low electrical resistance [78,79]. However other materials have also been employed to produce GDLs, e.g. thin metal sheets [80,81]. Compared with carbon materials, use of metal sheets can better control the porosity and pore size distribution in the produced GDLs, and also the thickness of the GDLs can be controlled. A produced metal sheet GDL is shown in Fig. 2-6. In addition to

the use of new materials, properties such as porosity, pore size and wettability are important in determining the water management ability of the GDLs. Instead of changing the overall porosity of the GDL, Jeong et al. [82] produced a porosity-graded MPL by using thermal expandable graphite (TEG) and they tested it in a fuel cell system. They found that the MPL increases the performance of a single cell, especially at high current densities. A hydrophilic MPL (made of VGCF-H and ionomer) was investigated by Tanuma et al. [83], and it was found that the MEA with the hydrophilic MPL showed the highest cell voltage under both dry and wet operating conditions when compared with various conventional GDLs.

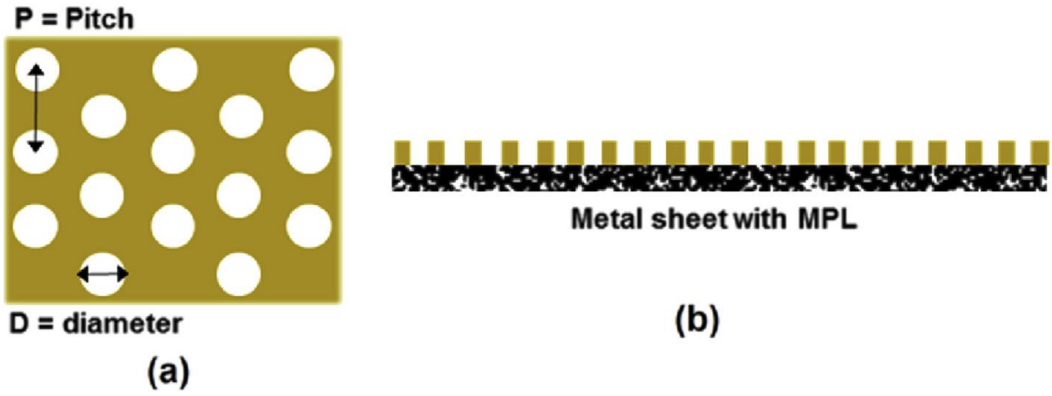

Figure 2-6 A schematic of the metal sheet GDL in [80]: (a) top view; (b) side view.

2.3.2.2 Structure designs

Structure design of GDLS is another method in order to improve the water management in GDLs. Nishida et al. [84] fabricated a GDL with grooves (shown in Fig. 2-7). The grooves work as pathways for the liquid water and thus the water could be more easily removed. It can be seen in Fig. 2-7 that the liquid water

accumulates in the grooves in the grooved GDL, while the distribution of the water is less uniform in the untreated GDL. Nishida found that the voltage can remain almost constant after a relative long operating time, i.e. 2000s, under different

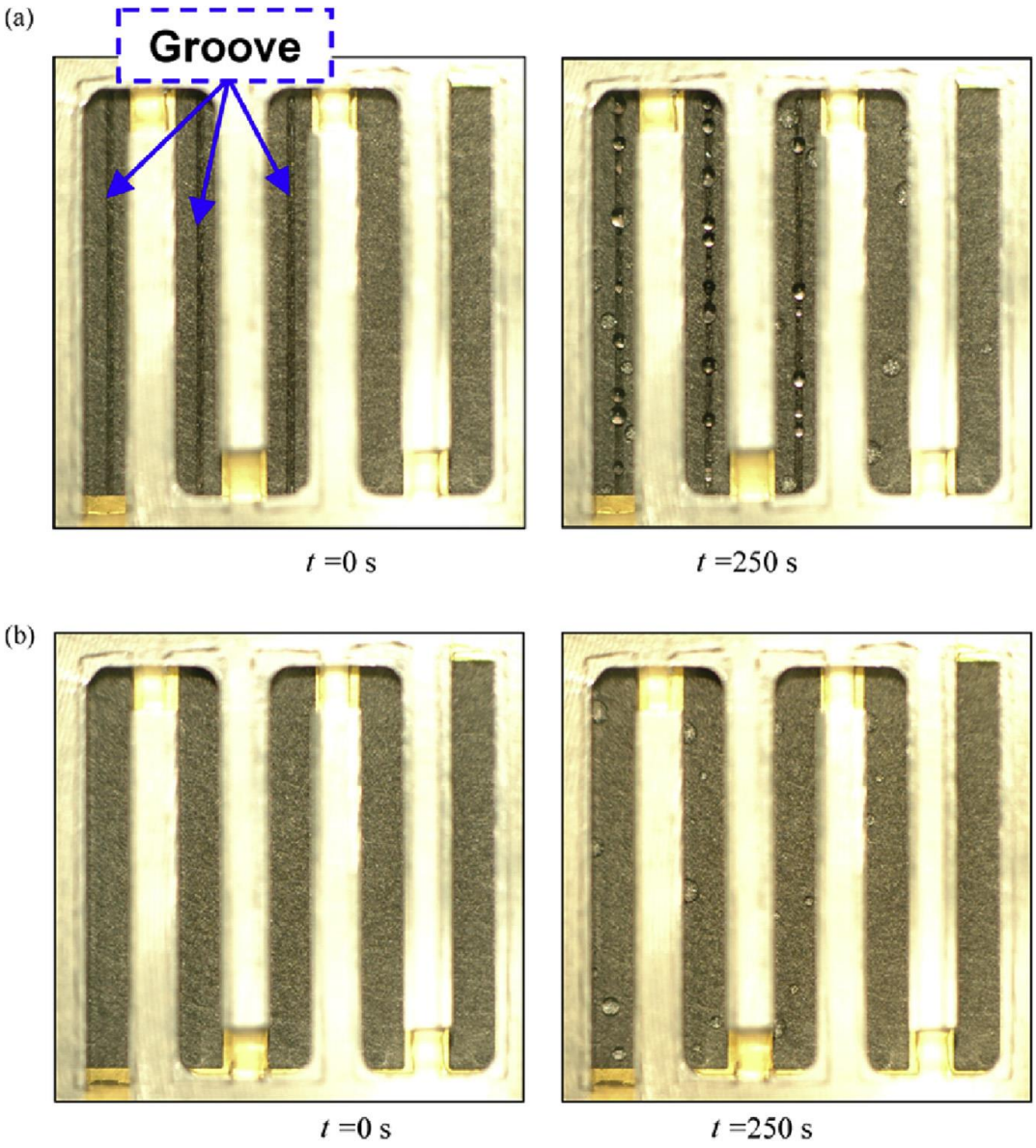

Figure 2-7 The effect of the grooved GDL on liquid water movement in the cathode GDL under the operating temperature of 5 °C and current density of 0.24 A/cm^2: (a) with grooves; (b) without grooves [84].

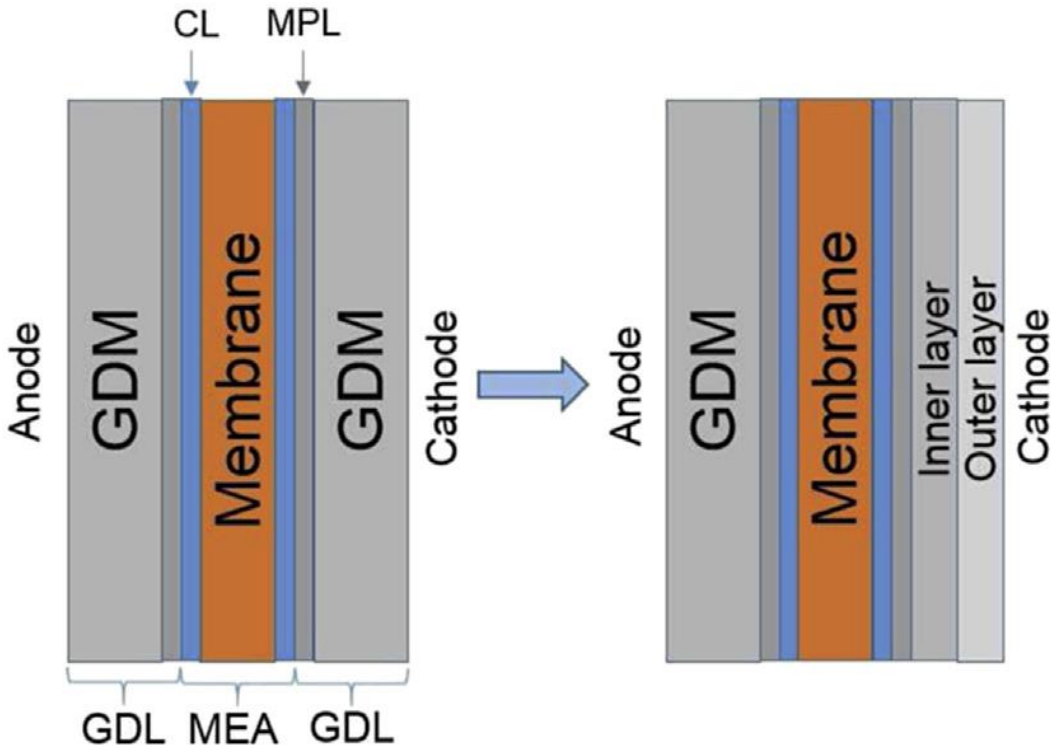

Figure 2-8 A schematic of a traditional PEMFC (left), and a PEMFC with a double-layer GDM in the cathode (right) [85].

working temperatures with the help of the grooves. Another typical method for improving the water management in the GDLs is to fabricate another layer within the GDLs. Wang et al. [85] fabricated a double-layer gas diffusion media (GDM), see Fig. 2-8. They found that the double-layer GDM with different polytetrafluoroethylene (PTFE) loadings can improve the water management within the PEMFCs. Other investigators have fabricated the double-layer with different properties, such as pore size [86]. In addition to the GDM, the use of double-layer MPLs has been widely investigated. Jeong et al. [87] proposed a design of double–layer MPL and one of the MPL layer is hydrophilic instead of hydrophobic. They tested the new MPL under two humidification conditions, i.e.

RH = 50% and 100%, and found that the use of hydrophobic/ hydrophilic double MPL can improve the water management in GDLs and thus increase the performance of the fuel cell. Similar conclusions on double-layer MPLs can also be found in [88,89].

Chapter 3: Numerical investigations on the overall performance of AB-PEMFCs

Summary

This chapter presents an efficient mathematical model for AB-PEMFCs. One of the main objectives of this study is to investigate the effects of hydrogen humidity, which is often neglected, on the performance of AB-PEMFCs. It is found that the heat transfer coefficient dictates the performance limiting mode of the AB-PEMFC, the modelled AB-PEMFC is limited by the dry-out of the membrane at high current densities. Also, the performance of the fuel cell is found to be mainly influenced by the hydrogen humidity. In addition, an optimal cathode GDL and relatively thinner anode GDL are favoured in order to achieve a good performance of the fuel cell.

3.1 Introduction

RH is one of the main factors associated with AB-PEMFCs performance. However, most of the studies on the effects of RH were conducted on conventional PEMFCs; for AB-PEMFCs, the number of investigations is less. In AB-PEMFCs, most of the studies on the effects of the operating conditions focus on the effect of the RH at the open cathode, assuming dry hydrogen is supplied to the anode of the fuel cell; see for example [90]. However, there have been very few investigations which have studied the effects of the anodic RH on the performance of the air-breathing PEM fuel cells; most of these investigations were experimental. Chu and Jiang [91] evaluated the performance of an air-breathing polymer electrolyte membrane fuel

cell (PEMFC) stack under different environmental conditions, and they showed that feeding humidified hydrogen to the anode slightly improves the PEMFC performance, even at low temperatures. Ho Jung et al. [35] examined the effect of the hydrophilicity of the anode catalyst layer on the performance of an air-breathing PEM fuel cell. The experimental results showed that a hydrophilic anode catalyst layer improves the cell performance through humidifying the anode side of the membrane and removing the water from the cathode. Hamel and Fréchette [92] suggested a simple steady-state model for the water transport through an air-breathing PEM fuel cell and an experimental characterisation was performed with direct injection of water at the anode. They showed that humidifying the anode had a positive effect on the performance of the cell, potentially even when the cathode is flooding. Ou et al. [93] tested an air-breathing PEM fuel cell with a humidity and temperature control system, and a bubble humidifier was utilized to humidify the inlet hydrogen in order to manage the water content of the membrane. The experimental results showed that the control method improves the output power of the fuel cell.

No modelling study has been conducted to investigate the effect of the anodic (hydrogen) RH on the performance of the AB-PEMFC. In this chapter, a mathematical model is built for an AB-PEMFC. The effect of the RH of the hydrogen on the cell performance is investigated and compared with that of the RH of ambient air at the open cathode. Also, the effect of the GDL thickness is examined, since the gas concentrations at the cathode catalyst layer and the membrane humidity condition are highly influenced by the GDL thickness.

3.2 Numerical model

The prototype of this built model was first described by O'Hayre et al. [94] and a schematic diagram of the modelled fuel cell is shown in Fig. 3-1. This fuel cell was selected because the temperature of the cathode GDL surface and the cell resistance were measured [95]. Therefore, in addition to the polarisation curves for the cell voltage, further data can be used to validate the proposed new model. The following assumptions have been taken into account when developing the model:

- The fuel cell operates in steady-state conditions.
- The air is treated as an ideal gas.
- The catalyst layer is infinitely thin and is therefore treated as an interface between the membrane and the GDL.
- Water only exits as vapour.
- The GDL material is assumed to be homogenous.
- The fuel cell is under a dead-end mode at the anode side.
- The water activity is uniform across the membrane and is in equilibrium with the water activity at the cathode catalyst layer.
- The thermal resistance of the collectors was found to be almost negligible, therefore the current collectors were not incorporated into the model.

The equations used in the model could be categorised into 3 groups: mass transfer; heat transfer; and closure relations. The equations for each groups are explained as follows.

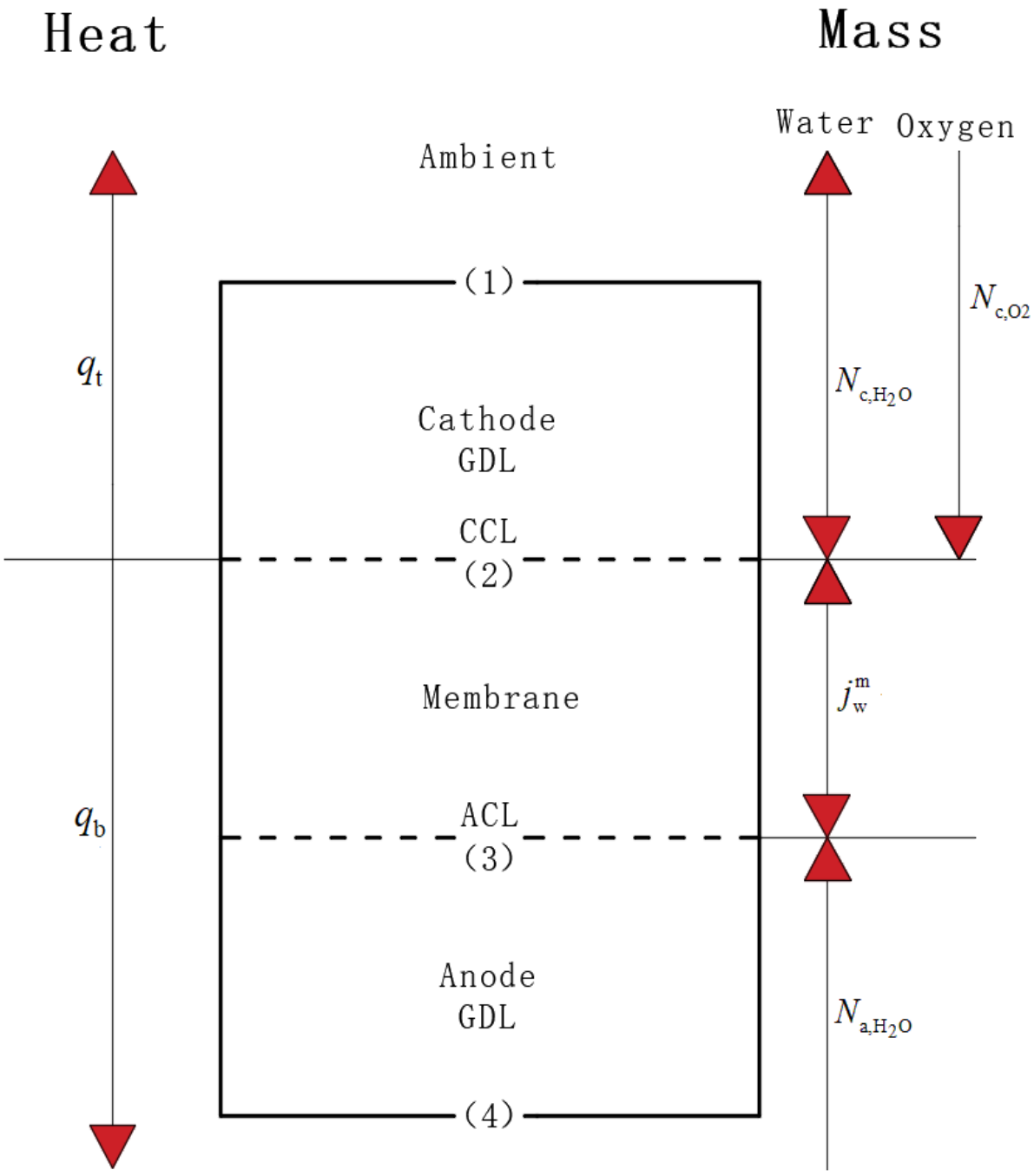

Figure 3-1 A schematic diagram of the modelled fuel cell. Each number represents an interface: (1) cathode GDL surface, (2) cathode catalyst layer, (3) anode catalyst layer and (4) anode GDL surface.

3.2.1 Mass transfer

On the cathode side, oxygen and water are mainly transported by natural convection in the ambient region next to the cathode GDL surface and by diffusion across the GDL. The convective molar flux of the species in the cathode, i.e. $N_{c,i}$, is given by:

$$N_{c,i} = h_{m,i}(C_{1,i} - C_{\infty,i}) \tag{3-1}$$

where the subscript i represents either oxygen (O_2) or water (H_2O), $C_{1,i}$ and $C_{\infty,i}$ are the molar concentrations of the species i at the surface of the cathode GDL and in the ambient region next to the cathode GDL, respectively. $h_{m,i}$ is the mass transfer coefficient of the species i and is obtained as follows:

$$h_{m,i} = \frac{Sh_i \cdot D_{ij}}{L_{ch,m}} \tag{3-2}$$

D_{ij} is the normal diffusion coefficient of the species i into j; the latter represents nitrogen (N_2). $L_{ch,m}$ is the characteristic length associated with the mass transfer, defined as the square root of the active area of the fuel cell. Sh_i is the Sherwood number, which is associated with the mass transfer, for the species i. It must be noted that the Lewis numbers for all simulation cases were found to be of the order of unity, so the analogy between heat and mass transfers is valid. Another important point to note is that the modelled fuel cell is horizontally-oriented with an upwards-facing open cathode and a uniform wall heat flux (UHF) boundary condition on the

surface of the cathode GDL is assumed. Therefore Sh_i is calculated by the following empirical equation [96]:

$$Sh_i = 0.16 Ra_{m,i}^{1/3} \tag{3-3}$$

The mass transfer-related Rayleigh number $Ra_{m,i}$ for the species i is given by:

$$Ra_{m,i} = \frac{g\beta_{m,i}(x_{1,i} - x_{\infty,i})L_{ch,m}^3}{\nu_i D_{ij}} \tag{3-4}$$

where g is the magnitude of the gravitational acceleration, ν_i is the kinematic viscosity of the species i, x_i is the mole fraction of the species i, and $\beta_{m,i}$ is the volumetric expansion coefficient of the species i. Since the molar concentration of nitrogen remains almost constant through the cathode GDL and the ambient region, we assume that a binary mixture of oxygen and water is transferred to the open cathode. Thus $\beta_{m,i}$ for the binary mixture is calculated as follows [96]:

$$\beta_{m,i} = \frac{M_{O_2} - M_{H_2O}}{M_{mix}} \tag{3-5}$$

where M_{O_2} and M_{H_2O} are the molecular weights of oxygen and water, respectively, M_{mix} is the molecular weight of the binary mixture and it is the arithmetic mean of the molecular weights of the mixture in the ambient region, $M_{\infty,mix}$, and at the cathode GDL surface, $M_{1,mix}$:

$$M_{mix} = \frac{M_{1,mix} + M_{\infty,mix}}{2} \tag{3-6}$$

$$M_{\infty,\mathrm{mix}} = \frac{C_{\infty,\mathrm{O_2}}}{C_{\infty,\mathrm{O_2}} + C_{\infty,\mathrm{H_2O}}} M_{\mathrm{O_2}} + \frac{C_{\infty,\mathrm{H_2O}}}{C_{\infty,\mathrm{O_2}} + C_{\infty,\mathrm{H_2O}}} M_{\mathrm{H_2O}} \tag{3-7}$$

$M_{1,\mathrm{mix}}$ can be calculated in the same manner. The molar concentration of the water in the ambient region, $C_{\infty,\mathrm{H_2O}}$, is given by:

$$C_{\infty,\mathrm{H_2O}} = \frac{P_{\mathrm{sat}} RH_{\infty}}{RT_{\infty}} \tag{3-8}$$

where R is the universal gas constant, RH_{∞} is the relative humidity in the ambient, T_{∞} is the ambient temperature, and P_{sat} is the saturation pressure of water vapour, obtained, in atm units, by the following formula [97]:

$$\begin{aligned}\log_{10} P_{\mathrm{sat}} = &-2.1794 + 0.02953(T_{\infty} - 273.15) - 9.1837\times10^{-5}(T_{\infty} - 273.15)^2 \\ &+ 1.4454\times10^{-7}(T_{\infty} - 273.15)^3\end{aligned} \tag{3-9}$$

The molar concentration of the oxygen in the ambient region, $C_{\infty,\mathrm{O_2}}$, is given by:

$$C_{\infty,\mathrm{O_2}} = 0.21(C_{\infty,\mathrm{tot}} - C_{\infty,\mathrm{H_2O}}) \tag{3-10}$$

where $C_{\infty,\mathrm{tot}}$ is the molar concentration of the air mixture in the ambient region and is given by:

$$C_{\infty,\mathrm{tot}} = \frac{P_{\infty}}{RT_{\infty}} \tag{3-11}$$

For the diffusion of water and oxygen across the cathode GDL, $N_{\mathrm{c,i}}$ is calculated as follows:

$$N_{\mathrm{c,i}} = D_{\mathrm{eff,ij}} \frac{C_{2,\mathrm{i}} - C_{1,\mathrm{i}}}{\delta_{\mathrm{GDL}}} \tag{3-12}$$

where $C_{2,i}$ is the molar concentration of the species i at the cathode catalyst layer, δ_{GDL} is the thickness of the GDL, $D_{eff,ij}$ is the effective diffusion coefficient, and it is obtained as follows [98]:

$$D_{\text{eff,ij}} = f(\varepsilon) D_{\text{ij}} \left(\frac{T_{\text{GDL}}}{T_{\text{ref}}}\right)^{1.5} \left(\frac{P_{\text{ref}}}{P}\right) \tag{3-13}$$

where T_{ref} and P_{ref} are the reference temperature and pressure, respectively. The pressure ratio (P_{ref} / P) is set to be unity since the operation pressure is the same as the reference pressure, i.e. 1 atm. T_{GDL} is the temperature of the cathode GDL, and is the arithmetic mean of the temperatures at the cathode GDL surface, T_1, and at the cathode catalyst layer, T_2. $f(\varepsilon)$ is the factor that corrects for the geometry and is a function of the porosity of the medium, ε. Instead of using the normally applied Bruggmann correlation, $f(\varepsilon)$ is calculated by a more accurate correlation developed for GDLs [99]:

$$f(\varepsilon) = 0.008 e^{4.81\varepsilon} \tag{3-14}$$

At the anode side, water and hydrogen are mainly transported by diffusion across the anode GDL. It should be noted that the concentration of oxygen at the cathode electrode is relatively small due to the low mass transfer coefficient, thus the hydrogen supplied at the anode is usually sufficient for the operation of the air-breathing fuel cell. Thus, the transport of hydrogen is not considered in the model and subsequently the anodic activation losses are neglected. The molar flux of water across the anodic GDL, i.e. N_{a,H_2O}, is given by:

$$N_{a,H_2O} = D_{eff,ij} \frac{C_{4,H_2O} - C_{3,H_2O}}{\delta_{GDL}} \tag{3-15}$$

Likewise, the effective diffusion coefficient $D_{eff,ij}$ can be calculated using Eq. (3-13) and Eq. (3-14). D_{ij} is the normal diffusion coefficient of water vapour into hydrogen as the latter, volume-wise, makes up most of the gas mixture at the anode. C_{3,H_2O} and C_{4,H_2O} are the molar concentrations of water at the anode catalyst layer and at the anode GDL surface. Since the gas mixture at the anode side is treated as an ideal gas, C_{4,H_2O} can be obtained by employing Eq. (3-8) and Eq. (3-9).

Water is transported through the membrane by three different processes, namely: water diffusion, electro-osmosis drag and water convection. The diffusion of water is caused by the concentration gradient and this is usually from the cathode to the anode due to the water being produced at the cathode catalyst layer. The electro-osmosis drag occurs because of the conjugated transport of the water molecules with the protons. The convection of water is caused by the pressure gradient [100]. Since water only exits as a vapour in this model, water convection is neglected and therefore the total water flux through the membrane from the anode to the cathode is given by [101]:

$$j_w^m = -D_w^m \frac{C_{2,H_2O} - C_{3,H_2O}}{\delta_{mem}} + n_d \frac{I}{F} \tag{3-16}$$

where I is the current density and F is the Faraday's constant. It should be noted that, for simplification, the catalyst layers are treated as interfaces between the membrane and the GDL and therefore the concentrations of water at the cathode and anode sides of the membrane were assumed to be of those of the cathode and

anode catalyst layers respectively, i.e. $C_{2,\mathrm{H_2O}}$ and $C_{3,\mathrm{H_2O}}$. The diffusion coefficient, $D_{\mathrm{w}}^{\mathrm{m}}$, and electro-osmotic drag coefficient, n_{d}, are dependent on the water content of the membrane, λ, and are given by [101]:

$$D_{\mathrm{w}}^{\mathrm{m}} = \begin{cases} 3.1\times10^{-7}\lambda\left[\exp(0.28\lambda)-1\right]\exp(-\dfrac{2346}{T_{\mathrm{mem}}}) & \text{if } 0<\lambda<3 \\ 4.17\times10^{-8}\lambda\left[161\exp(-\lambda)+1\right]\exp(-\dfrac{2346}{T_{\mathrm{mem}}}) & \text{if } 3\le\lambda<17 \end{cases} \tag{3-17}$$

$$n_{\mathrm{d}} = \begin{cases} 1 & \text{if } \lambda \le 14 \\ 0.1875\lambda - 1.625 & \text{otherwise} \end{cases} \tag{3-18}$$

The water content of the membrane, λ, is calculated by:

$$\lambda = \begin{cases} 0.043+17.81a-39.85a^2+36.0a^3 & \text{if } 0\le a\le 1 \\ 14.0+1.4(a-1) & \text{if } 1<a\le 3 \end{cases} \tag{3-19}$$

where a is the water activity in the membrane which, as indicated in the assumptions, is assumed to be uniform across the membrane and is in equilibrium with the water activity at the cathode catalyst layer and a is given by:

$$a = \frac{P_{2,\mathrm{H2O}}}{P_{2,\mathrm{sat}}} \tag{3-20}$$

where $P_{2,\mathrm{sat}}$ is the saturation pressure of the water vapour at the cathode catalyst layer, obtained using Eq. (3-9), and $P_{2,\mathrm{H_2O}}$ is the partial pressure of the water vapour at the cathode catalyst layer, and is given by:

$$P_{2,\mathrm{H2O}} = C_{2,\mathrm{H_2O}} R T_2 \tag{3-21}$$

In the modelled fuel cell, water is transported between the anode and cathode sides of the membrane and also between the ambient and the cathode catalyst layer. It is also produced at the cathode catalyst layer. Thus, the transport of water in the fuel cell, based on Faraday's second law of electrolysis and the model proposed by Berg et al. [102], is governed by:

$$N_{\mathrm{a,H_2O}} = j_{\mathrm{w}}^{\mathrm{m}} \tag{3-22}$$

for the anode side, and by:

$$N_{\mathrm{c,H_2O}} = j_{\mathrm{w}}^{\mathrm{m}} + \frac{I}{2F} \tag{3-23}$$

for the cathode side. On the other hand, oxygen transports through cathode GDL between the ambient and the cathode catalyst layer and therefore its transport is governed by the following equation:

$$N_{\mathrm{c,O_2}} = \frac{I}{4F} \tag{3-24}$$

3.2.2 Heat transfer

The heat generated is assumed to be released only from the cathode catalyst layer as most of the heat sources exist. Therefore, the heat is mainly transported by conduction in the GDLs and the membrane; and by natural convection in the ambient region next to the GDL surfaces.

The convective heat flux at the interface between the ambient and the cathode GDL, q_{t}, is given by:

$$q_t = h_c(T_1 - T_\infty) \tag{3-25}$$

where h_c is the heat transfer coefficient at the surface of the cathode GDL, which is the sum of the natural convection coefficient, $h_{c,con}$, and the radiative coefficient, $h_{c,rad}$:

$$h_c = h_{c,con} + h_{c,rad} \tag{3-26}$$

$$h_{c,rad} = 2e\sigma_{Bolt}(T_1^2 + T_\infty^2)(T_1 + T_\infty) \tag{3-27}$$

$$h_{c,con} = \frac{Nu_c \cdot k_{c,air}}{L_{ch,h}} \tag{3-28}$$

where e is the emissivity, σ_{Bolt} is the Stephan-Boltzmann constant, $k_{c,air}$ is the thermal conductivity of air, $L_{ch,h}$ is the characteristic length for heat transfer, and Nu_c is the Nusselt number. As mentioned in the mass transfer section, the fuel cell is assumed to represent a horizontally-oriented heated plate with UHF boundary condition. Nu_c and the relevant Rayleigh number, $Ra_{h,c}$ are then given by [96]:

$$Nu_c = 0.16Ra_{h,c}^{1/3} \tag{3-29}$$

$$Ra_{h,c} = \frac{g\beta_c q_c L_{ch,h}^{\ 4}}{\nu_{c,air}\alpha_{c,air}k_{c,air}} \tag{3-30}$$

The kinematic viscosity $\nu_{c,air}$, the thermal diffusivity $\alpha_{c,air}$ and the thermal conductivity $k_{c,air}$ of the air have been all estimated using the tabulated data [103] at the film temperature, $T_{c,f}$, which is the arithmetic mean of the temperatures of

the cathode GDL surface, T_1, and the ambient region, T_∞ . The thermal expansion coefficient, β_c , is calculated as follows:

$$\beta_c = \frac{1}{T_{c,f}} \tag{3-31}$$

The convective heat flux at the bottom of the fuel cell, q_b , is calculated in the same manner using Eq. (3-25) – (3-31).

With the given thermal conductivities and thicknesses of the GDL and the membrane, i.e. k_{GDL} , δ_{GDL} , k_{mem} and δ_{mem} , The conductive heat fluxes in the GDLs and the membrane are given by:

$$q_t = k_{GDL} \frac{T_2 - T_1}{\delta_{GDL}} \tag{3-32}$$

$$q_b = k_{mem} \frac{T_2 - T_3}{\delta_{mem}} = k_{GDL} \frac{T_3 - T_4}{\delta_{GDL}} \tag{3-33}$$

where k_{GDL} and k_{mem} are the thermal conductivities of the GDL and the membrane, respectively, and δ_{GDL} and δ_{mem} are the thicknesses of the GDL and the membrane, respectively.

3.2.3 Closure relations

The cell potential E is expressed as follows:

$$E = E_o - \eta_{act} - \eta_{ohmic} \tag{3-34}$$

where E_o is the thermodynamic equilibrium voltage, η_{act} is the activation loss, and

η_{ohmic} is the ohmic loss. It should be noted that the concentration losses, mainly caused by water flooding, has not been considered in this model as the water activity was found to be always less than unity at the high current densities in all the investigated cases, thus signifying the absence of water flooding. The thermodynamic equilibrium voltage E_o is given by the Nernst equation:

$$E_o = \frac{-\Delta H + T\Delta S}{nF} + \frac{RT}{nF}\ln\left(\frac{P_{\text{H}_2} \cdot P_{\text{O}_2}^{0.5}}{P_{\text{H}_2\text{O}}}\right) \tag{3-35}$$

where ΔH and ΔS are the enthalpy and the entropy changes for the fuel cell reaction, respectively. P_{H_2} (1 atm), P_{O_2} (0.21 atm) and $P_{\text{H}_2\text{O}}$ (usually assumed to be 1 atm) are the partial pressures of hydrogen, oxygen and water under thermodynamic equilibrium. The activation losses, η_{act} , and the ohmic losses, η_{ohmic} , are given by:

$$\eta_{\text{act}} = \frac{RT_2}{2\alpha_{\text{ch}}F}\ln\left(\frac{C_{\infty,\text{O}_2} I}{C_{2,\text{O}_2} I_o}\right) \tag{3-36}$$

$$\eta_{\text{ohmic}} = IA(R_{\text{elec}} + R_{\text{mem}}) \tag{3-37}$$

where α_{ch} is the charge transfer coefficient, I_o is the reference exchange current density and R_{elec} is the lumped cell resistance of the fuel cell. These three parameters have been obtained from the experimental data [94]. A is the active area of the fuel cell and R_{mem} is the resistance of the membrane, obtained as follows:

$$R_{\text{mem}} = \frac{\delta_{\text{mem}}}{A\sigma_{\text{mem}}} \tag{3-38}$$

where σ_{mem} is the ionic conductivity of the membrane. The ionic resistance of the catalyst layer is neglected in the model because two cases where the catalyst layer resistance is included and excluded in the model have been investigated and it is found that the effect of this resistance is negligible. Because the widely-used Springer model [97] for calculating the ionic conductivity of the membrane was found to be rather inaccurate under low humidity conditions, another empirical formula is normally used for the modelled air-breathing fuel cells [104]:

$$\sigma_{\text{mem}} = (3.46a^3 + 0.0161a^2 + 1.42a - 0.175) \times \exp\left[1268\left(\frac{1}{303} - \frac{1}{T_2}\right)\right] \tag{3-39}$$

The total heat flux in the fuel cell is given by:

$$q = I(\eta_{\text{act}} + \eta_{ohmic} + \frac{T\Delta S}{2F}) = q_{\text{t}} + q_{\text{b}} \tag{3-40}$$

The simulations in this study were implemented using MATLAB R2017b and all the nonlinear algebraic equations were solved by 'fsolve'. The time taken for the convergence using a 3.20 GHz Intel(R) Xeon(R) E3 CPU and 16.00 GB RAM was remarkably small: 4 s, indicating the efficiency of the developed model. All the physical and geometrical parameters considered in the model are given in Table 3-1.

Table 3-1 Values of the parameters applied in the simulations. Unless otherwise stated, the values of the parameters were taken from the experiment data [94,95].

Parameter	**Value**
Faraday's constant, F	96,485 C mol^{-1}
Magnitude of gravitational acceleration, g	9.81 m s^{-2}
Universal gas constant, R	8.314 J mol^{-1} K^{-1}
Stephan-Boltzmann constant, σ_{Bolt}	5.67×10^{-8} W m^{-2} K^{-4}
Enthalpy change of fuel cell reaction, ΔH	-241.98 kJ mol^{-1}
Entropy change of fuel cell reaction, ΔS	-44.43 J mol^{-1} K^{-1}
Diffusivity of oxygen in nitrogen, $D_{O_2-N_2}$	2.2×10^{-5} m^2 s^{-1}
Diffusivity of water vapour in nitrogen, $D_{H_2O-N_2}$	2.56×10^{-5} m^2 s^{-1}
Diffusivity of water vapour in hydrogen, $D_{H_2O-H_2}$	1.02×10^{-4} m^2 s^{-1} [105]
GDL thickness, δ_{GDL}	3.0×10^{-4} m
Membrane thickness, δ_{mem}	5.2×10^{-5} m
GDL thermal conductivity, k_{GDL}	1 W m^{-1} K^{-1}
Membrane conductivity, k_{mem}	0.17 W m^{-1} K^{-1}
GDL porosity, ε	0.4
Emissivity, e	0.9
Active area of fuel cell, A	9.0×10^{-4} m^2
Characteristic length for mass transfer, $L_{\text{ch,m}}$	3.0×10^{-2} m
Characteristic length for heat transfer, $L_{\text{ch,h}}$	7.0×10^{-2} m
Lumped electrical resistance of the fuel cell, R_{elec}	0.012 Ω
Charge transfer coefficient, α_{ch}	0.41
Reference exchange current density, I_0	3.0×10^{-3} A m^{-2}

3.3 Results and discussion

3.3.1 Model validation

To validate the model, the modelling data obtained from the present model are compared with the experimental data reported by Fabian et al. [43]. It should be noted that although this work was performed some time ago, it is still regarded by many as the benchmark work [106,107]. Fig. 3-2(a) shows the polarization curves produced by the model at two ambient temperatures (i.e. 10 and 30°C) and a constant ambient relative humidity of 40%. One can observe from the figure that the modelling data are in good agreement with the experimental data and that the sharp decline in the cell voltage at high current densities is well captured by the model.

Fig. 3-2(b) and 3-2(c) show the cell resistance and the temperature of the cathode GDL surface as a function of the current density for 10 and 30°C ambient temperatures and an ambient relative humidity of 40%. Similarly, good agreement is obtained between the experimental and the modelling data, imparting confidence on the reliability of the model. Further, Fig. 3-2(a) and 3-2(b) show that there is a sharp decline in the cell voltage and a steep increase in the cell resistance and these coincide. This means that the cell resistance is the main reason for limiting the air-breathing fuel cell performance at high current densities.

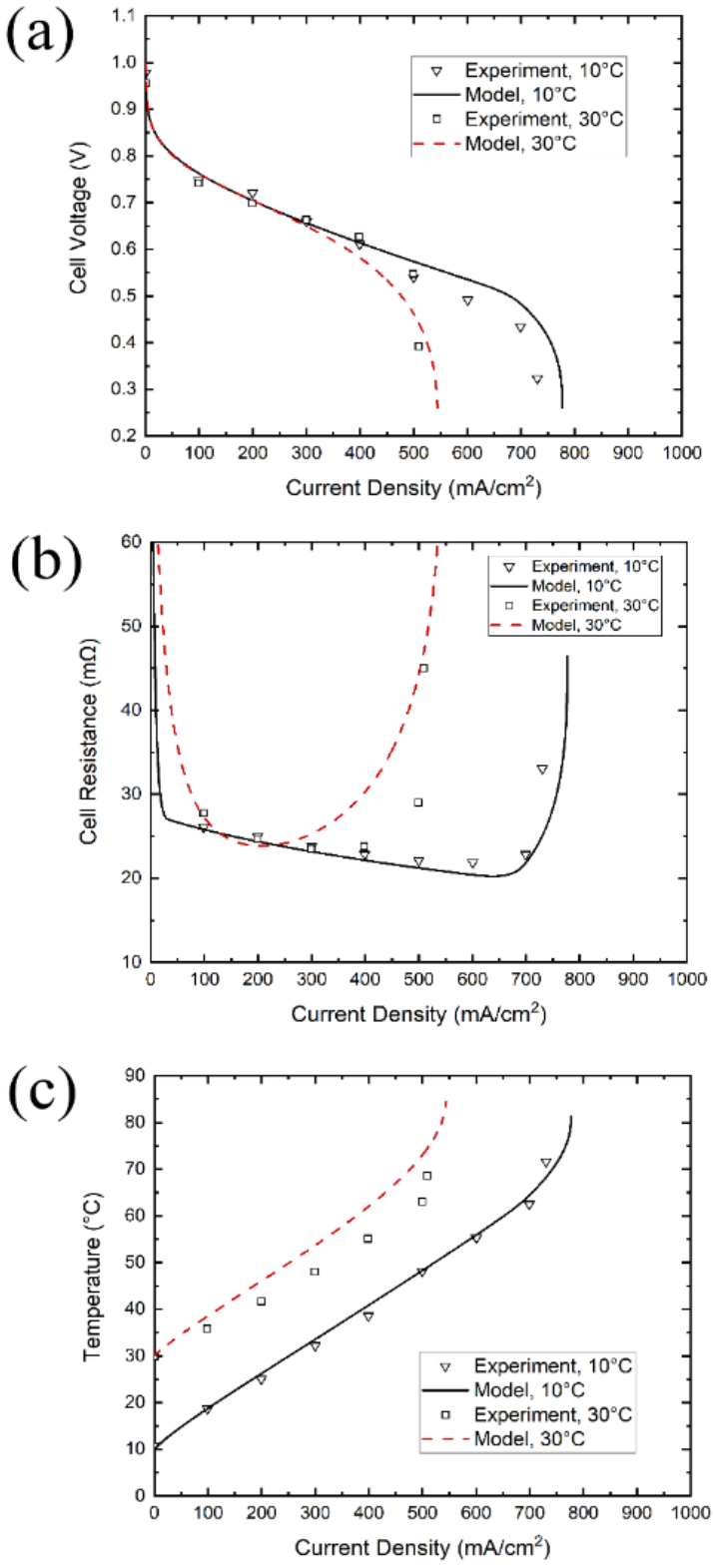

Figure 3-2 (a) The cell voltage, (b) cell resistance and (c) GDL surface temperature as a function of the current density for an air-breathing fuel cell operating at 40% ambient relative humidity and ambient temperatures of 10 and 30°C.

3.3.2 Status of the water

It is clear from the previous section that the air-breathing fuel cell is limited mainly by the membrane ohmic resistance at high current densities and thus the performance of the fuel cell increases with decreasing the fuel cell temperature. This must be compared with conventional fuel cells, where the performance is normally limited by water flooding. Therefore, it is of much interest to analyse the status of liquid water at the cathode of the modelled fuel cell; Fig. 3-3 shows the rates of generation and removal of water (which is equivalent to the water flux at the surface of the cathode GDL), respectively.

Depending upon the relative magnitudes of the water generation and removal rates, the cathode of the fuel cell is said to be under: (i) self-humidification in the low current density region (< 50 mA/cm²) where the difference between the higher rate of water removal and the lower rate of water generation decreases with increasing current density, (ii) water flooding in the intermediate current density region (between 50 and 450 mA/cm²) where the rate of generation of water is always more than the rate of water removal, and (iii) membrane dry-out in the high current density region (> 450 mA/cm²) where the rate of water removal is always more than that of water generation and the difference between the two rates increases as the current density increases. Clearly, fuel cells with such profile, caused by the relatively low heat transfer coefficient, is limited by the dry-out of the membrane, and the higher fuel cell temperature will cause more serious water flooding and thus decrease the fuel cell performance.

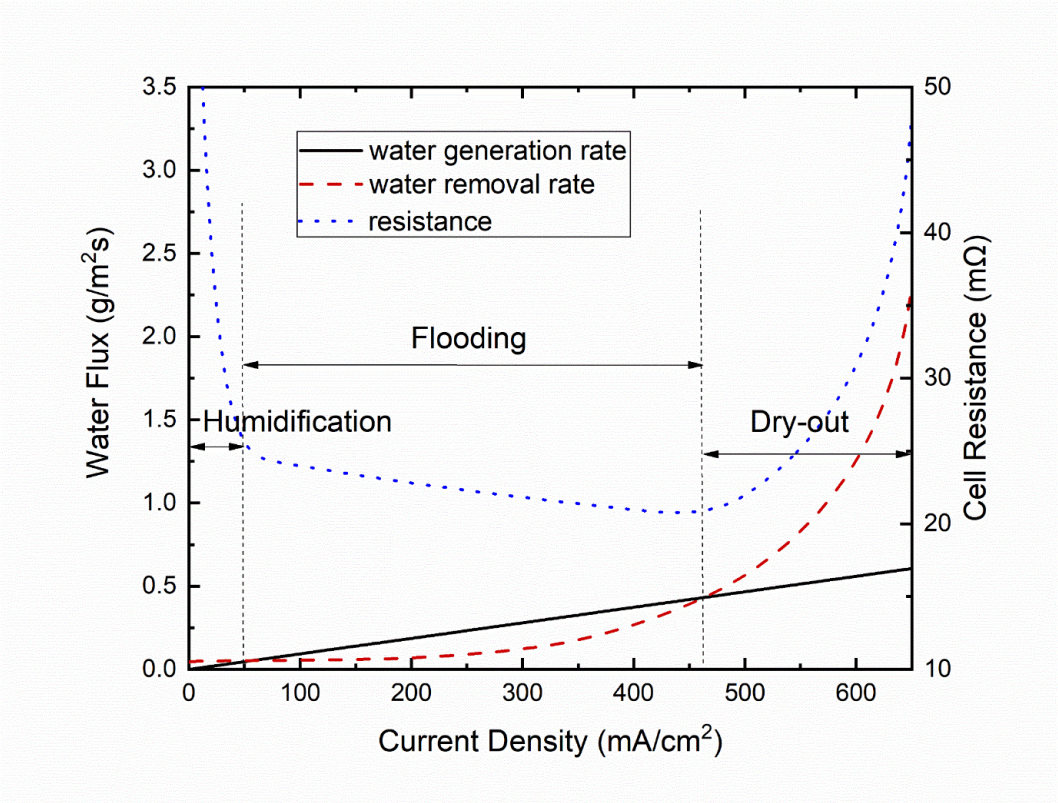

Figure 3-3 The water generation rate, the cathode water removal rate and the cell resistance as a function of the current density.

In order to determine the sensitivity of the fuel cell performance to the heat transfer coefficient, this coefficient has been increased by a factor of 3. From Fig. 3-4, it is clear that the cathode of the fuel cell operates under: (i) self-humidification in the low current density region (< 40 mA/cm²) and (ii) water flooding in the current density larger than 40 mA/cm². Unlike the profile shown in Fig. 3-3, the performance of the fuel cell with higher heat transfer coefficient is limited by water flooding at high current densities which is commonly encountered when operating conventional PEM fuel cells.

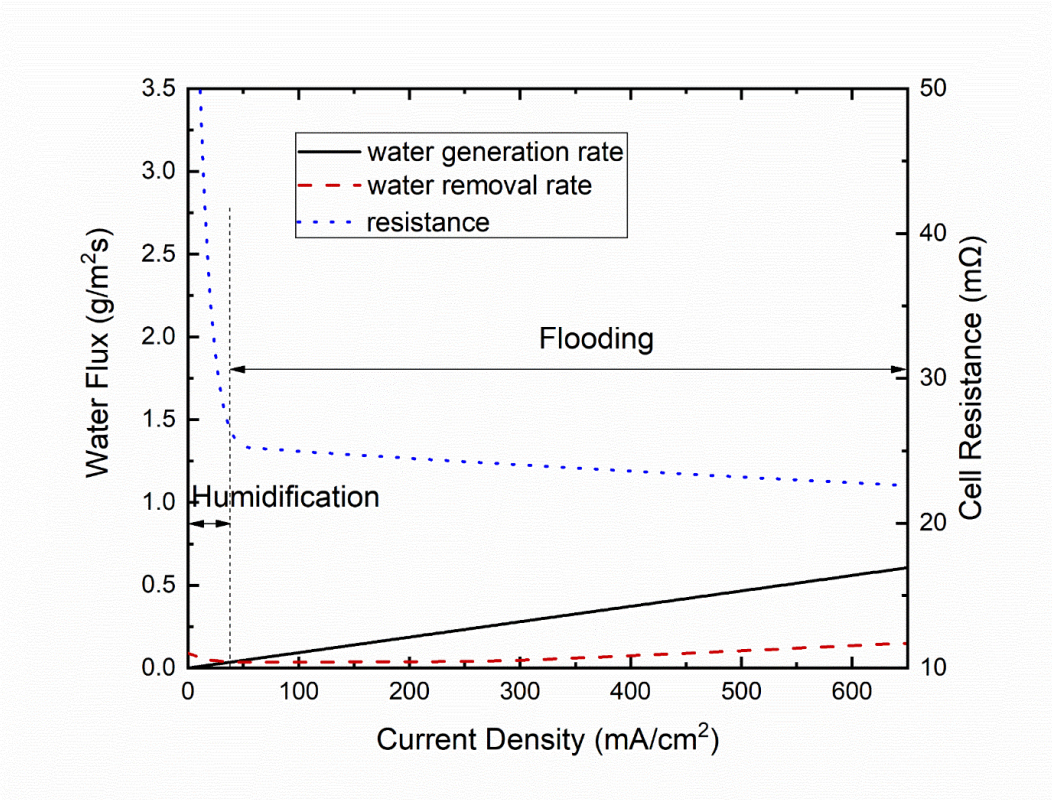

Figure 3-4 The water generation rate, the cathode water removal rate and the cell resistance as a function of the current density for the fuel cell with a 3 times larger heat transfer coefficient.

3.3.3 Effect of the operating conditions

The effect of the humidity at the anode is often neglected when modelling air-breathing PEM fuel cells as hydrogen is normally assumed to be dry. In this section, the effects of both the cathodic relative humidity (the ambient relative humidity) and the anodic relative humidity on the performance of the air-breathing fuel cell are examined.

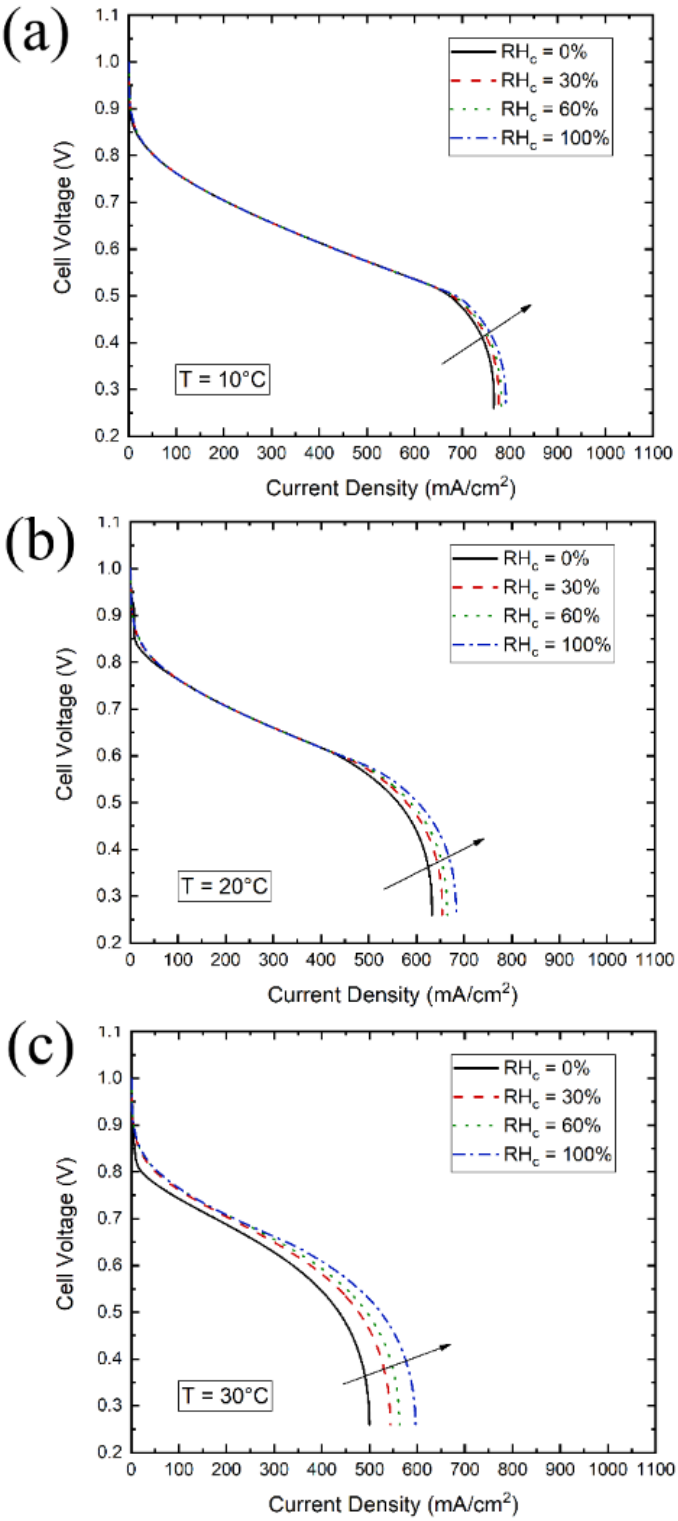

Figure 3-5 Effect of the ambient relative humidity at the cathode on the cell performance at zero anodic (hydrogen) relative humidity and three ambient temperatures: (a) 10°C, (b) 20°C and (c) 30°C.

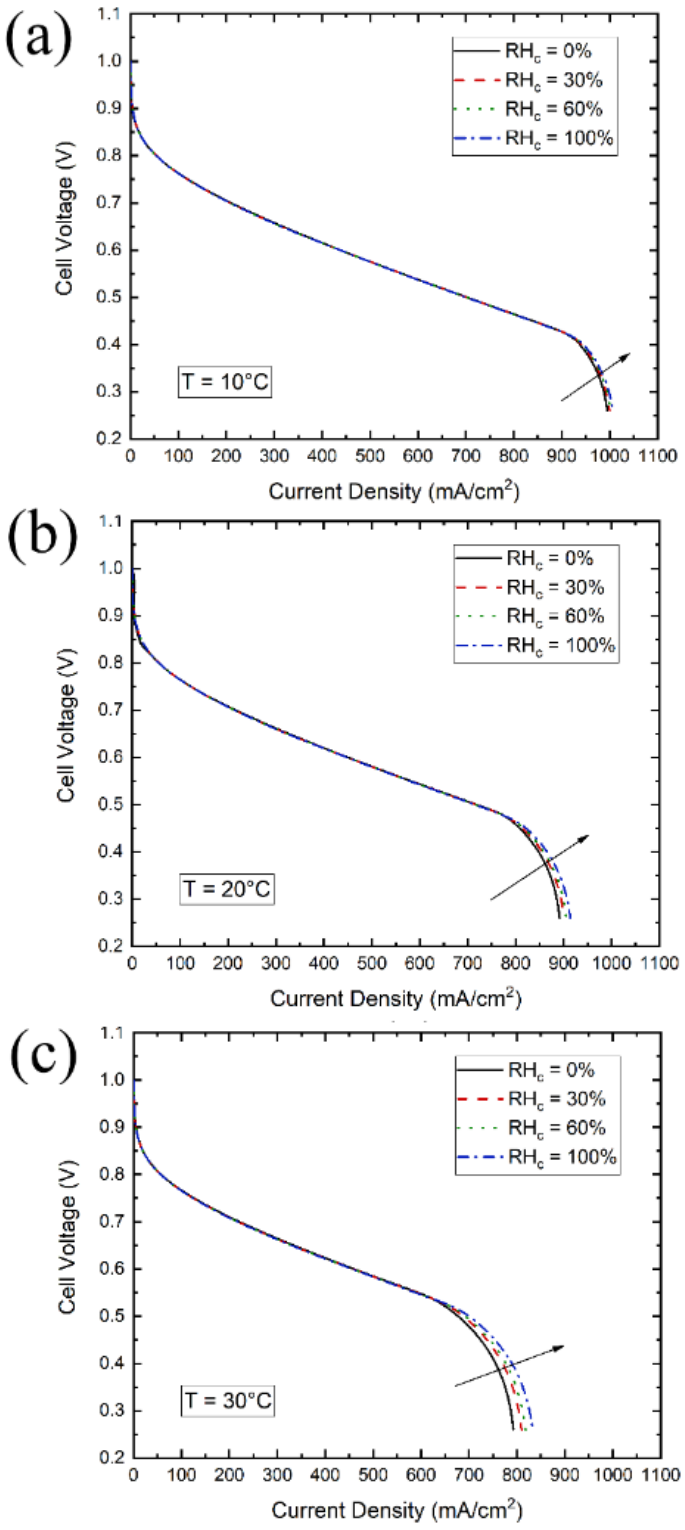

Figure 3-6 Effect of the ambient relative humidity at the cathode on the cell performance at 100% anodic (hydrogen) relative humidity and three ambient temperatures: (a) 10°C, (b) 20°C and (c) 30 °C.

3.3.3.1 Ambient RH

Figs. 3-5 and 3-6 show the effect of the ambient relative humidity. For dry hydrogen (Fig. 3-5), the cell performance increases slightly with increasing ambient relative humidity, and with fully humidified hydrogen (Fig. 3-6), the performance gain is even smaller.

3.3.3.2 Hydrogen RH

Figs. 3-7 and 3-8 show the effect of the anodic relative humidity. It is evident that increasing the anode humidity greatly improves the performance of the fuel cell. For example, when the anodic relative humidity increases from 0 to 100% in Fig. 3-7(c), the limiting current density increases by more than 40% at 0.3V. Clearly, one of the ways to mitigate membrane dry-out problem at high current density, which has been discussed in Section 3.3.2, and subsequently enhance the fuel cell performance is to increase the relative humidity of hydrogen.

It also can be seen from Figs. 3-5 and 3-7, the performance improvement attributed to the increase in the anodic relative humidity is clearly larger than that attributed to the increase in the ambient relative humidity. Also we can observe that this improvement is only very slightly influenced by the humidity situation at the cathode side (see Figs. 3-7 and 3-8). Further, it is observed that for all the cases investigated, the performance improvement is more significant at higher ambient temperatures, and this is due to lower membrane humidification with higher ambient temperatures.

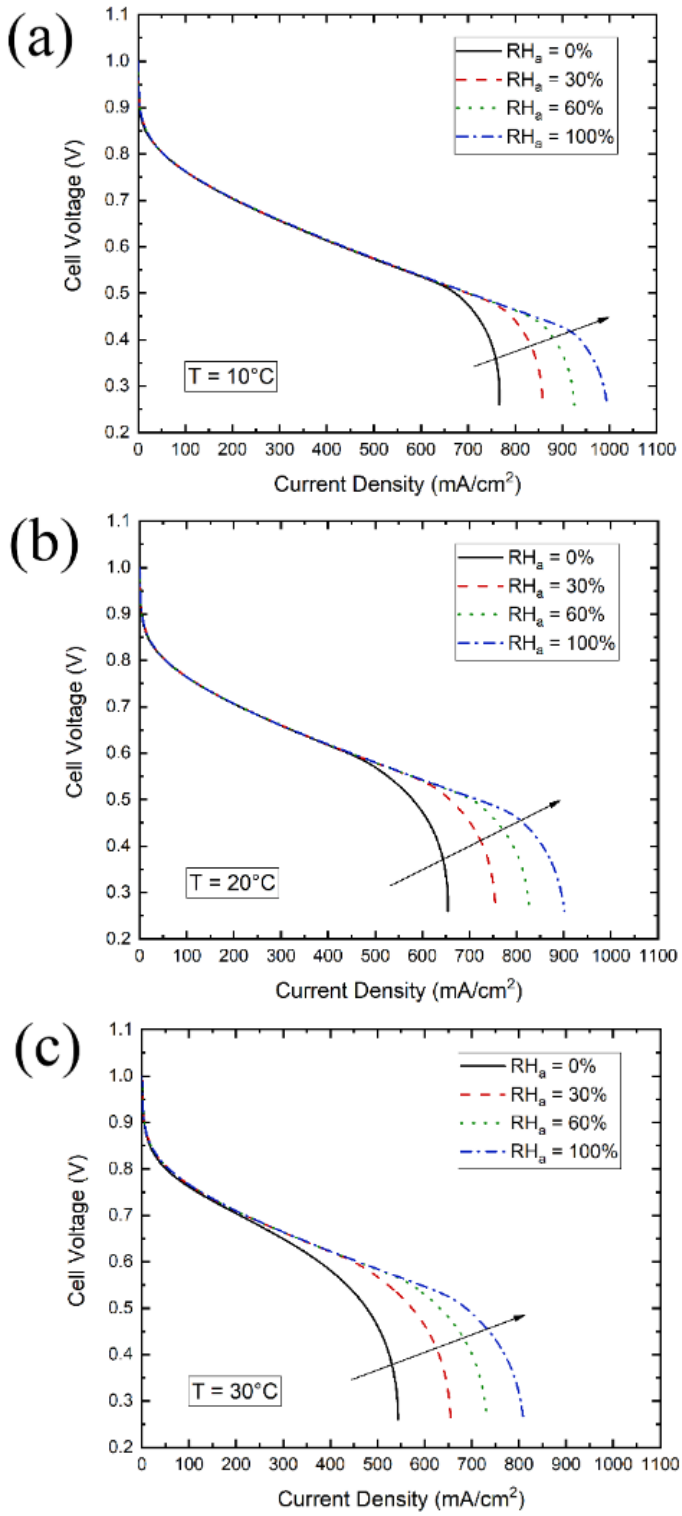

Figure 3-7 Effect of the anode (hydrogen) relative humidity on the cell performance at zero cathode relative humidity and three ambient temperatures: (a) 10°C, (b) 20°C and (c) 30°C.

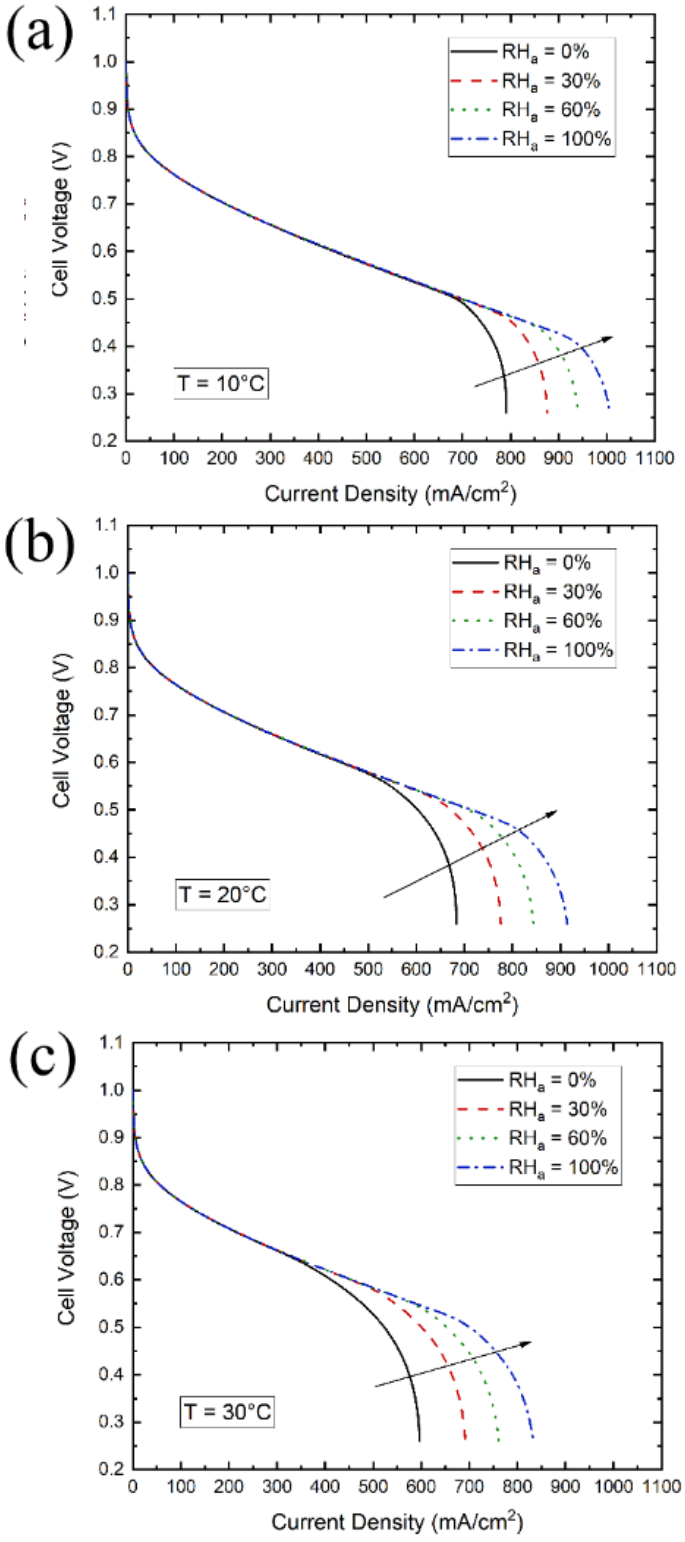

Figure 3-8 Effect of the anode (hydrogen) relative humidity on the cell performance at 100% cathode relative humidity and three ambient temperatures: (a) 10°C, (b) 20°C and (c) 30°C.

3.3.3.3 Water flooding

As mentioned in Section 3.2, water flooding has not been considered in the model. The increase in both the anode and cathode relative humidity normally cause water flooding at the cathode side of conventional fuel cells particularly at high current densities where the rate of water production is relatively high.

To better understand the effect of the hydrogen relative humidity on water flooding, a figure that shows the accumulating liquid water at the cathode catalyst layer as a function of current density is generated; see Fig. 3-9. For all the investigated cases, the ambient relative humidity and temperature were selected to be 40% and 20°C, respectively, as they are more or less the normal indoor conditions. It should be noted that no temperature control equipment is included in the model, since the

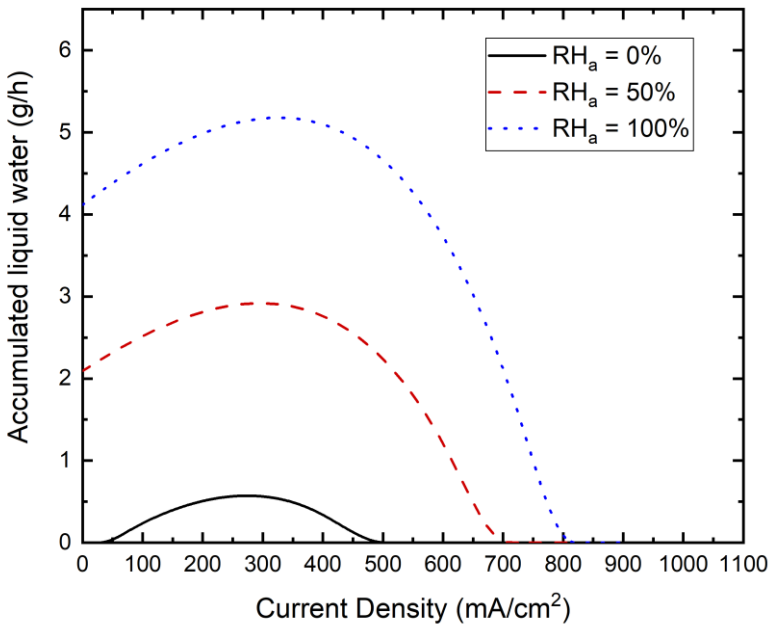

Figure 3-9 The accumulating liquid water at the cathode catalyst layer as a function of the current density for the fuel cell operating at different anode (hydrogen) relative humidities.

air-breathing fuel cell is designed to power small electronic devices where the ancillary components are required to be removed to simplify the system and subsequently boost its competitiveness. It can be seen from the figure that the increase in the relative humidity of hydrogen causes more water to accumulate at the cathode catalyst layer; delaying the occurrence of the limiting current density.

Water activity, which is the ratio between the partial pressure of the water vapour and the saturation pressure of the water vapour, can be also used to confirm whether there exists liquid water. Fig. 3-10 shows the water activity of the cathode catalyst layer and GDL surface as a function of the anode relative humidity at relatively low cell voltages (i.e. 0.4, 0.3 and 0.2V). Overall, it can be observed that the water activity slightly increases with increasing anodic relative humidity. For example, at 0.4V the water activity of the catalyst layer increases only by 20% when increasing the anodic relative humidity from 0% to 100%. It can be noted that, in all the simulated cases shown in Fig. 3-10, the water activity is less than unity, and this indicates that no liquid water is produced at the cathode side. Therefore, the increase in the anodic relative humidity does not cause water flooding at high current densities.

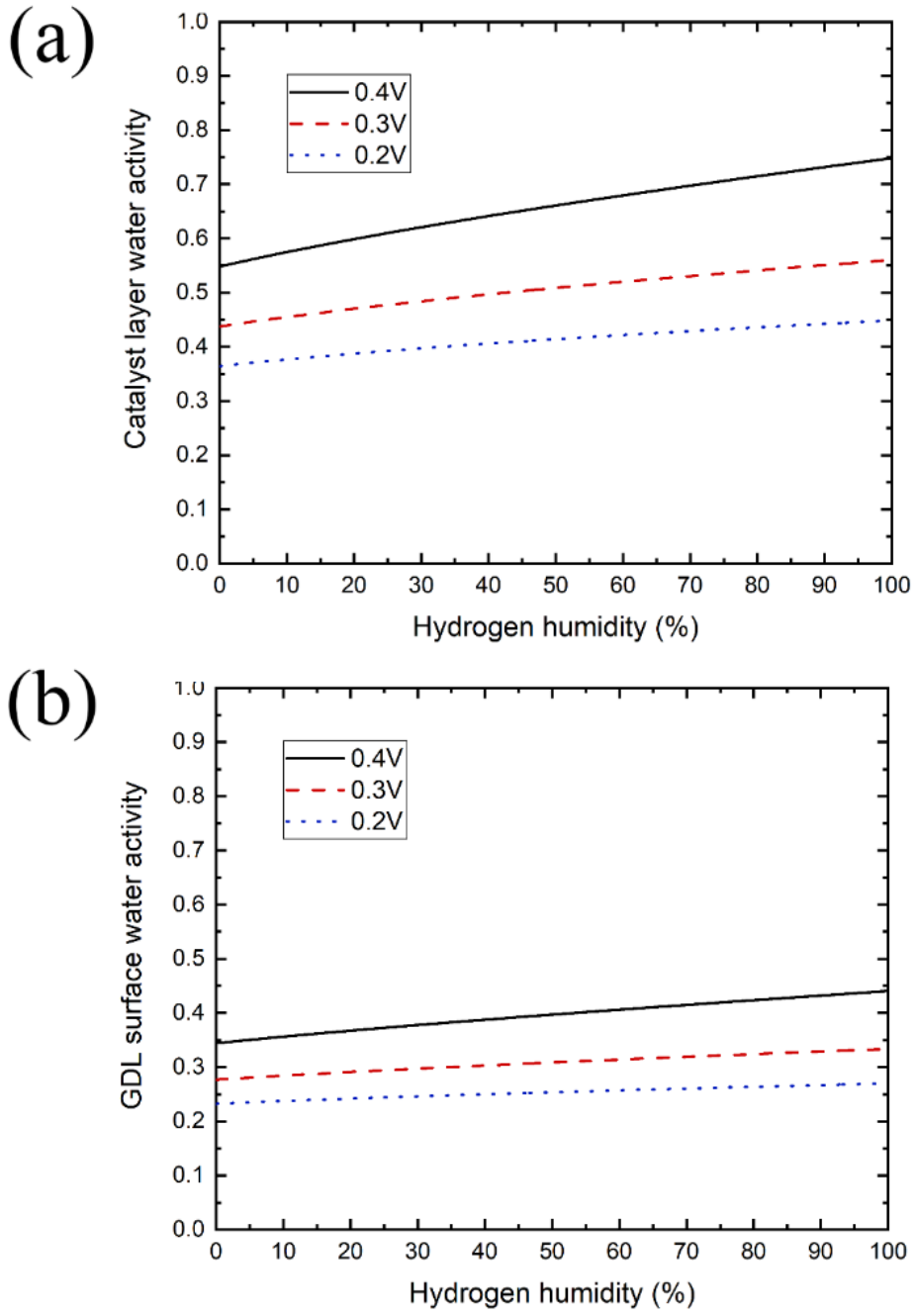

Figure 3-10 Effect of anodic (hydrogen) relative humidity on the water activity at relatively low cell voltages and at (a) cathode catalyst layer and (b) cathode GDL surface.

3.3.4 Effect of the GDL

The results presented in Section 3.3.3 show that the increase in the anodic relative humidity improves the performance of the air-breathing fuel cell by increasing the water vapour concentration at the cathode catalyst layer and subsequently its ionic conductivity. Also, the variation of GDL thickness can influence the diffusion of the water vapour at the cathode and thus change the water vapour concentration. For dry and fully humidified hydrogen, the effects of GDL thickness on the cell performance are investigated.

It can be seen that, from Fig. 3-11, the most appropriate GDL thickness, at either the cathode or anode, for operation of the air-breathing fuel cell is different at two humidity conditions at the anode side. For the dry condition, a thicker GDL is favoured, e.g. 0.8 mm thickness; see Fig. 3-11(a). While for the fully humidified condition, the cell performs better with a thinner GDL, i.e. 0.2 mm thickness; see Fig. 3-11(b). The thickness of the GDL mainly influences the diffusion of the water vapour and oxygen. The cell performance is largely dependent on the concentrations of these two gases and therefore it is necessary to investigate the relationships between these concentrations and the GDL thickness.

Fig. 3-12 shows the effect of the GDL thickness on the gas concentrations at 0.4V and at two humidity conditions. For the dry condition (Fig. 3-12(a)), we can observe that the GDL thickness has opposite effect on the concentrations of water and oxygen. This is because, at the fuel cell cathode side, the water is transported from where it is produced at the cathode catalyst layer towards the ambient, while oxygen is transported in the opposite direction, i.e. from the ambient to where it is

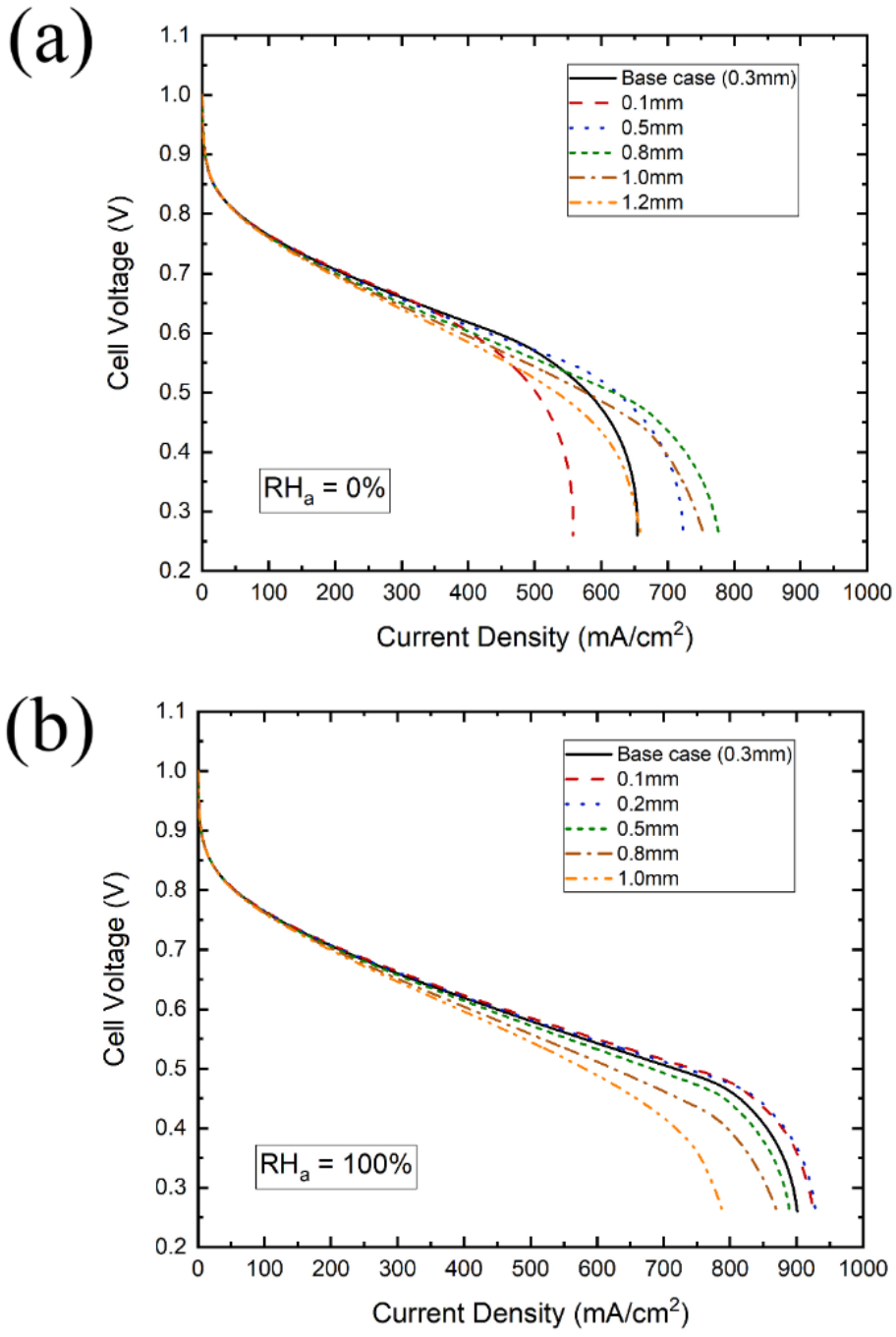

Figure 3-11 Effect of the GDL thickness on the cell performance at two anodic (hydrogen) relative humidity: (a) 0% and (b) 100%.

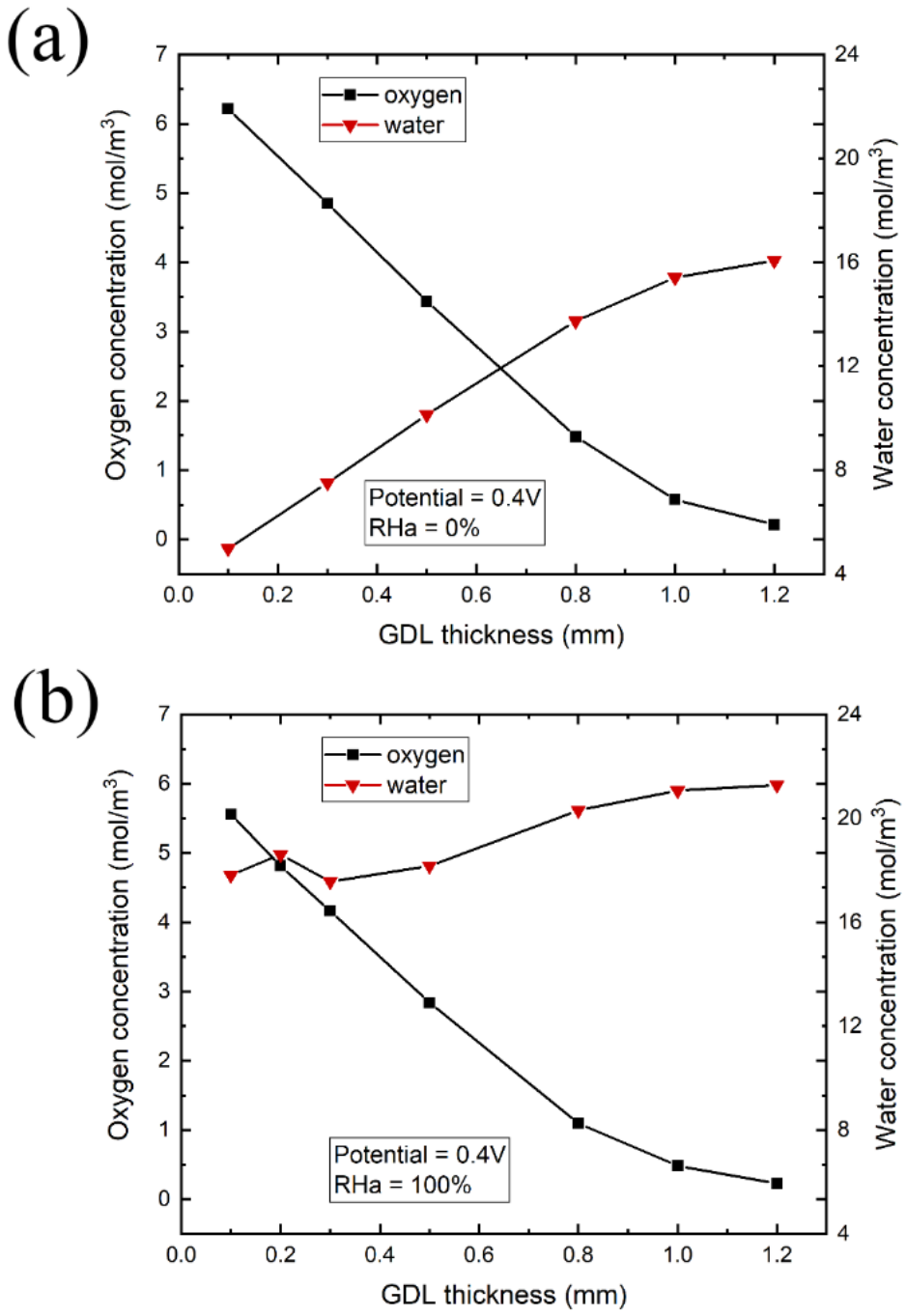

Figure 3-12 Effect of the GDL thickness on the oxygen and water vapour as the cathode catalyst layer at two anode (hydrogen) relative humidity: (a) 0% and (b) 100%.

consumed at the cathode catalyst layer. When a thicker GDL is chosen, it becomes more difficult for water to be transported from the cathode catalyst layer to the ambient region and for oxygen to be transported from the ambient to the catalyst layer. For this reason, an optimal thickness is favoured to ensure the supply of sufficient oxygen for the oxygen reduction reaction and to supply sufficient water vapour to appropriately humidify the membrane. However for the fully humidified condition (Fig. 3-12(b)), water vapour is also transported from the anode side to the cathode catalyst layer. Thus a thinner GDL at the anode side enhances the diffusion of water vapour through the GDL, thus causing the water concentration to reach a relatively high value, and then it follows the same trend as the dry condition. For this case, a thinner GDL is appropriate for the cell operation at the high humidified conditions since there is a relatively high concentration of water and oxygen at the cathode catalyst layer.

Based on the above findings, it could be stated that there exists an optimal thickness for the cathode GDL that ensures sufficient supply of both oxygen and water vapour. On the other hand, a relatively thin GDL can improve the transfer of water vapour to the cathode and this improvement becomes more profound as hydrogen relative humidity increases.

It should be noted that a relatively thick GDL can cause water flooding; Fig. 3-13 shows that relatively thick GDLs (i.e. 0.8 and 1.2 mm) causes water activity to be more than unity for most of the anodic relative humidity values, thus leading to possible water flooding.

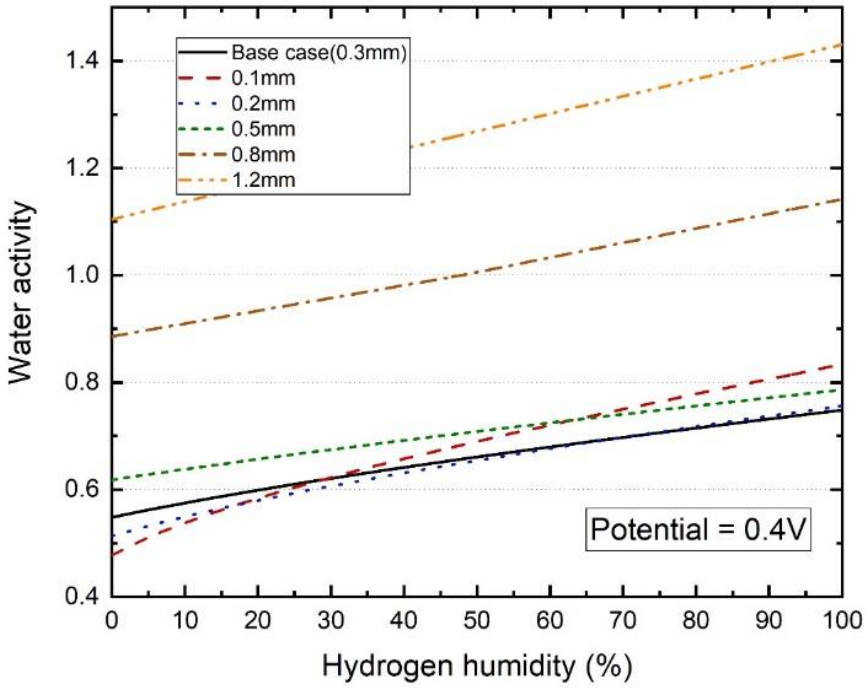

Figure 3-13 Effect of the GDL thickness on the water activity at the cathode catalyst layer.

3.4 Conclusions

In this chapter, a mathematical zero-dimensional model has been developed for air-breathing PEM fuel cells. The main purpose of this study is to examine the effects of hydrogen humidity on the performance of AB-PEMFCs. The main conclusions are as follows:

- The heat transfer coefficient dictates the performance limiting mode of the air-breathing PEM fuel cell: dry-out of the membrane with relatively low heat transfer coefficient and water flooding with relatively high heat transfer coefficient.

- The performance of the fuel cell significantly improves with increasing anodic (hydrogen) relative humidity and this is due to the increase in the water concentration at the cathode catalyst layer at high current densities. For example, the limiting current density increases by more than 40% at an ambient temperature of 30 °C when increasing the anodic relative humidity from 0 to 100%. This improvement is marginally influenced by the humidity condition at the cathode side. Further, the increase in the anodic relative humidity does not cause water flooding at high current densities.
- In order to maintain high concentrations of both oxygen and water vapour at the cathode catalyst layer, there is an optimal thickness for the cathode GDL. However, for anode GDLs, the thinner GDLs are preferred to enhance the diffusion of water vapour at the anode and consequently increase the water concentration at the cathode, and this improvement is more significant with the hydrogen relative humidity increases.

Chapter 4: Numerical investigations on the local performance of flow channels in AB-PEMFCs

Summary

A 3D VOF model for an anode channel in an AB-PEMFC has been built in this chapter. The effects of the initial position of the water droplet, its size as well as the wettability of the GDL are investigated under different operating conditions. It is found that the initial position of the relatively small water droplet in the channel has almost no effect on the pressure drop and the time taken for the liquid water to move out from the channel; however, such effects become more profound as the size of the water droplet increases. Also, when the droplet is placed at the side wall of the channel, then it develops into pockets of water that are mainly located at the upper corners of the channel, thus causing a smaller pressure drop compared to the cases in which the water droplet is placed either on the surface of the GDL or on the top wall of the channel. Furthermore, the hydrogen velocity is found to have a negligible effect on the dynamics of liquid water; however, the pressure drop and removal time are significantly influenced by the hydrogen velocity. Moreover, as the size of the water droplet increases, the pressure drop increases and the time required for the liquid water to move out of the channel decreases. Finally, the pressure drop in the channel decreases and the removal time of the liquid water increases as the contact angle of the GDL decreases.

4.1 Introduction

Most VOF studies in PEMFCs have focused on the flooding in the cathode channels which is commonly-encountered in PEMFCs as water is produced at the cathode. However there is no cathode gas channel in AB-PEMFCs since the cathode is open to the ambient air, and some visualization experiments have showed that, under some certain operating conditions, e.g. low current densities and high relative humidity, flooding can occur in the anode gas channel [108–110]. In the cathode compartment, liquid water emerges from the GDL pores. While in the anode channel, liquid water can be either (i) the produced within the anode channel through condensation of water vapour at the walls of the channel where the temperature is lower than that of the GDL surface, or (ii) the transferred from the cathode side through the membrane by back diffusion and pressure difference [111]. Ge and Wang [62] were the first to present visualization results of the flooding in the anode channel. Their results showed that water was prone to condense on the channel walls rather than inside the hydrophobic GDL. In addition, they found that hydrophilic anode GDLs could alleviate anode channel flooding. Lee and Bae [112] compared water flooding at both the anode and the cathode by employing a transparent fuel cell. They found that flooding at the anode was more significant than that at the cathode and this was attributed to the relatively high rate of back diffusion and low flow rate of hydrogen. Ferreira et al. [113] numerically investigated the two-phase flow in the anode channel by adopting the VOF model. They placed a water droplet on the top wall of the channel at the start of the simulations and subsequently studied the effects of the hydrogen velocity, operating

temperature and the channel walls wettability on the droplet. Hou et al. [114] built a VOF model for alkaline membrane fuel cells and investigated the sensitivity of liquid water removal to the geometry of the flow channels at both the anode and cathode sides. However, in their study, a single droplet was placed at the surface of the GDL at the anode side where water is generated in this type of fuel cell.

In previous studies, the effects of the initial position of the water droplet and the GDL wettability at the anode have not been investigated. Unlike the cathode channel, the initial position of the water droplets in the anode channel is more unpredictable. Therefore, a 3D VOF model is built in this study to investigate the sensitivity of the dynamics of the liquid water droplet to the initial position in the anode flow channel. Also, the effects of the size of the droplet and the hydrogen velocity are investigated. Further, the effects of the anode GDL wettability on the dynamics of liquid water droplet, average pressure drop and water removal time are investigated. Such investigations are important as they provide insights on how one could design fuel cell components which mitigate water flooding at the anode of the fuel cell.

4.2 Numerical model

Fig. 4-1 shows a schematic of the 3D computational domain considered in this study. It contains a straight gas channel with a 1 mm × 0.5 mm rectangular cross section and 5 mm length. The cross sectional area, namely 1 mm × 0.5 mm, of the channel was chosen because it is commonly used in commercial products. Further, the channel length of 5 mm is chosen since it is found to be long enough for the multi-

phase flow to be fully developed and to cover all the possible dynamics of the liquid water such as detachment. To this end, modelling the entire channel is unnecessary, especially when bearing in mind that it requires much larger computational time. The bottom surface represents the surface of the GDL while the other sides represent the walls of the flow channel.

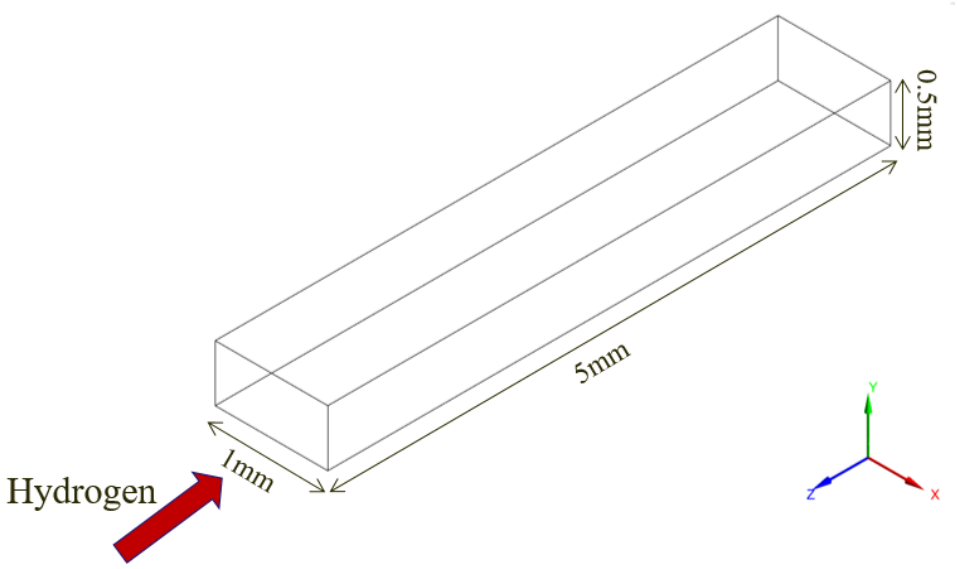

Figure 4-1 A schematic diagram of the modelled anode channel.

The boundary conditions used for the model are the velocity-inlet for the inlet of the channel and pressure-outlet for the outlet of the channel. Apart from the boundary conditions assigned at the inlet and the outlet of the channel, other surfaces are treated as a "wall" so that different values of the contact angle can be set for each surface. The consumption of hydrogen due to the anodic electrochemical reaction is neglected in the model. This simplification is widely

used when modelling two-phase flow in fuel cell channels as this would not affect the dynamics of the liquid water in the channel which is the focus of such studies [68,69,115]. A 25 cm^2 PEM fuel cell operating at 0.5 A cm^{-2}, 80 °C and hydrogen stoichiometric ratio of 1.2 are chosen for the simulation of the base case. These were found to be conditions at which anode flooding occurs [112]. Based on the above conditions, the velocity of the inlet gas, which is a mixture of water vapour and hydrogen, is calculated to be 2 m s^{-1}, and all the physical parameters considered in the model are listed in Table 4-1. In this study, fully humidified hydrogen is chosen for all simulations as this will most likely cause anode flooding.

The simulations in this study are run using ANSYS FLUENT 18.2. The pressure-based solver is employed in the model. It should be noted that the Reynolds and Bond numbers were found to be small for all simulated cases: less than 10^3 and 0.1, respectively. Therefore, the laminar viscous model has been selected and the gravity effect has been neglected.

Table 4-1 Values of the parameters applied in the VOF model. Unless otherwise stated, the values of the parameters are taken from [113].

Parameter	**Value**
Temperature	353 K
Inlet velocity	2 m s^{-1}
Ambient pressure	101,325 Pa
Outlet pressure	0 Pa (gauge)
Gas density	6.877×10^{-2} kg m^{-3}
Liquid water density	971.8 kg m^{-3}
Gas viscosity	9.995×10^{-6} Pa s
Liquid water viscosity	3.544×10^{-8} Pa s
Surface tension	6.267×10^{-2} N m^{-1}

A computational domain consisting of 96,526 cells is employed in this study. Grid independency is tested by decreasing and increasing this number by 20%; the changes in the velocity profile and pressure drop were found to be negligible, thus indicating grid independency. The time step is set to be 10-6 s and therefore the global Courant number is less than 2. Different time steps, i.e. between 10-7 s and 10-5 s, have been also tested in the model, and the time step of 10-6 s was found to be a suitable trade-off between the accuracy and computational time.

Table 4-2 The computation cases investigated in the VOF model.

Case	Contact angle (°)		Droplet			Operation condition
	GDL	Channel walls	Diameter (mm)	Location (mm)	Distance (mm)	Hydrogen velocity (m/s)
1	140	45	0.5	Top wall	1	2
2	140	45	0.5	Side wall	1	2
3	140	45	0.5	GDL	1	2
4	140	45	0.5	Top wall	1	1
5	140	45	0.5	Side wall	1	1
6	140	45	0.5	GDL	1	1
7	140	45	0.5	Top wall	1	3
8	140	45	0.5	Side wall	1	3
9	140	45	0.5	GDL	1	3
10	140	45	0.5	Top wall	3	2
11	140	45	0.5	Side wall	3	2
12	140	45	0.5	GDL	3	2
13	140	45	1	Top wall	1	2
14	140	45	1	GDL	1	2
15	10	45	1	Top wall	1	2
16	30	45	1	Top wall	1	2
17	45	45	1	Top wall	1	2
18	60	45	1	Top wall	1	2
19	90	45	1	Top wall	1	2
20	120	45	1	Top wall	1	2
21	170	45	1	Top wall	1	2

4.3 Results and discussion

In this study, the effects of the initial position of the water droplet, its size and the wettability of the GDL surface are investigated. Table 4-2 shows all the cases investigated, detailing the contact angles for the GDL and walls of the channel, the size of the water droplet, the hydrogen velocity, the position of the water droplet and its distance from the inlet. Case 1 is the baseline case where a hydrophobic GDL and a hydrophilic channel are chosen. Although different sizes were considered for the droplet and the channel, the results for Cases 1,4,7 and 13 were shown to be in good agreement with those of Ferreira et al. [113].

4.3.1 Droplet initial position

The same size droplets are placed on the top wall, side wall and GDL surface in order to investigate the sensitivity of the liquid water dynamics to the initial position of the water droplet. The initial position of the water droplet is selected to signify how water flooding is initiated. For example, the case where the droplet is placed on the GDL surface signifies that water flooding is attributed to the water transfer from the cathode to the anode by back diffusion and pressure difference. Fig. 4-2 shows the water dynamics for the Cases 1-3. It should be noted that the droplet in all the cases is assumed to be a hemisphere. For the baseline case, i.e. Case 1, where the water droplet is placed on the top wall of the channel, it can be observed that the droplet first spreads, thus increasing the contact area, and then it moves to the outlet along the top wall. As will be shown in the next section, the spread of the water droplet increases as the droplet size increases. For Case 2, where the droplet is placed on the side wall, the droplet first spreads to both the top wall and the GDL

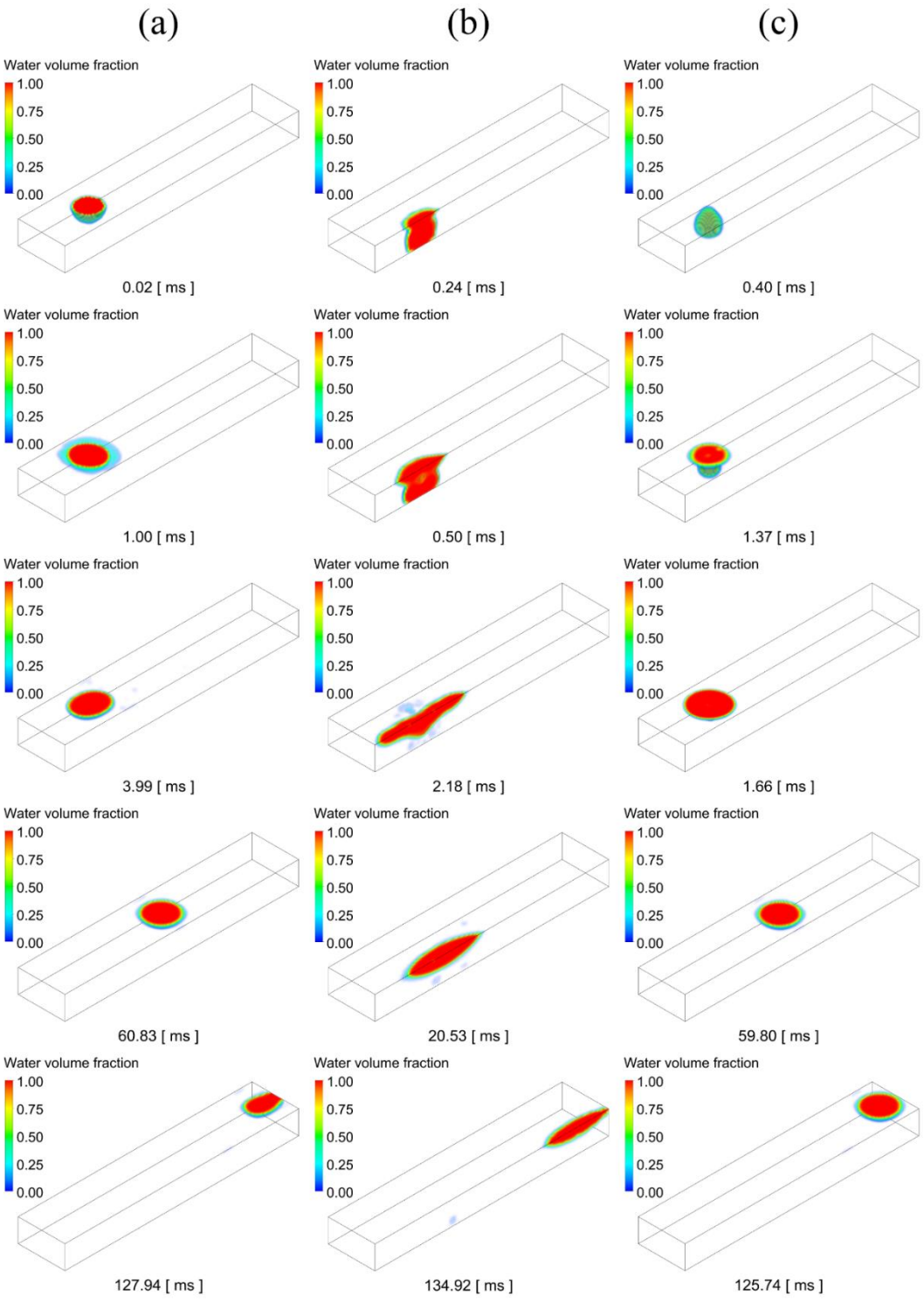

Figure 4-2 The dynamics of liquid water droplet for different initial positions: (a) top wall, (b) side wall and (c) GDL surface. The distance from the inlet is 1 mm.

surface. Since the GDL surface is hydrophobic, liquid water moves away from the GDL and moves to the upper corner of the channel. When all the water has reached the upper corner, the water forms a narrow and long film, and moves to the outlet along the corner. For a droplet placed on the GDL surface, the droplet first detaches from the GDL surface because of the hydrophobic nature of that surface. The droplet then reaches the top wall and flattens as it moves towards the outlet. It can be seen that the difference in the water dynamics between Cases 1 and 3 is small. However in Case 3, the water droplet collides with the top wall; such a collision is, as will be shown in the next section, more profound as the size of water droplet increases.

In order to obtain some quantitative differences between the above cases, Fig. 4-3(a) presents the average volume fraction of the water and the pressure drop for Cases 1-3 as a function of time. When correlated with time, the average volume fraction of water gives insight into how quickly the liquid water is removed from the channel. As shown in Fig. 4-3(a), the shortest time to move out of the channel (~130 ms) is taken by the droplet that is initially placed at the top wall of the channel, i.e. Case 1. The droplet on the GDL surface takes a longer time to reach the outlet since it first experiences a detachment from the GDL surface and a collision with the top wall of the channel before forming a film. On the other hand, in these three cases the longest time to move out of the channel is taken by the droplet that is initially placed at the side wall of the channel and this is mainly because of the elongated shape of the forming film. Fig. 4-3(b) shows the pressure drop for these three cases. The difference in the pressure drop between the case where the droplet

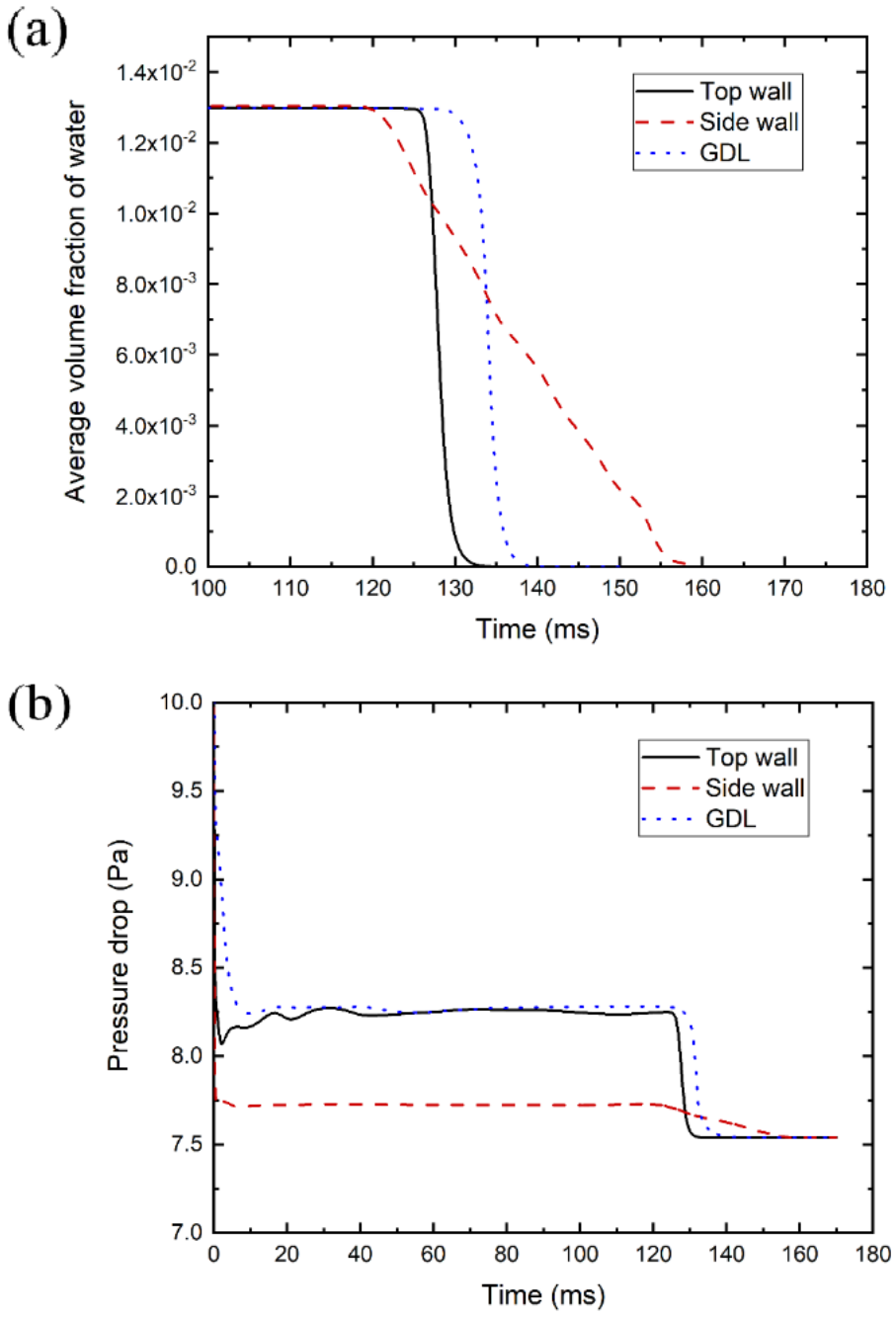

Figure 4-3 The average volume fraction of the water and (b) the pressure drop in the channel as functions of time.

is placed on the top wall and the case where the water droplet is placed on the GDL surface is small because the dynamics of the liquid water in both cases is similar. However, in Case 2, where the water droplet is placed at the side wall of the channel, a smaller pressure drop occurs since the forming water film occupies less cross-section area of the channel.

In addition to Fig. 4-3, Fig. 4-4 shows the cross-section of the channel at the moment when the water film is fully developed and the fraction of liquid water is a maximum. The fractions of liquid water occupying the cross-section is almost the same for Cases 1 and 3, and this explains why the pressure drop is more or less the same for these two cases (see Fig. 4-3(b)). On the other hand, the fraction of liquid water occupying the cross-section is the lowest for Case 2 and this is in agreement with lowest pressure drop occurring in this case.

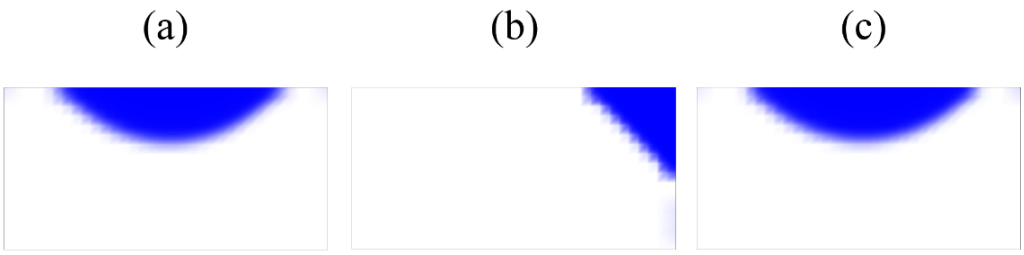

Figure 4-4 The cross-section for different initial positions: (a) top wall, (b) side wall and (c) GDL surface.

The effects of the distance of the droplet from the inlet on the dynamics of the liquid water is also investigated by changing it from 1 mm to 3 mm (Cases 10-12). Fig. 4-5 shows that the dynamics of the liquid water droplets for Cases 10-12 are similar

to those of Cases 1-3, thus indicating the negligible effects of the investigated variable, i.e. the distance from the inlet, on the dynamics of liquid water droplets.

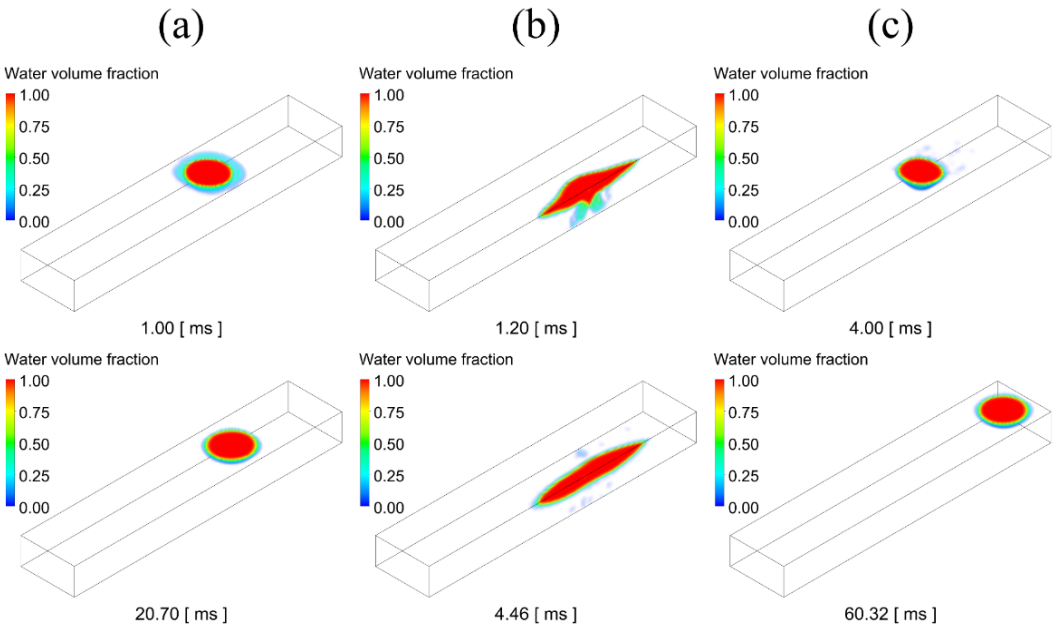

Figure 4-5 The water dynamics of the liquid water droplet for different initial positions on: (a) top wall, (b) side wall and (c) GDL surface. The distance of the droplet from the inlet is 3 mm.

4.3.2 Operation condition

The velocity of hydrogen has been changed in Cases 4-8 in order to represent different operation conditions; the operating current density dictates the velocity of the reactant gas. It was found that the dynamics of the water was only slightly influenced by the velocity of the hydrogen — the dynamics of the water in these cases was similar to those presented in Fig. 4-2 and therefore these results have not been presented. However, the hydrogen velocity has a significant effect on the water removal time and pressure drop in the channel; see Fig. 4-6 which shows the

removal time for the water and the average pressure drop in the channel as functions of the hydrogen velocity for the Cases 1-9.

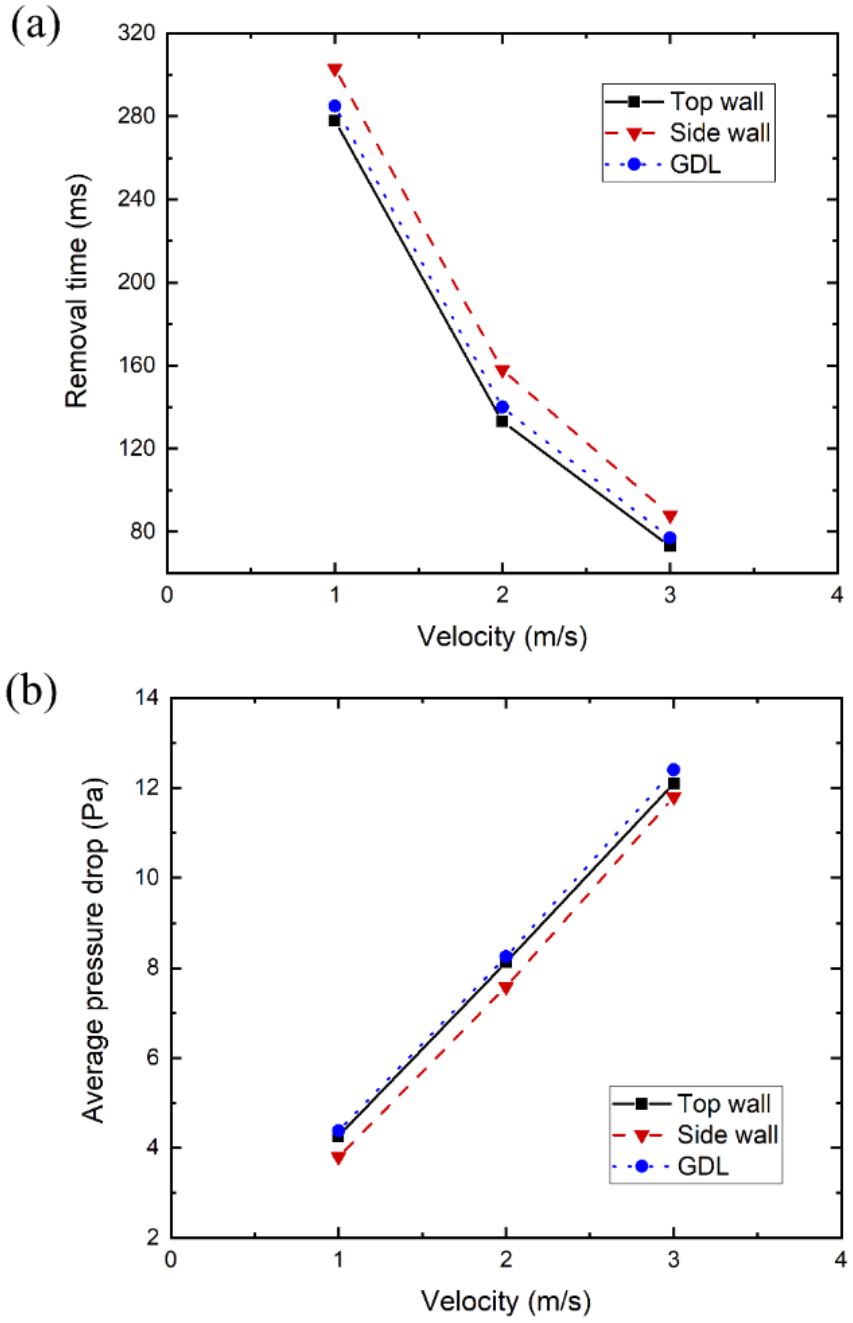

Figure 4-6 (a) The removal time of water and (b) the average pressure drop in the channel as functions of the hydrogen velocity.

The removal time decreases with increasing the hydrogen velocity. One can also observe that the average pressure drop increases as the velocity increases. It should be noted that, under any operating condition, the droplet placed on the side wall causes a smaller pressure drop compared to the cases in which the water droplet is placed either on the surface of the GDL or on the top wall of the channel; however, it requires a longer time to move out of the channel.

4.3.3 Droplet size

At the anode flow channel, water vapour may condense at different locations in the flow channel, thus forming water droplets. These droplets are likely to coalesce and form larger droplets. Due to this, different sizes of the droplet can be employed to represent different levels of severity of water flooding. Therefore, it is of interest to investigate the sensitivity of the dynamics of the liquid water in the anode flow channel to the size of the water droplet. It should be noted that the dynamics of the large droplet placed at the side wall was found to be more or less the same as that of the small droplet, see Fig. 4-2(b), and therefore it has not been presented in Fig. 4-7. In the cases discussed in the previous section, 0.5 mm diameter droplets are employed; however, larger droplets (i.e. 1 mm diameter) are used in Cases 13 and 14 and placed on the top wall and GDL surface, respectively.

Fig. 4-7 shows the water dynamics for the 1 mm water droplets. Fig. 4-7(a) shows the water droplet placed at the top wall of the channel, due to its relatively large size and the hydrophilicity of the surfaces of the channel, spreads to the side walls of the channel before moving towards the outlet. For the droplet placed on the GDL surface, see Fig. 4-7(b), the droplet, due to the hydrophobicity of the GDL, moves

towards and collides with the top wall of the channel, thus causing the droplet to flatten and disperse over a large area on the top and side walls of the channels.

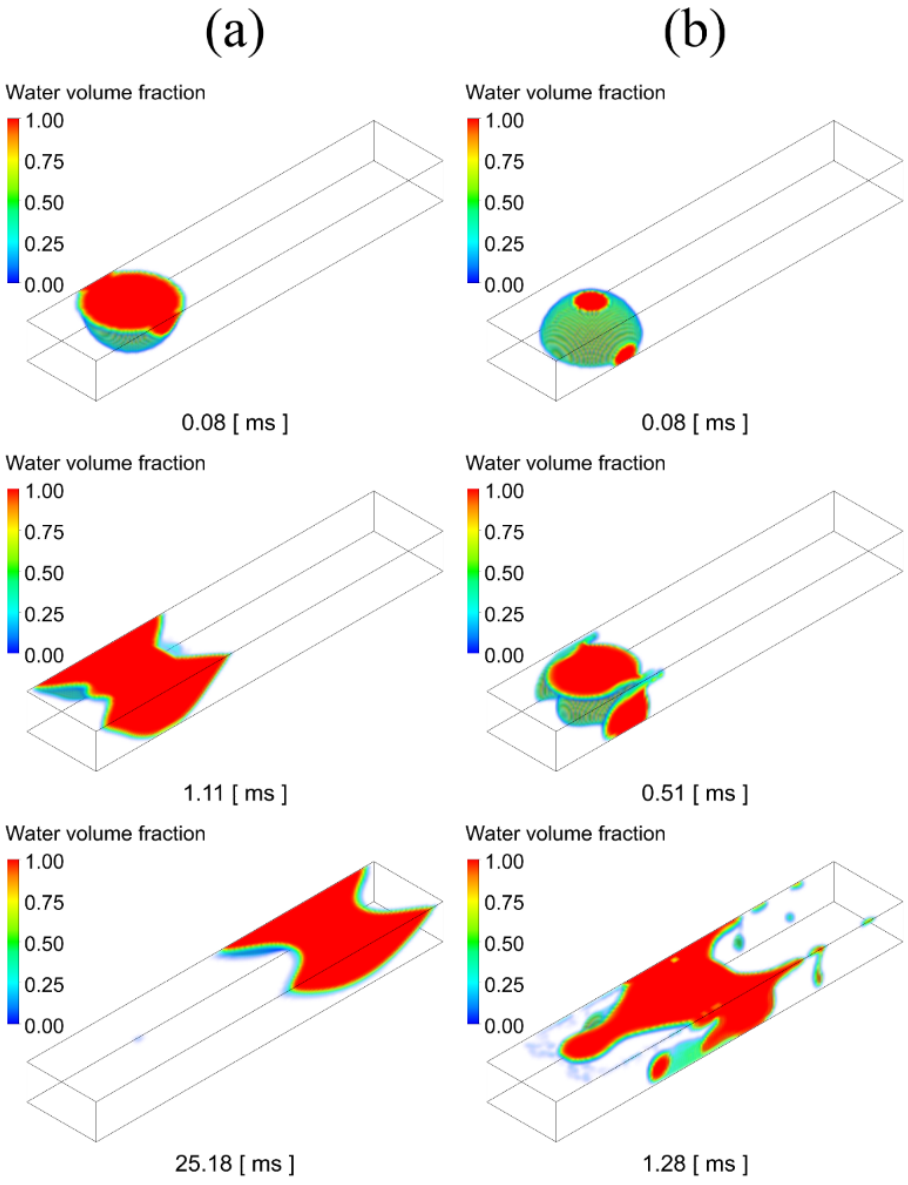

Figure 4-7 The water dynamics of 1 mm water droplets placed on: (a) top wall and (b) GDL surface.

Fig. 4-8(b) shows the pressure drop for the Cases 13 and 14. It can be seen that the pressure drop for the case in which the water droplet is initially placed on the GDL surface, i.e. Case 14, is smaller than that of the case in which the water droplet is

initially placed on the top wall (Case 13). This could be attributed to the observation that the extent of the dispersion of the liquid water in Case 14 is higher than that of Case 13.

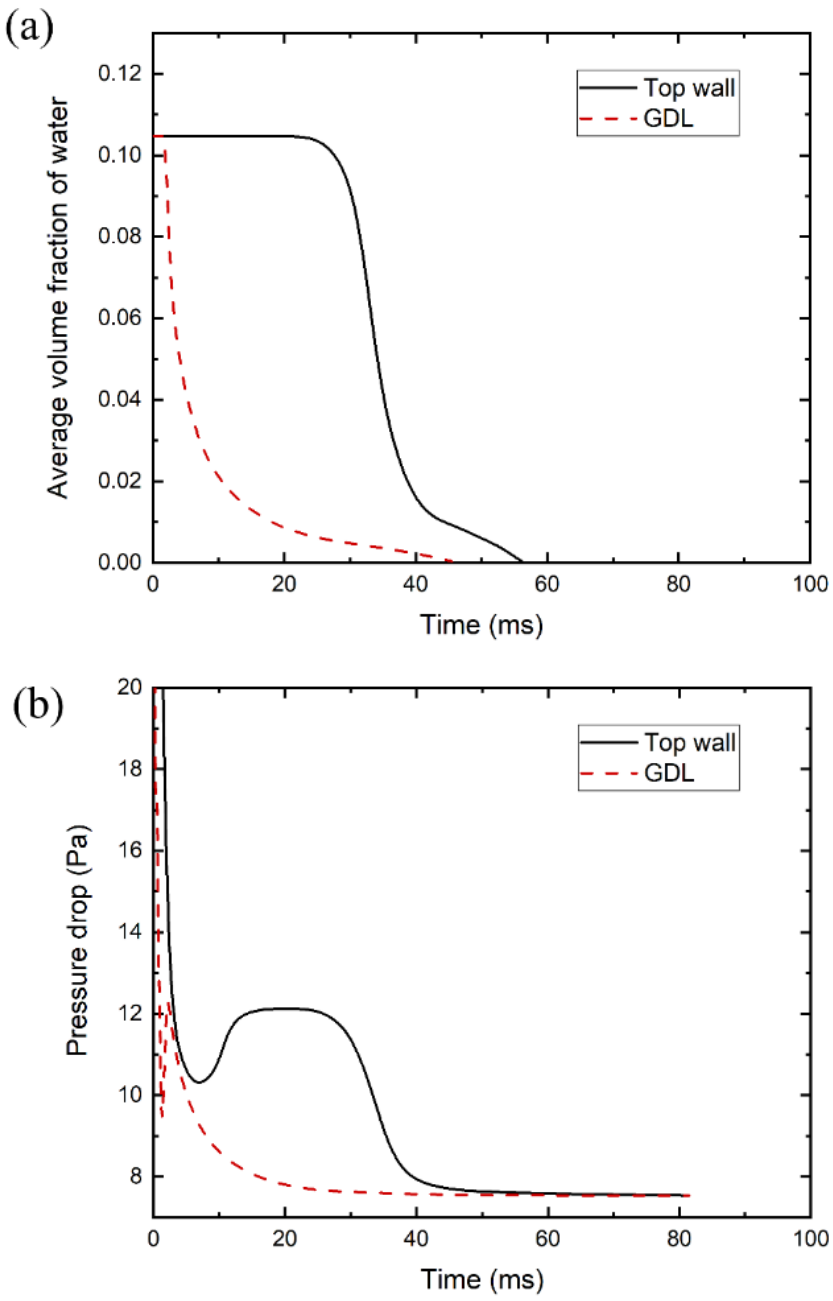

Figure 4-8 (a) The average volume fraction of water and (b) the pressure drop in the gas channel as functions of time.

The larger droplet placed on the top wall of the channel causes a larger pressure drop compared to the corresponding smaller droplet before being removed from the channel; see Fig. 4-3(b) and Fig. 4-8(b). Fig. 4-8(a) displays the average volume fraction of the water as a function of time for the Cases 13 and 14. Compared with the results shown in Fig. 4-3(a), it can be seen that larger droplets require less time to move out from the channel. In order to explain this, velocity vectors of the gas over the surface of the small droplet in Case 1 and over the surface of the larger droplet in Case 13 are generated.

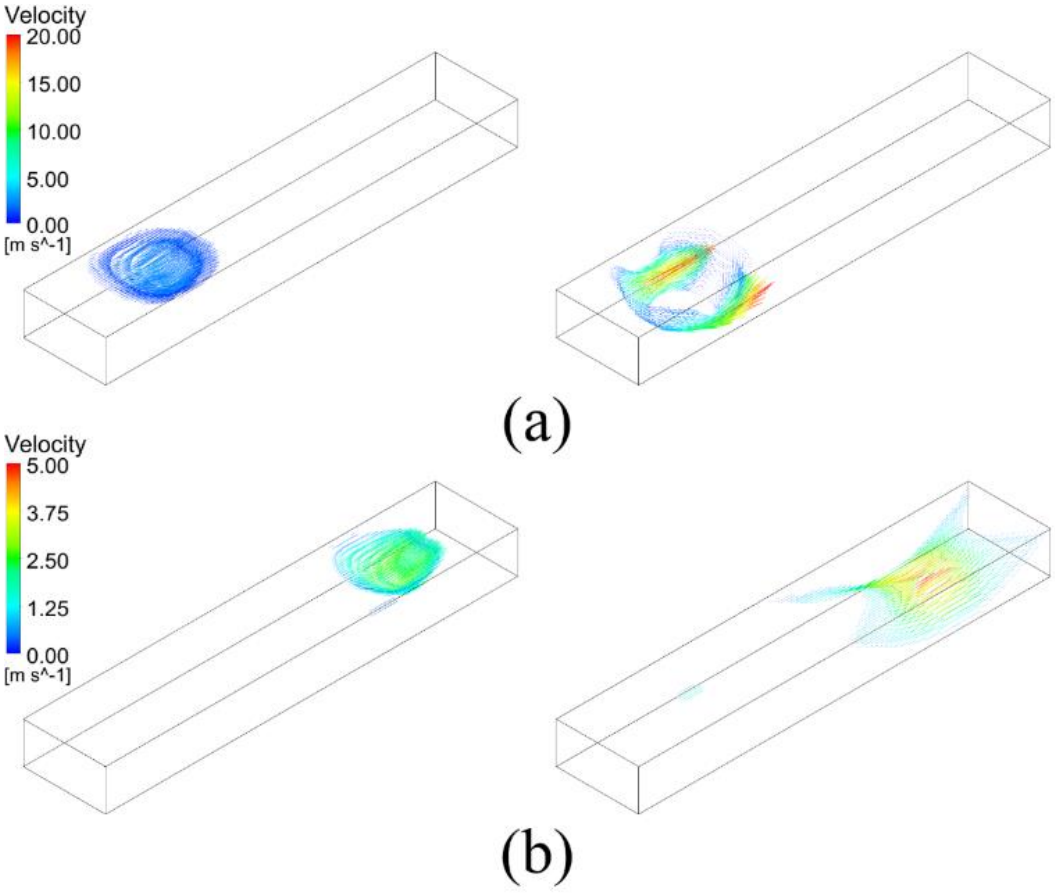

Figure 4-9 The velocity profile over the surface of the small droplet (left) and large droplet (right) (a) at the beginning of the simulation and (b) towards the end of the simulation.

It is clear that the gas velocity values over the surface of the larger droplet are significantly larger than those over the surface of the smaller droplet, see Fig. 4-9. This is due to the fact that the larger droplet occupies a larger cross-section of the channel, thus resulting in a higher velocity and subsequently a faster removal from the channel.

4.3.4 GDL wettability

Cases 15 – 21 are investigated in order to study the effect of the GDL wettability on the dynamics of the liquid water. In these cases, a single droplet with a diameter 1 mm is placed on the top wall. The diameter of 1 mm was chosen since the 0.5 mm water droplet placed on the top wall was shown not to contact the GDL surface, see Fig. 4-2, thus rendering the investigation of the effects of the GDL wettability not possible. The low contact angles in Cases 15-18 represent hydrophilic GDLs which have been recently employed in practical fuel cells as shown in [62].

Fig. 4-10 shows the water dynamics for three selected cases, namely Cases 15, 16 and 21. The dynamics of the other cases, i.e. Cases 17-20, are not presented since the dynamics of the liquid water in these cases were shown to be similar to the above-investigated cases. However their results, along with those of Cases 15, 16 and 21, were used to generate the Fig. 4-11.

For the case in which the contact angle of the GDL is 10°, the droplet spreads over the GDL surface and, in particular, near the lower corners of the channel and this is, compared to those of the top and sides walls of the channel, clearly due to the super-hydrophilicity of the GDL surface. It should be noted that the strong adhesion

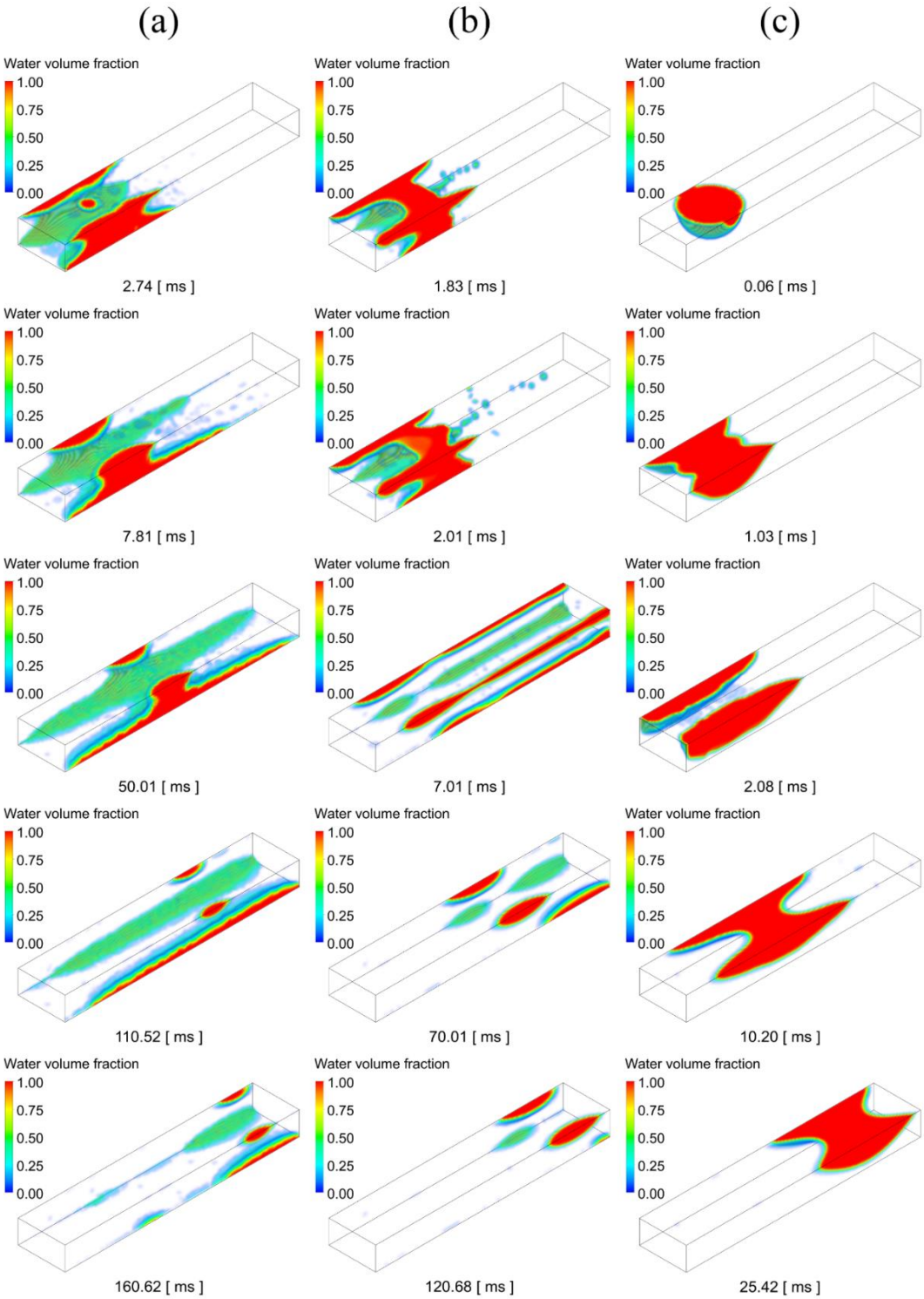

Figure 4-10 The water dynamics with different GDL contact angles: (a) 10°, (b) 30° and (c) 170°.

force between the liquid water and the surface of the GDL in the above case results in creating elongated pockets of liquid water. In Case 16, as the difference in the contact angles between the walls of the channel (45°) and the GDL (30°) is relatively small, the initial liquid water droplet splits into four portions that are mainly positioned at the four corners of the channel. For the case in which the contact angle of the GDL is 170°, the dynamics of the liquid water is similar to that of the case in which the contact angle of the GDL is 140°, i.e. Fig. 4-7(a).

Fig. 4-11(a) shows the time taken for the liquid water to move out from the flow channel as a function of the GDL contact angle. The liquid water requires more time to move out from the channel as the contact angle decreases and this is due to the relatively strong adhesion force between the liquid water and the surface of the GDL. Fig. 4-11(b) shows the pressure drop averaged over the time taken for the liquid water to move out from the channel. Overall, it can be observed that the pressure drop decreases as the contact angle decreases and this is due to the increasing extent of the spreading of the liquid water over the surfaces of the channel and the GDL with decreasing GDL contact angle; this is in agreement with the previous experimental observations [112]. However the super-hydrophilic GDL, where the contact angle is 10°, increases the pressure drop in the channel. Bearing in mind that the pressure is averaged over the removal time, and this is attributed to the relatively long time taken by the liquid water to move out of the channel for the above case, i.e. the case in which the contact of the GDL is 10°. In commercial fuel cell products, with a more hydrophilic GDL surface, liquid water is more likely to accumulate and form big droplets due to the longer removal time. Although a single

droplet in this kind of channel may cause a relatively low pressure droplet (Fig. 4-11(b)), the big accumulated droplet can lead to an extensive pressure drop and even cause a blockage. So the trade-off between the pressure drop and the removal time should be considered when designing practical products.

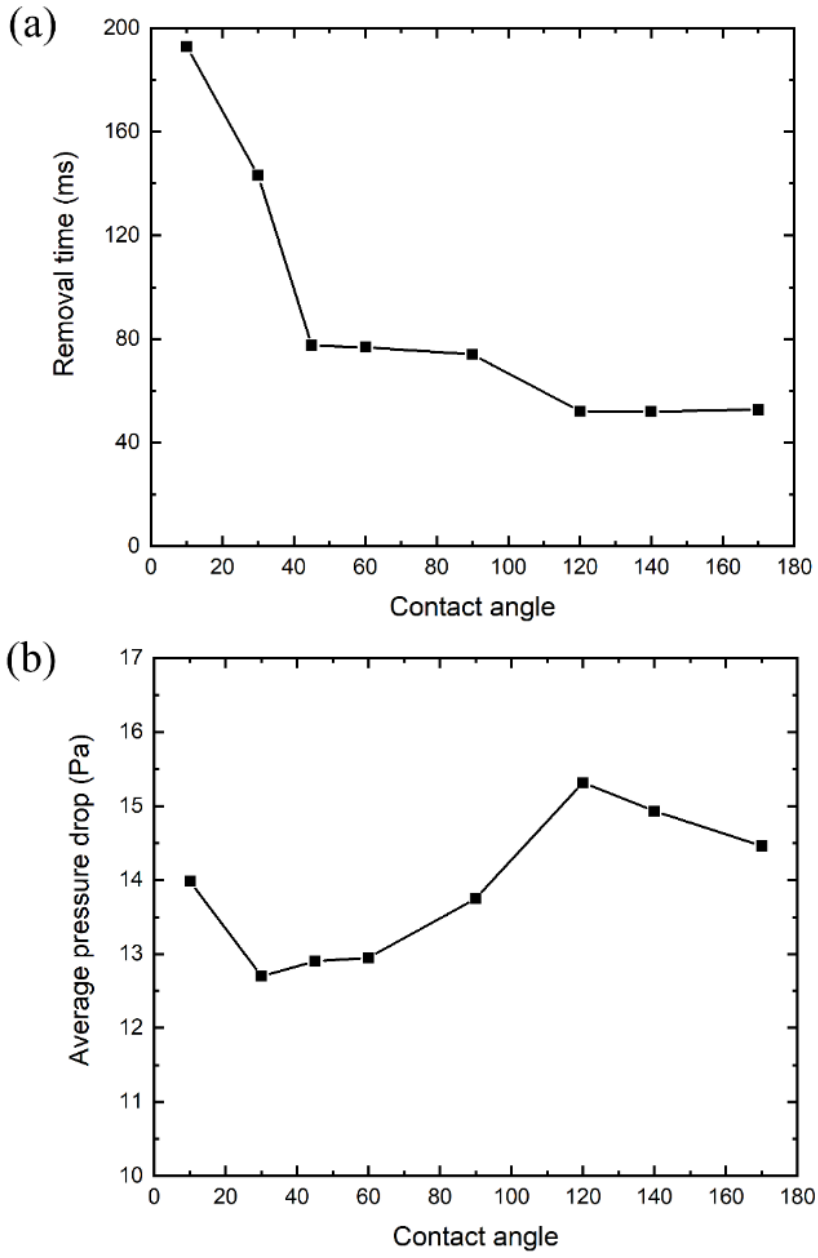

Figure 4-11 (a) The removal time for the water and (b) the average pressure drop in the channel as functions of the GDL contact angle.

4.4 Conclusions

In this chapter, a 3D VOF model has been developed for anode channels in AB-PEMFCs. The main purpose of this study is to examine the effects of the initial position of a water droplet, its size and the GDL wettability on the dynamics of the liquid water as it moves out of the flow channel. The findings of the study provide insightful information when designing fuel cells which are vulnerable to water flooding at their anode. The main conclusions are as follows:

- The time taken for the liquid water droplet to move out from the channel and the pressure drop caused are almost insensitive to the initial position of the water droplet in the flow channel.
- The water droplet, initially placed at the surface of a typical hydrophobic GDL, detaches from the GDL surface and collides with the top wall of the channel, thus causing relatively more dispersion of the liquid water. This phenomena becomes more profound as the size of the water droplet increases.
- The droplet that is initially placed on the side wall of the channel develops into elongated pockets of water that is mainly located near the upper corners of the channel. This leads to a smaller pressure drop but more time for the water to move out of the channel compared to the cases in which the water droplet is initially placed on the top wall of the channel or the surface of the GDL.
- The distance between the initial position of the water droplet and the inlet of the channel has almost a negligible effect on the dynamics of liquid water.

- The dynamics of the liquid water is almost independent of the hydrogen velocity; however, the latter has a significant effect on the removal time and the pressure drop in the channel.
- As the water droplet size increases, the velocity profile over the surface of the droplet increases, thus leading to less time required for the liquid water to move out of the channel. However, the pressure drop in the channel increases with increasing droplet size.
- For relatively large droplets, the pressure drop generally decreases with decreasing contact angle of the GDL. However, due to the strong adhesion forces, the time required to clear the channel from liquid water increases with decreasing GDL contact angle.

Chapter 5: Experimental studies on GDL stacks

Summary

The thickness of GDLs is found to be important in determining the performance of AB-PEMFCs in previous modelling investigations. In order to produce the GDLs with different thicknesses, stacking of several GDL layers is an appropriate choice. In this chapter, the effect of stacking on through-plane permeability is investigated. By combining some single GDL layers, different GDL stacks are prepared and then tested in the permeability setup. In addition to stacking, the effect of contact tightness between each layer in the GDL stacks is discussed. The results show that stacking has a negligible influence on the overall through-plane permeability and a tighter contact can slightly increase the permeability of the GDL stack.

5.1 Introduction

Gas permeability is a key property of GDLs since it largely influences gas flow through GDLs. The gas permeability of a GDL can be divided into the in-plane permeability and through-plane permeability [116,117], and due to its importance in determining the convective flow in the GDLs, many studies have been conducted to investigate the permeability of different GDLs.

Ismail et al. [119] studied the effect of PTFE treatment on the through-plane permeability of the tested GDLs. It was found that there exists an optimum amount of PTFE (i.e. 5% by weight) at which the through-plane permeability of the GDL

is a maximum, meaning that a relative small amount of PTFE can improve the through-plane permeability of the GDL. Further, the same research group has conducted a series of experiments in order to study the through-plane permeability of the MPL in the GDL [77,120]. In general, the coating of the MPL layer is found to decrease the overall permeability of the GDL, and the carbon loading significantly influences the permeability of the MPL layer. In addition to experimental studies, some research groups have proposed multidimensional models to study the GDL permeability. Tamayol et al. [121] came up with an analytical model for the GDL, where the in-plane permeability of the GDL was a function of the porosity and fibre diameter. Shou et al. [122] proposed a numerical model for mass flows through GDLs based on the scaling estimate approach and the mixing law and the permeability calculated from this model was validated by experimental results. They found that the fibre arrangement and porosity are very important in determining the permeability of the GDLs. Further, some models considered the effect of MPL penetration on the gas permeability [123–125].

However, all the above studies have measured the permeability of a single GDL sample. In this research, experiments on the through-plane permeability of the GDL stacks are conducted. The stacking of GDLs may increase the mass transfer resistance and this is because of gaps presents between the GDL samples. The permeability of GDL stacks with various number of samples have been measured and compared in order to find the effect of stacking.

5.2 Experimental setup and method

5.2.1 Experimental setup

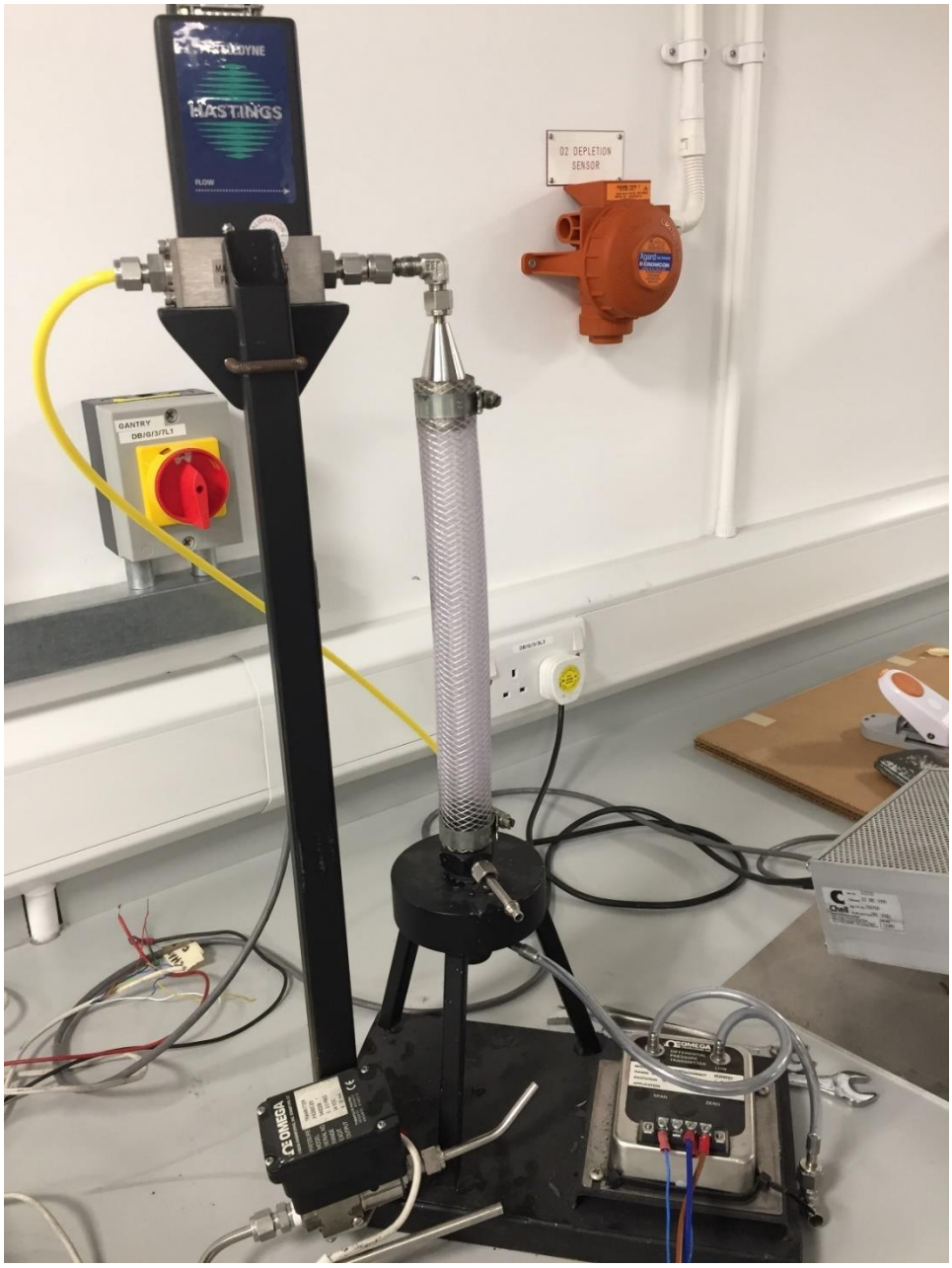

Figure 5-1 A photograph of the through-plane gas permeability setup.

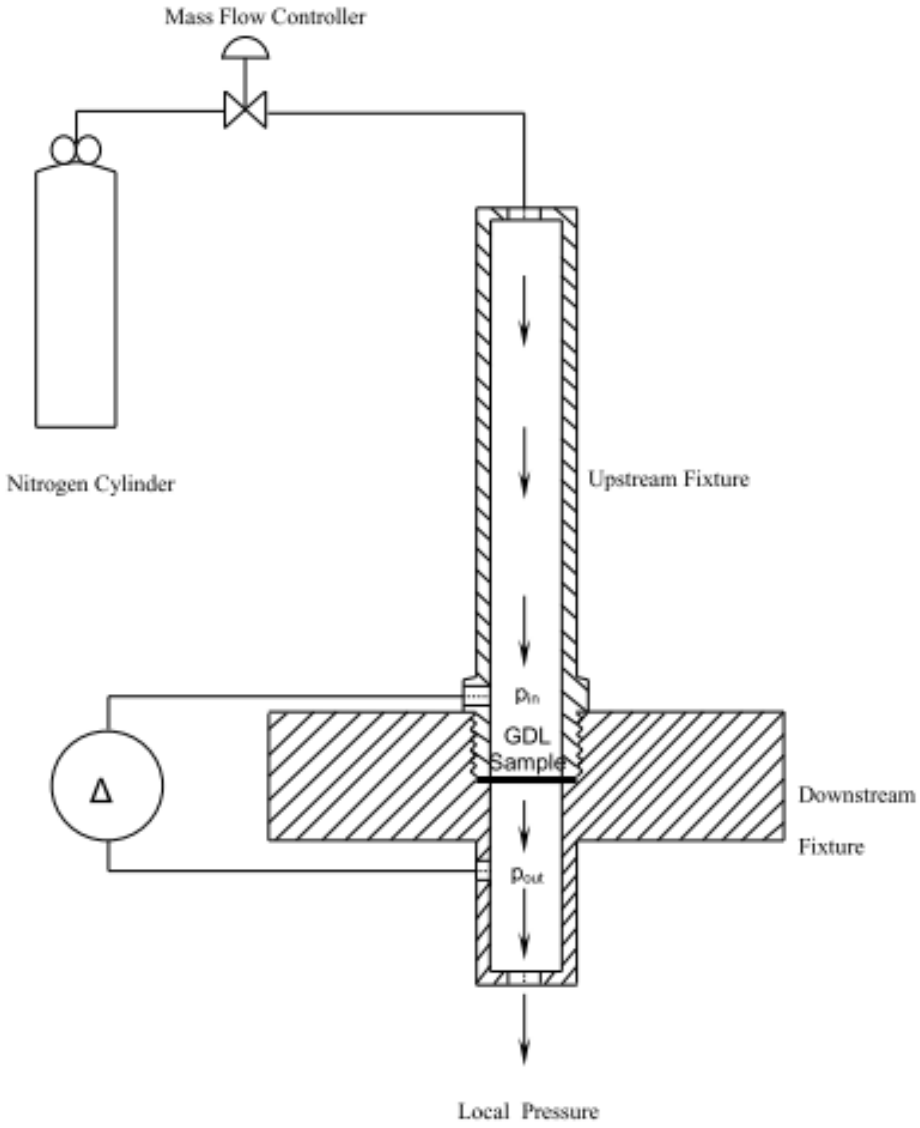

Figure 5-2 A schematic of the through-plane gas permeability setup [119].

A photograph and the schematic diagram of the experimental setup are shown in Fig. 5-1 and Fig. 5-2, respectively. The setup mainly consists of upstream and downstream fixtures. Nitrogen enters the setup through the upstream fixtures and then flow across the sample, which is fixed between these two fixtures. The flow rate is measured and controlled by a digital flow controller (Teledyne Hastings,

HFC-202) with a range of 0.0-0.1 SLPM. By employing the differential pressure sensor (Omega, PX 653) with a range of ±12.5 Pa, the pressure drop across the tested sample is measured. The stacks tested in this experiment are composed of several circular GDL samples and the diameter of a single GDL sample is 25 mm. It should be noted that the diameter of the GDL sample or stack placed between two fixtures is only 20 mm.

5.2.2 Sample preparation

The samples used in this experiment were SIGRACET 39 BA (SGL Carbon, Germany). A typical SEM image for SGL BA sample is shown in Fig. 5-3. It can be seen that BA series have some PTFE coated on the carbon fibres.

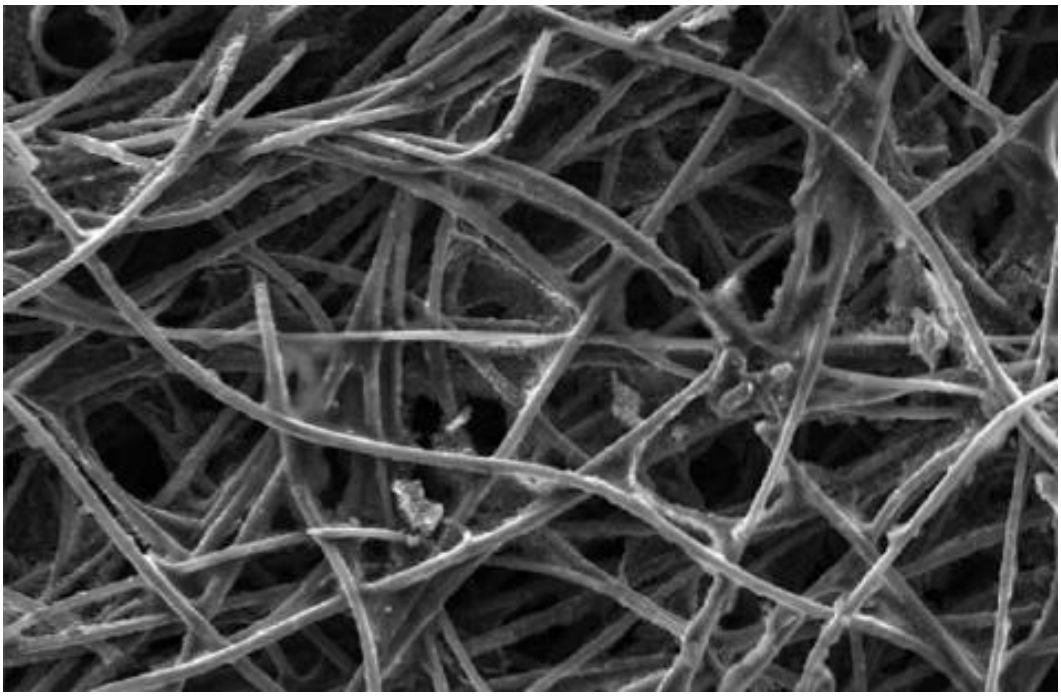

Figure 5-3 A typical SEM image for a SGL BA sample [119]**.**

Ten circular samples with 25mm diameter were cut out from a large sheet of SGL 39BA (45 x 40 cm), and the thicknesses of these samples were measured by a micrometre. The thicknesses of these samples are shown in Table 5-1. In the experiment, GDL stacks consisting of 1,2,3,4 and 5 layers have been prepared and tested for permeability. For each stack, five random combinations of the samples have been tested to calculate the average gas permeability.

Table 5-1 Thicknesses of the GDL samples used in the gas permeability experiment.

Sample	1	2	3	4	5
Thickness (mm)	0.265	0.270	0.280	0.293	0.274
Sample	6	7	8	9	10
Thickness (mm)	0.283	0.285	0.291	0.271	0.269

5.2.3 Data analysis

Because the flow rates are relatively small enough, the flow through the samples can be described by Darcy's law:

$$-\nabla p = \frac{\mu}{K} v \tag{5-1}$$

where p is the pressure, μ and v are the dynamic viscosity and velocity of the nitrogen flowing through the samples, and K is the through-plan permeability of the tested stacks. The velocity v can be calculated by:

$$v = \frac{\dot{V}}{A} \tag{5-2}$$

where $\dot{V}$ is the volumetric flow rate of the nitrogen and A is the area of the samples that are exposed to the nitrogen flow.

Based on above equations, the gas permeability can be calculated by:

$$K = \frac{\mu \delta v}{\Delta p} = \frac{\mu \delta \dot{V}}{\Delta p A} \tag{5-3}$$

where δ is the thickness of the tested GDL stack and Δp is the pressure drop across the GDL stack recorded by the differential pressure sensor.

The through-plane permeability was calculated at different flow rates and corresponding pressure drops and then the average value of permeability was obtained.

5.3 Results and discussion

5.3.1 Effect of stacking

Fig. 5-4 shows the pressure drop through the stack as a function of the nitrogen velocity. It should be noted that the velocity was sufficiently small and thus the pressure loss caused by inertia was neglected in the experiment. The permeability

was calculated by using Darcy's law, i.e. Eq. 5-3. Table 5-2 shows the calculated through-plane permeability for the tested stacks in the experiment. It is clear that, within the limits of the experimental error, the differences between the permeability of the various tested stacks are negligible. Although the 95% confidence interval is generally larger for the stacks with more samples, the average value of the permeability for the tested stacks are almost the same, which means that the stacking has a little influence on the through-plane permeability of the GDL material.

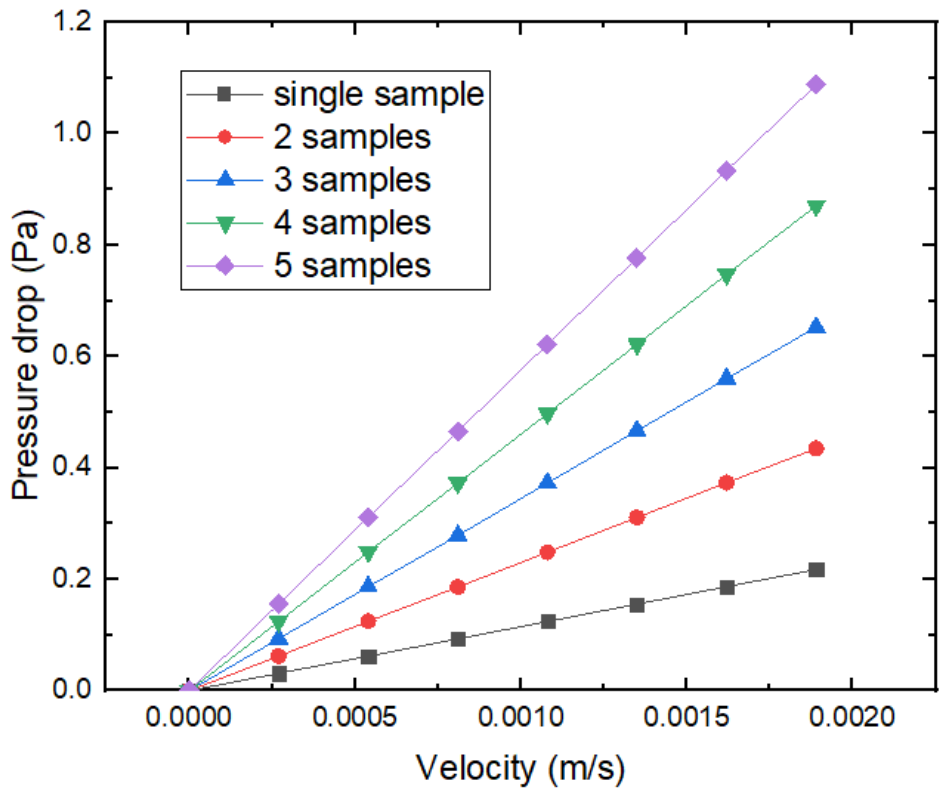

Figure 5-4 The pressure drop as a function of the nitrogen velocity for different GDL stacks.

Table 5-2 Through-plane permeability for the tested stacks

Stack type	Through-plane permeability (10^{-11} m^2)
Single layer	4.28 ± 0.15
Two layers	4.30 ± 0.21
Three layers	4.29 ± 0.24
Four layers	4.28 ± 0.22
Five layers	4.29± 0.26

5.3.2 Effect of contact tightness

The sensitivity of the through-plane permeability to the tightness on the GDL stack induced by the fixtures of the setup was investigated with the five-sample stacks. To achieve this, 2 cases were set. In the first case, the stack was placed loosely between the 2 fixtures and the corresponding permeability was calculated. In the second case, the stack was tightened between the 2 fixtures and the corresponding through-plane permeability was calculated. Fig. 5-5 shows the pressure drop across the stack as a function of the nitrogen velocity for these two cases. It can be seen that the "loose" arrangement slightly increases the pressure drop for all the nitrogen velocities. The calculated through-plane gas permeability for the GDL stack with a tight contact is 4.36×10^{-11} m^2, while the calculated permeability for the stack with a loose contact is 4.28×10^{-11} m^2. The reason behind this may be that the increased tightness may have caused some damage to the GDL stack; thus creating some cracks and subsequently resulting in increasing the gas permeability of the GDL.

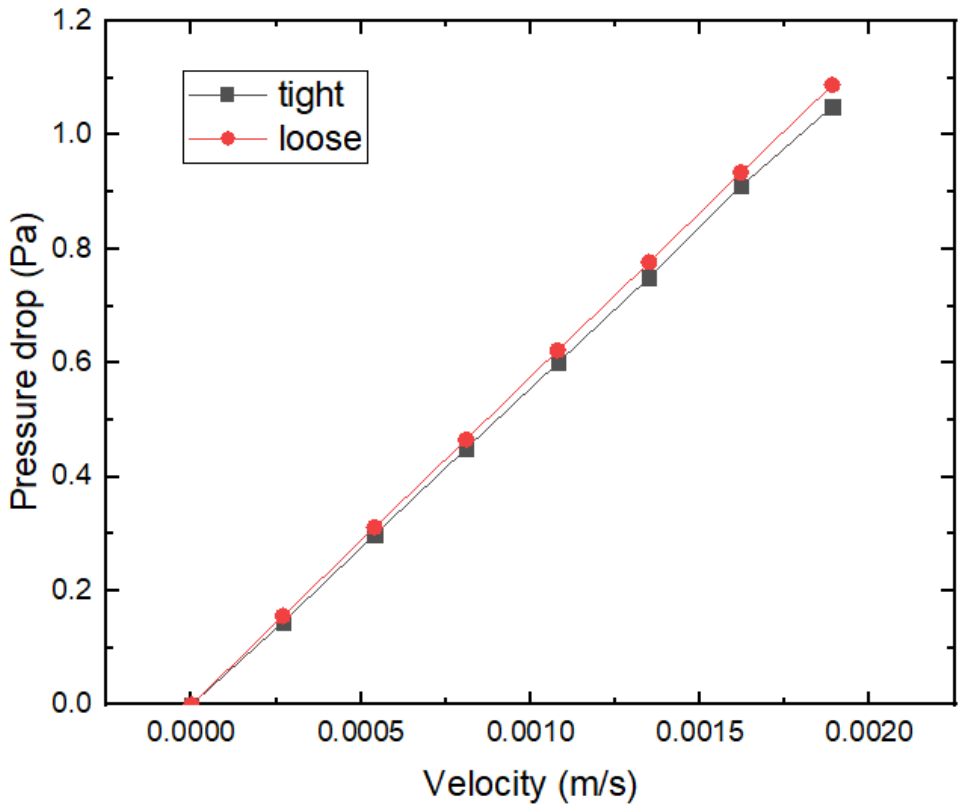

Figure 5-5 The pressure drop as a function of the nitrogen velocity for different contact situations.

5.4 Conclusions

Unlike the previously conducted experiments, the gas permeability experiment for GDL stacks by varying the number of samples is measured. The main conclusions are as follows:

- The stacking of the layers has little influence on the overall gas permeability of the GDL stack. This shows that placing GDL stacks inside fuel cells may be technically feasible.

- Increasing the tightness of the contact between the GDL stacks and the fixtures of the setup may lead to the creation of some damage to the structure of the stacks and consequently result in increasing the gas permeability of the GDL stack.

Chapter 6: Conclusions and future work

Summary

In this chapter, a summary of the conclusions is presented in Section 6.1 and the suggestions for future work are recommended in Section 6.2.

6.1 Conclusions

The AB-PEMFC is an ideal choice to work as batteries in portable applications. The main limitations in this FC are the relative low performance and the water management problem. In this thesis, both experimental and modelling work have been conducted to improve the overall performance of the AB-PEMFC and the local performance of some components employed in the AB-PEMFC. The main conclusions are as follows:

6.1.1 Overall performance of AB-PEMFCs

Unlike conventional PEMFCs, the performance limiting mode of AB-PEMFCs is dictated by the heat transfer coefficient: dry-out of the membrane with relatively low heat transfer coefficient and water flooding with a relatively high heat transfer coefficient.

In addition to the components employed in AB-PEMFCs, the operating condition is found to be closely related to the performance of the AB-PEMFCs. Among the different operating conditions, such as ambient temperature and relative humidity, hydrogen relative humidity is found to be more effective in improving the overall performance of the AB-PEMFC, and this improvement is not influenced by any

other operating conditions. Further, the increase in the hydrogen relative humidity will not cause water flooding at high current densities in the AB-PEMFC.

6.1.2 Flow channels for AB-PEMFCs

In the anode flow channel of the AB-PEMFC, the time taken for the water droplet to move out from the channel and the pressure drop caused are almost insensitive to the initial position, however the dynamics of the droplets is closely related to the initial position. On the contrary, the size of the water droplet is found to have a negligible effect on the water dynamics while it will largely influence the removal time and pressure drop through the channel.

The hydrogen velocity has little influence on the water dynamics in the anode channel, but it will largely change the removal time and the pressure drop through the channel. The decrease of the contact angle of the GDL surface leads to the decrease in the pressure drop in the anode flow channel. However, the removal time for the water droplet increases with decreasing GDL contact angle, and this is because of the strong adhesion forces.

6.1.3 GDLs employed in AB-PEMFCs

The GDL is found to be very important in AB-PEMFCs. In general, there is an optimal thickness for the cathode GDL in order to maintain high concentrations of both oxygen and water vapour at the cathode catalyst layer. While for anode GDLs, the thinner GDLs are preferred to enhance the diffusion of water vapour at the anode and this improvement is more significant when the relative humidity of the hydrogen is higher.

In order to produce the GDLs with different thicknesses, stacking of several GDL layers is a considerable choice. The stacking of the GDL layers has almost no effect on the through-plane permeability of the whole stack. In addition, the permeability of the stack can be slightly increased by employing a more tighter contact between each layer in the stack. These findings show that, in order to produce GDLs with different thicknesses, the use of GDL stacks may be a technically feasible choice.

6.2 Suggestions for future work

There is still a wide gap from the full commercialization of AB-PEMFCs into the markets. The future work for AB-PEMFCs should focus on both the operating conditions and the components for AB-PEMFCs.

6.2.1 The operating condition for AB-PEMFCs

The performance of AB-PEMFCs is largely influenced by the operating condition. Further investigations should consider the combination of the modelling and experimental work under different operating conditions for AB-PEMFCs. Further, system studies on how to control the operating condition for the AB-PEMFCs in real portable devices should be conducted, since this type of fuel cell is very sensitive to the working conditions and the changes in the conditions significantly influences the stability of the AB-PEMFC system.

6.2.2 The components employed in AB-PEMFCs

The increase of hydrogen RH is found to be effective in improving the performance of AB-PEMFCs, and this can be attributed to the improvement of the membrane hydration level at high current densities. In addition to hydrogen RH, other methods

related to the design of the components to improve the water concentration of the membrane in AB-PEMFCs could be investigated. For example, direct liquid injection and pre-treatment of the membrane. In addition, the transport of the produced water from the cathode to the membrane may be a feasible and effective method. This is because it can improve the hydration level of the membrane and solve the flooding problem at the cathode.

List of references

[1] BP's Statistical Review of World Energy 2018, (2018) 1–56. https://www.bp.com/content/dam/bp/business-sites/en/global/corporate/pdfs/energy-economics/statistical-review/bp-stats-review-2018-full-report.pdf.

[2] 2018 BP Energy Outlook, (2018) 125. doi:10.1088/1757-899X/342/1/012091.

[3] N. Bizon, P. Thounthong, Fuel economy using the global optimization of the Fuel Cell Hybrid Power Systems, Energy Convers. Manag. 173 (2018) 665–678. doi:10.1016/j.enconman.2018.08.015.

[4] S. Wang, S.P. Jiang, Prospects of Fuel Cell Technologies, Natl. Sci. Rev. 4 (2017) 163–166. doi:10.1093/nsr/nww099.

[5] Y. Wang, D.Y.C. Leung, J. Xuan, H. Wang, A review on unitized regenerative fuel cell technologies, part-A: Unitized regenerative proton exchange membrane fuel cells, Renew. Sustain. Energy Rev. 65 (2016) 961–977. doi:10.1016/j.rser.2016.07.046.

[6] M.B. Sassin, Y. Garsany, B.D. Gould, K.E. Swider-Lyons, Fabrication Method for Laboratory-Scale High-Performance Membrane Electrode Assemblies for Fuel Cells, Anal. Chem. 89 (2017) 511–518. doi:10.1021/acs.analchem.6b03005.

[7] G. Merle, M. Wessling, K. Nijmeijer, Anion exchange membranes for alkaline fuel cells: A review, J. Memb. Sci. 377 (2011) 1–35. doi:10.1016/j.memsci.2011.04.043.

[8] Z.F. Pan, L. An, T.S. Zhao, Z.K. Tang, Advances and challenges in alkaline anion exchange membrane fuel cells, Prog. Energy Combust. Sci. 66 (2018) 141–175. doi:10.1016/j.pecs.2018.01.001.

[9] Z. Du, H. Li, T. Gu, A state of the art review on microbial fuel cells: A promising technology for wastewater treatment and bioenergy, Biotechnol. Adv. 25 (2007) 464–482. doi:10.1016/j.biotechadv.2007.05.004.

[10] A.J. Slate, K.A. Whitehead, D.A.C. Brownson, C.E. Banks, Microbial fuel cells : An overview of current technology, Renew. Sustain. Energy Rev. 101 (2019) 60–81. doi:10.1016/j.rser.2018.09.044.

[11] S. Singhal, Advances in solid oxide fuel cell technology, Solid State Ionics. 135 (2000) 305–313. doi:10.1016/S0167-2738(00)00452-5.

[12] F. Ramadhani, M.A. Hussain, H. Mokhlis, S. Hajimolana, Optimization strategies for Solid Oxide Fuel Cell (SOFC) application: A literature survey, Renew. Sustain. Energy Rev. 76 (2017) 460–484. doi:10.1016/j.rser.2017.03.052.

[13] N. Mahato, A. Banerjee, A. Gupta, S. Omar, K. Balani, Progress in material selection for solid oxide fuel cell technology: A review, Prog. Mater. Sci. 72 (2015) 141–337. doi:10.1016/j.pmatsci.2015.01.001.

[14] T. Wilberforce, A. Alaswad, A. Palumbo, M. Dassisti, A.G. Olabi, Advances in stationary and portable fuel cell applications, Int. J. Hydrogen Energy. 41 (2016) 16509–16522. doi:10.1016/j.ijhydene.2016.02.057.

[15] G. Upreti, D.L. Greene, K.G. Duleep, R. Sawhney, Fuel cells for non-automotive uses: Status and prospects, Int. J. Hydrogen Energy. 37 (2012) 6339–6348. doi:10.1016/j.ijhydene.2012.01.060.

[16] Z.P. Cano, D. Banham, S. Ye, A. Hintennach, J. Lu, M. Fowler, Z. Chen, Batteries and fuel cells for emerging electric vehicle markets, Nat. Energy. 3 (2018) 279–289. doi:10.1038/s41560-018-0108-1.

[17] S.S. Munjewar, S.B. Thombre, R.K. Mallick, Approaches to overcome the barrier issues of passive direct methanol fuel cell – Review, Renew. Sustain. Energy Rev. 67 (2017) 1087–1104. doi:10.1016/j.rser.2016.09.002.

[18] B.C. Ong, S.K. Kamarudin, S. Basri, Direct liquid fuel cells: A review, Int. J. Hydrogen Energy. 42 (2017) 10142–10157. doi:10.1016/j.ijhydene.2017.01.117.

[19] Y. Jiang, X. Wang, L. Zhong, L. Liu, Design, fabrication and testing of a silicon-based air-breathing micro direct methanol fuel cell, J. Micromechanics Microengineering. 16 (2006). doi:10.1088/0960-1317/16/9/S10.

[20] E. Carcadea, H. Ene, D.B. Ingham, R. Lazar, L. Ma, M. Pourkashanian, I. Stefanescu, A computational fluid dynamics analysis of a PEM fuel cell system for power generation, Int. J. Numer. Methods Heat Fluid Flow. 17 (2007) 302–312. doi:10.1108/09615530710730166.

[21] A. Schmitz, M. Tranitz, S. Eccarius, A. Weil, C. Hebling, Influence of cathode opening size and wetting properties of diffusion layers on the performance of air-breathing PEMFCs, J. Power Sources. 154 (2006) 437–447. doi:10.1016/j.jpowsour.2005.10.070.

[22] T. Mennola, M. Noponen, M. Aronniemi, T. Hottinen, M. Mikkola, O. Himanen, P. Lund, Mass transport in the cathode of a free-breathing polymer electrolyte membrane fuel cell, J. Appl. Electrochem. 33 (2003) 979–987.

doi:10.1023/A:1026279431097.

[23] P. Pei, H. Chen, Main factors affecting the lifetime of Proton Exchange Membrane fuel cells in vehicle applications: A review, Appl. Energy. 125 (2014) 60–75. doi:10.1016/j.apenergy.2014.03.048.

[24] R. Banerjee, S.G. Kandlikar, Two-phase flow and thermal transients in proton exchange membrane fuel cells - A critical review, Int. J. Hydrogen Energy. 40 (2015) 3990–4010. doi:10.1016/j.ijhydene.2015.01.126.

[25] P. Manoj Kumar, V. Parthasarathy, A passive method of water management for an air-breathing proton exchange membrane fuel cell, Energy. 51 (2013) 457–461. doi:10.1016/j.energy.2012.12.015.

[26] A. Schmitz, M. Tranitz, S. Wagner, R. Hahn, C. Hebling, Planar self-breathing fuel cells, J. Power Sources. 118 (2003) 162–171. doi:10.1016/S0378-7753(03)00080-6.

[27] Q. Wu, H. Li, W. Yuan, Z. Luo, F. Wang, H. Sun, X. Zhao, H. Fu, Performance evaluation of an air-breathing high-temperature proton exchange membrane fuel cell, Appl. Energy. 160 (2015) 146–152. doi:10.1016/j.apenergy.2015.09.042.

[28] S.U. Jeong, E.A. Cho, H.J. Kim, T.H. Lim, I.H. Oh, S.H. Kim, Effects of cathode open area and relative humidity on the performance of air-breathing polymer electrolyte membrane fuel cells, J. Power Sources. 158 (2006) 348–353. doi:10.1016/j.jpowsour.2005.09.044.

[29] N. Bussayajarn, H. Ming, K.K. Hoong, W.Y. Ming Stephen, C.S. Hwa, Planar air breathing PEMFC with self-humidifying MEA and open cathode geometry design for portable applications, Int. J. Hydrogen Energy. 34 (2009) 7761–7767. doi:10.1016/j.ijhydene.2009.07.077.

[30] S.H. Kim, H.Y. Cha, C.M. Miesse, J.H. Jang, Y.S. Oh, S.W. Cha, Air-breathing miniature planar stack using the flexible printed circuit board as a current collector, Int. J. Hydrogen Energy. 34 (2009) 459–466. doi:10.1016/j.ijhydene.2008.09.088.

[31] T. Hottinen, O. Himanen, P. Lund, Effect of cathode structure on planar free-breathing PEMFC, J. Power Sources. 138 (2004) 205–210. doi:10.1016/j.jpowsour.2004.06.044.

[32] T. Hottinen, M. Mikkola, P. Lund, Evaluation of planar free-breathing polymer electrolyte membrane fuel cell design, J. Power Sources. 129 (2004) 68–72. doi:10.1016/j.jpowsour.2003.11.012.

[33] T. Fabian, R. O'Hayre, S. Litster, F.B. Prinz, J.G. Santiago, Active water management at the cathode of a planar air-breathing polymer electrolyte

membrane fuel cell using an electroosmotic pump, J. Power Sources. 195 (2010) 3640–3644. doi:10.1016/j.jpowsour.2009.12.025.

[34] T. Fabian, R. O'Hayre, S. Litster, F.B. Prinz, J.G. Santiago, Passive water management at the cathode of a planar air-breathing proton exchange membrane fuel cell, J. Power Sources. 195 (2010) 3201–3206. doi:10.1016/j.jpowsour.2009.12.030.

[35] U. Ho Jung, S. Uk Jeong, K. Tae Park, H. Mee Lee, K. Chun, D. Woong Choi, S.H. Kim, Improvement of water management in air-breathing and air-blowing PEMFC at low temperature using hydrophilic silica nano-particles, Int. J. Hydrogen Energy. 32 (2007) 4459–4465. doi:10.1016/j.ijhydene.2007.05.008.

[36] D. Modroukas, V. Modi, Micromachined silicon structures for free-convection PEM fuel cells, J. Micromechanics Microengineering. 15 (2005). doi:10.1088/0960-1317/15/9/S04.

[37] D.J.L. Brett, S. Atkins, N.P. Brandon, N. Vasileiadis, V. Vesovic, A.R. Kucernak, Membrane resistance and current distribution measurements under various operating conditions in a polymer electrolyte fuel cell, J. Power Sources. 172 (2007) 2–13. doi:10.1016/j.jpowsour.2007.05.071.

[38] M.G. Santarelli, M.F. Torchio, Experimental analysis of the effects of the operating variables on the performance of a single PEMFC, Energy Convers. Manag. 48 (2007) 40–51. doi:10.1016/j.enconman.2006.05.013.

[39] Y. Ahn, F. Zhang, B.E. Logan, Air humidity and water pressure effects on the performance of air-cathode microbial fuel cell cathodes, J. Power Sources. 247 (2014) 655–659. doi:10.1016/j.jpowsour.2013.08.084.

[40] H.Y. Kim, K. Kim, Numerical study on the effects of gas humidity on proton-exchange membrane fuel cell performance, Int. J. Hydrogen Energy. 41 (2016) 11776–11783. doi:10.1016/j.ijhydene.2016.01.075.

[41] L. Xing, Q. Cai, C. Xu, C. Liu, K. Scott, Y. Yan, Numerical study of the effect of relative humidity and stoichiometric flow ratio on PEM (proton exchange membrane) fuel cell performance with various channel lengths: An anode partial flooding modelling, Energy. 106 (2016) 631–645. doi:10.1016/j.energy.2016.03.105.

[42] D.T. Santa Rosa, D.G. Pinto, V.S. Silva, R.A. Silva, C.M. Rangel, High performance PEMFC stack with open-cathode at ambient pressure and temperature conditions, Int. J. Hydrogen Energy. 32 (2007) 4350–4357. doi:10.1016/j.ijhydene.2007.05.042.

[43] T. Fabian, J.D. Posner, R. O'Hayre, S.W. Cha, J.K. Eaton, F.B. Prinz, J.G.

Santiago, The role of ambient conditions on the performance of a planar, air-breathing hydrogen PEM fuel cell, J. Power Sources. 161 (2006) 168–182. doi:10.1016/j.jpowsour.2006.03.054.

[44] A. Bazylak, Liquid water visualization in PEM fuel cells: A review, Int. J. Hydrogen Energy. 34 (2009) 3845–3857. doi:10.1016/j.ijhydene.2009.02.084.

[45] M.I. Rosli, D.J. Borman, D.B. Ingham, M.S. Ismail, L. Ma, M. Pourkashanian, Transparent PEM Fuel Cells for Direct Visualization Experiments, J. Fuel Cell Sci. Technol. 7 (2010) 061015. doi:10.1115/1.4001353.

[46] R.M. Aslam, D.B. Ingham, M.S. Ismail, K.J. Hughes, L. Ma, M. Pourkashanian, Simultaneous thermal and visual imaging of liquid water of the PEM fuel cell flow channels, J. Energy Inst. (2018) 1–8. doi:10.1016/j.joei.2018.01.005.

[47] T. Ous, C. Arcoumanis, The formation of water droplets in an air-breathing PEMFC, Int. J. Hydrogen Energy. 34 (2009) 3476–3487. doi:10.1016/j.ijhydene.2009.02.037.

[48] P. Deevanhxay, T. Sasabe, S. Tsushima, S. Hirai, Observation of dynamic liquid water transport in the microporous layer and gas diffusion layer of an operating PEM fuel cell by high-resolution soft X-ray radiography, J. Power Sources. 230 (2013) 38–43. doi:10.1016/j.jpowsour.2012.11.140.

[49] P.K. Sinha, P. Halleck, C.-Y. Wang, Quantification of Liquid Water Saturation in a PEM Fuel Cell Diffusion Medium Using X-ray Microtomography, Electrochem. Solid-State Lett. 9 (2006) A344. doi:10.1149/1.2203307.

[50] A. Pfrang, D. Veyret, F. Sieker, G. Tsotridis, X-ray computed tomography of gas diffusion layers of PEM fuel cells: Calculation of thermal conductivity, Int. J. Hydrogen Energy. 35 (2010) 3751–3757. doi:10.1016/j.ijhydene.2010.01.085.

[51] Z. Dunbar, R.I. Masel, Quantitative MRI study of water distribution during operation of a PEM fuel cell using Teflon®flow fields, J. Power Sources. 171 (2007) 678–687. doi:10.1016/j.jpowsour.2007.06.207.

[52] R. Satija, D.L. Jacobson, M. Arif, S.A. Werner, In situ neutron imaging technique for evaluation of water management systems in operating PEM fuel cells, J. Power Sources. 129 (2004) 238–245. doi:10.1016/j.jpowsour.2003.11.068.

[53] J.P. Owejan, T.A. Trabold, D.L. Jacobson, M. Arif, S.G. Kandlikar, Effects

of flow field and diffusion layer properties on water accumulation in a PEM fuel cell, Int. J. Hydrogen Energy. 32 (2007) 4489–4502. doi:10.1016/j.ijhydene.2007.05.044.

[54] E. Coz, J. Théry, P. Boillat, V. Faucheux, D. Alincant, P. Capron, G. Gébel, Water management in a planar air-breathing fuel cell array using operando neutron imaging, J. Power Sources. 331 (2016) 535–543. doi:10.1016/j.jpowsour.2016.09.041.

[55] Y. Wang, C.-Y. Wang, A Nonisothermal, Two-Phase Model for Polymer Electrolyte Fuel Cells, J. Electrochem. Soc. 153 (2006) A1193. doi:10.1149/1.2193403.

[56] U. Pasaogullari, P.P. Mukherjee, C.-Y. Wang, K.S. Chen, Anisotropic Heat and Water Transport in a PEFC Cathode Gas Diffusion Layer, J. Electrochem. Soc. 154 (2007) B823. doi:10.1149/1.2745714.

[57] S. Mazumder, J.V. Cole, Rigorous 3-D Mathematical Modeling of PEM Fuel Cells, J. Electrochem. Soc. 150 (2003) A1503. doi:10.1149/1.1615609.

[58] E. Birgersson, M. Noponen, M. Vynnycky, Analysis of a Two-Phase Non-Isothermal Model for a PEFC, J. Electrochem. Soc. 152 (2005) A1021. doi:10.1149/1.1877992.

[59] R.B. Ferreira, D.S. Falcão, V.B. Oliveira, A.M.F.R. Pinto, Numerical simulations of two-phase flow in proton exchange membrane fuel cells using the volume of fluid method – A review, J. Power Sources. 277 (2015) 329–342. doi:10.1016/j.jpowsour.2014.11.124.

[60] J.U. Brackbill, D.B. Kothe, ScienceDirect - Journal of Computational Physics : A continuum method for modeling surface tension, J. Comput. Phys. 335354 (1992). doi:10.1016/0021-9991(92)90240-Y.

[61] K. Jiao, B. Zhou, P. Quan, Liquid water transport in straight micro-parallel-channels with manifolds for PEM fuel cell cathode, J. Power Sources. 157 (2006) 226–243. doi:10.1016/j.jpowsour.2005.06.041.

[62] S. Ge, C.-Y. Wang, Liquid Water Formation and Transport in the PEFC Anode, J. Electrochem. Soc. 154 (2007) B998. doi:10.1149/1.2761830.

[63] A.D. Le, B. Zhou, A general model of proton exchange membrane fuel cell, J. Power Sources. 182 (2008) 197–222. doi:10.1016/j.jpowsour.2008.03.047.

[64] C. Fang, C. Hidrovo, F. min Wang, J. Eaton, K. Goodson, 3-D numerical simulation of contact angle hysteresis for microscale two phase flow, Int. J. Multiph. Flow. 34 (2008) 690–705. doi:10.1016/j.ijmultiphaseflow.2007.08.008.

[65] M. Andersson, S.B. Beale, U. Reimer, W. Lehnert, D. Stolten, Interface resolving two-phase flow simulations in gas channels relevant for polymer electrolyte fuel cells using the volume of fluid approach, Int. J. Hydrogen Energy. 43 (2018) 2961–2976. doi:10.1016/j.ijhydene.2017.12.129.

[66] A. Theodorakakos, T. Ous, M. Gavaises, J.M. Nouri, N. Nikolopoulos, H. Yanagihara, Dynamics of water droplets detached from porous surfaces of relevance to PEM fuel cells, J. Colloid Interface Sci. 300 (2006) 673–687. doi:10.1016/j.jcis.2006.04.021.

[67] P. Quan, B. Zhou, A. Sobiesiak, Z. Liu, Water behavior in serpentine micro-channel for proton exchange membrane fuel cell cathode, J. Power Sources. 152 (2005) 131–145. doi:10.1016/j.jpowsour.2005.02.075.

[68] J.G. Carton, V. Lawlor, A.G. Olabi, C. Hochenauer, G. Zauner, Water droplet accumulation and motion in PEM (Proton Exchange Membrane) fuel cell mini-channels, Energy. 39 (2012) 63–73. doi:10.1016/j.energy.2011.10.023.

[69] A. Bozorgnezhad, M. Shams, H. Kanani, M. Hasheminasab, G. Ahmadi, Two-phase flow and droplet behavior in microchannels of PEM fuel cell, Int. J. Hydrogen Energy. 41 (2016) 19164–19181. doi:10.1016/j.ijhydene.2016.09.043.

[70] A. Bazylak, D. Sinton, N. Djilali, Dynamic water transport and droplet emergence in PEMFC gas diffusion layers, J. Power Sources. 176 (2008) 240–246. doi:10.1016/j.jpowsour.2007.10.066.

[71] Y. Ding, X. Bi, D.P. Wilkinson, 3D simulations of the impact of two-phase flow on PEM fuel cell performance, Chem. Eng. Sci. 100 (2013) 445–455. doi:10.1016/j.ces.2012.11.007.

[72] A.D. Le, B. Zhou, A generalized numerical model for liquid water in a proton exchange membrane fuel cell with interdigitated design, J. Power Sources. 193 (2009) 665–683. doi:10.1016/j.jpowsour.2009.04.011.

[73] A.D. Le, B. Zhou, Fundamental understanding of liquid water effects on the performance of a PEMFC with serpentine-parallel channels, Electrochim. Acta. 54 (2009) 2137–2154. doi:10.1016/j.electacta.2008.10.029.

[74] L. Chen, T.F. Cao, Z.H. Li, Y.L. He, W.Q. Tao, Numerical investigation of liquid water distribution in the cathode side of proton exchange membrane fuel cell and its effects on cell performance, Int. J. Hydrogen Energy. 37 (2012) 9155–9170. doi:10.1016/j.ijhydene.2012.01.101.

[75] R.B. Ferreira, D.S. Falcão, V.B. Oliveira, A.M.F.R. Pinto, 1D + 3D two-phase flow numerical model of a proton exchange membrane fuel cell, Appl.

Energy. 203 (2017) 474–495. doi:10.1016/j.apenergy.2017.06.048.

[76] R. Omrani, B. Shabani, Gas diffusion layer modifications and treatments for improving the performance of proton exchange membrane fuel cells and electrolysers: A review, Int. J. Hydrogen Energy. 42 (2017) 28515–28536. doi:10.1016/j.ijhydene.2017.09.132.

[77] O.M. Orogbemi, D.B. Ingham, M.S. Ismail, K.J. Hughes, L. Ma, M. Pourkashanian, The effects of the composition of microporous layers on the permeability of gas diffusion layers used in polymer electrolyte fuel cells, Int. J. Hydrogen Energy. 41 (2016) 21345–21351. doi:10.1016/j.ijhydene.2016.09.160.

[78] H. Gharibi, M. Javaheri, R.A. Mirzaie, The synergy between multi-wall carbon nanotubes and Vulcan XC72R in microporous layers, Int. J. Hydrogen Energy. 35 (2010) 9241–9251. doi:10.1016/j.ijhydene.2009.08.092.

[79] M. Hunsom, P. Piumsomboon, K. Pruksathorn, N. Tantavichet, S. Endoo, K. Charutavai, K. Poochinda, Novel application of Hicon Black in PEMFC microporous sublayer: Effects of composition and subsequent membrane selection, Renew. Energy. 36 (2011) 369–373. doi:10.1016/j.renene.2010.07.002.

[80] N. Hussain, E. Van Steen, S. Tanaka, P. Levecque, Metal based gas diffusion layers for enhanced fuel cell performance at high current densities, J. Power Sources. 337 (2017) 18–24. doi:10.1016/j.jpowsour.2016.11.001.

[81] F.Y. Zhang, S.G. Advani, A.K. Prasad, Performance of a metallic gas diffusion layer for PEM fuel cells, J. Power Sources. 176 (2008) 293–298. doi:10.1016/j.jpowsour.2007.10.055.

[82] J.H. Chun, D.H. Jo, S.G. Kim, S.H. Park, C.H. Lee, E.S. Lee, J.Y. Jyoung, S.H. Kim, Development of a porosity-graded micro porous layer using thermal expandable graphite for proton exchange membrane fuel cells, Renew. Energy. 58 (2013) 28–33. doi:10.1016/j.renene.2013.02.025.

[83] T. Tanuma, M. Kawamoto, S. Kinoshita, Effect of Properties of Hydrophilic Microporous Layer (MPL) on PEFC Performance, J. Electrochem. Soc. 164 (2017) F499–F503. doi:10.1149/2.0371706jes.

[84] K. Nishida, T. Murakami, S. Tsushima, S. Hirai, Measurement of liquid water content in cathode gas diffusion electrode of polymer electrolyte fuel cell, J. Power Sources. 195 (2010) 3365–3373. doi:10.1016/j.jpowsour.2009.12.073.

[85] Y. Wang, L. Wang, S.G. Advani, A.K. Prasad, Double-layer gas diffusion

media for improved water management in polymer electrolyte membrane fuel cells, J. Power Sources. 292 (2015) 39–48. doi:10.1016/j.jpowsour.2015.05.028.

[86] H. Oh, J. Park, K. Min, E. Lee, J.Y. Jyoung, Effects of pore size gradient in the substrate of a gas diffusion layer on the performance of a proton exchange membrane fuel cell, Appl. Energy. 149 (2015) 186–193. doi:10.1016/j.apenergy.2015.03.072.

[87] J.H. Chun, K.T. Park, D.H. Jo, J.Y. Lee, S.G. Kim, S.H. Park, E.S. Lee, J.Y. Jyoung, S.H. Kim, Development of a novel hydrophobic/hydrophilic double micro porous layer for use in a cathode gas diffusion layer in PEMFC, Int. J. Hydrogen Energy. 36 (2011) 8422–8428. doi:10.1016/j.ijhydene.2011.04.038.

[88] P. Shrestha, R. Banerjee, J. Lee, N. Ge, D. Muirhead, H. Liu, A.K.C. Wong, D. Ouellette, B. Zhao, A. Bazylak, Hydrophilic microporous layer coatings for polymer electrolyte membrane fuel cells operating without anode humidification, J. Power Sources. 402 (2018) 468–482. doi:10.1016/j.jpowsour.2018.08.062.

[89] F.B. Weng, C.Y. Hsu, M.C. Su, Experimental study of micro-porous layers for PEMFC with gradient hydrophobicity under various humidity conditions, Int. J. Hydrogen Energy. 36 (2011) 13708–13714. doi:10.1016/j.ijhydene.2011.07.141.

[90] Y. Zhang, A. Mawardi, R. Pitchumani, Numerical studies on an air-breathing proton exchange membrane (PEM) fuel cell stack, J. Power Sources. 173 (2007) 264–276. doi:10.1016/j.jpowsour.2007.05.008.

[91] D. Chu, R. Jiang, Performance of polymer electrolyte membrane fuel cell (PEMFC) stacks Part I. Evaluation and simulation of an air-breathing PEMFC stack, J. Power Sources. 83 (1999) 128–133. doi:10.1016/S0378-7753(99)00285-2.

[92] S. Hamel, L.G. Fréchette, Critical importance of humidification of the anode in miniature air-breathing polymer electrolyte membrane fuel cells, J. Power Sources. 196 (2011) 6242–6248. doi:10.1016/j.jpowsour.2011.04.020.

[93] K. Ou, W.W. Yuan, M. Choi, S. Yang, Y.B. Kim, Performance increase for an open-cathode PEM fuel cell with humidity and temperature control, Int. J. Hydrogen Energy. 42 (2017) 29852–29862. doi:10.1016/j.ijhydene.2017.10.087.

[94] R. O'Hayre, T. Fabian, S. Litster, F.B. Prinz, J.G. Santiago, Engineering model of a passive planar air breathing fuel cell cathode, J. Power Sources. 167 (2007) 118–129. doi:10.1016/j.jpowsour.2007.01.073.

[95] M.S. Ismail, D.B. Ingham, K.J. Hughes, L. Ma, M. Pourkashanian, An efficient mathematical model for air-breathing PEM fuel cells, Appl. Energy. 135 (2014) 490–503. doi:10.1016/j.apenergy.2014.08.113.

[96] M. Ghiaasiaan, Convective Heat and Mass Transfer, Cambridge University Press, Cambridge, 2011. doi:10.1017/CBO9780511800603.

[97] T.E. Springer, Polymer Electrolyte Fuel Cell Model, J. Electrochem. Soc. 138 (1991) 2334. doi:10.1149/1.2085971.

[98] M.M. Mench, ed., Fuel Cell Engines, John Wiley & Sons, Inc., Hoboken, NJ, USA, 2008. doi:10.1002/9780470209769.

[99] M.S. Ismail, D.B. Ingham, K.J. Hughes, L. Ma, M. Pourkashanian, Effective diffusivity of polymer electrolyte fuel cell gas diffusion layers: An overview and numerical study, Int. J. Hydrogen Energy. 40 (2015) 10994–11010. doi:10.1016/j.ijhydene.2015.06.073.

[100] L. Karpenko-Jereb, P. Innerwinkler, A.M. Kelterer, C. Sternig, C. Fink, P. Prenninger, R. Tatschl, A novel membrane transport model for polymer electrolyte fuel cell simulations, Int. J. Hydrogen Energy. 39 (2014) 7077–7088. doi:10.1016/j.ijhydene.2014.02.083.

[101] K. Jiao, X. Li, Water transport in polymer electrolyte membrane fuel cells, Prog. Energy Combust. Sci. 37 (2011) 221–291. doi:10.1016/j.pecs.2010.06.002.

[102] P. Berg, K. Promislow, J. St. Pierre, J. Stumper, B. Wetton, Water Management in PEM Fuel Cells, J. Electrochem. Soc. 151 (2004) A341. doi:10.1149/1.1641033.

[103] T.L. Bergman, A.S. Lavine, F.P. Incropera, D.P. DeWitt, Introduction to Heat Transfer, John Wiley & Sons, Inc., New York, 2011.

[104] S. Litster, N. Djilali, Mathematical modelling of ambient air-breathing fuel cells for portable devices, Electrochim. Acta. 52 (2007) 3849–3862. doi:10.1016/j.electacta.2006.11.002.

[105] F.A. Schwertz, J.E. Brow, Diffusivity of water vapor in some common gases, J. Chem. Phys. 19 (1951) 640–646. doi:10.1063/1.1748306.

[106] R.W. Atkinson, M.W. Hazard, J.A. Rodgers, R.O. Stroman, B.D. Gould, An Open-Cathode Fuel Cell for Atmospheric Flight, J. Electrochem. Soc. 164 (2017) F46–F54. doi:10.1149/2.0261702jes.

[107] O.A. Obeisun, Q. Meyer, E. Engebretsen, D.P. Finegan, J.B. Robinson, G. Hinds, P.R. Shearing, D.J.L. Brett, Study of water accumulation dynamics in the channels of an open-cathode fuel cell through electro-thermal

characterisation and droplet visualisation, Int. J. Hydrogen Energy. 40 (2015) 16786–16796. doi:10.1016/j.ijhydene.2015.07.066.

[108] B. Chen, J. Wang, T. Yang, Y. Cai, C. Zhang, S.H. Chan, Y. Yu, Z. Tu, Carbon corrosion and performance degradation mechanism in a proton exchange membrane fuel cell with dead-ended anode and cathode, Energy. 106 (2016) 54–62. doi:10.1016/j.energy.2016.03.045.

[109] J.M. Sergi, S.G. Kandlikar, Quantification and characterization of water coverage in PEMFC gas channels using simultaneous anode and cathode visualization and image processing, Int. J. Hydrogen Energy. 36 (2011) 12381–12392. doi:10.1016/j.ijhydene.2011.06.092.

[110] J. O'Rourke, M. Ramani, M. Arcak, In situ detection of anode flooding of a PEM fuel cell, Int. J. Hydrogen Energy. 34 (2009) 6765–6770. doi:10.1016/j.ijhydene.2009.06.029.

[111] W. Schmittinger, A. Vahidi, A review of the main parameters influencing long-term performance and durability of PEM fuel cells, J. Power Sources. 180 (2008) 1–14. doi:10.1016/j.jpowsour.2008.01.070.

[112] D. Lee, J. Bae, Visualization of flooding in a single cell and stacks by using a newly-designed transparent PEMFC, Int. J. Hydrogen Energy. 37 (2012) 422–435. doi:10.1016/j.ijhydene.2011.09.073.

[113] R.B. Ferreira, D.S. Falcão, V.B. Oliveira, A.M.F.R. Pinto, Numerical simulations of two-phase flow in an anode gas channel of a proton exchange membrane fuel cell, Energy. 82 (2015) 619–628. doi:10.1016/j.energy.2015.01.071.

[114] Y. Hou, G. Zhang, Y. Qin, Q. Du, K. Jiao, Numerical simulation of gas liquid two-phase flow in anode channel of low-temperature fuel cells, Int. J. Hydrogen Energy. 42 (2017) 3250–3258. doi:10.1016/j.ijhydene.2016.09.219.

[115] Y. Cai, T. Yang, P.C. Sui, J. Xiao, A numerical investigation on the effects of water inlet location and channel surface properties on water transport in PEMFC cathode channels, Int. J. Hydrogen Energy. 41 (2016) 16220–16229. doi:10.1016/j.ijhydene.2016.04.241.

[116] J.T. Gostick, M.W. Fowler, M.D. Pritzker, M.A. Ioannidis, L.M. Behra, In-plane and through-plane gas permeability of carbon fiber electrode backing layers, J. Power Sources. 162 (2006) 228–238. doi:10.1016/j.jpowsour.2006.06.096.

[117] M.S. Ismail, T. Damjanovic, D.B. Ingham, L. Ma, M. Pourkashanian, Effect of polytetrafluoroethylene-treatment and microporous layer-coating on the

in-plane permeability of gas diffusion layers used in proton exchange membrane fuel cells, J. Power Sources. 195 (2010) 6619–6628. doi:10.1016/j.jpowsour.2010.04.036.

[118] R. Flückiger, S.A. Freunberger, D. Kramer, A. Wokaun, G.G. Scherer, F.N. Büchi, Anisotropic, effective diffusivity of porous gas diffusion layer materials for PEFC, Electrochim. Acta. 54 (2008) 551–559. doi:10.1016/j.electacta.2008.07.034.

[119] M.S. Ismail, T. Damjanovic, K. Hughes, D.B. Ingham, L. Ma, M. Pourkashanian, M. Rosli, Through-Plane Permeability for Untreated and PTFE-Treated Gas Diffusion Layers in Proton Exchange Membrane Fuel Cells, J. Fuel Cell Sci. Technol. 7 (2010) 051016. doi:10.1115/1.4000685.

[120] O.M. Orogbemi, D.B. Ingham, M.S. Ismail, K.J. Hughes, L. Ma, M. Pourkashanian, Through-plane gas permeability of gas diffusion layers and microporous layer: Effects of carbon loading and sintering, J. Energy Inst. 91 (2018) 270–278. doi:10.1016/j.joei.2016.11.008.

[121] A. Tamayol, M. Bahrami, In-Plane Gas Permeability of Proton Exchange Membrane Fuel Cell Gas Diffusion Layers, in: ASME 2010 3rd Jt. US-European Fluids Eng. Summer Meet. Vol. 1, Symp. – Parts A, B, C, ASME, 2010: pp. 1241–1248. doi:10.1115/FEDSM-ICNMM2010-30563.

[122] D. Shou, Y. Tang, L. Ye, J. Fan, F. Ding, Effective permeability of gas diffusion layer in proton exchange membrane fuel cells, Int. J. Hydrogen Energy. 38 (2013) 10519–10526. doi:10.1016/j.ijhydene.2013.06.043.

[123] A. Wong, A. Bazylak, Investigating the Effect of Non-Uniform Microporous Layer Intrusion on Oxygen Transport in Dry and Partially Saturated Polymer Electrolyte Membrane Fuel Cell Gas Diffusion Layers, ECS Trans. 80 (2017) 175–186. doi:10.1149/08008.0175ecst.

[124] N. Zamel, X. Li, Effective transport properties for polymer electrolyte membrane fuel cells - With a focus on the gas diffusion layer, Prog. Energy Combust. Sci. 39 (2013) 111–146. doi:10.1016/j.pecs.2012.07.002.

[125] N. Zamel, J. Becker, A. Wiegmann, Estimating the thermal conductivity and diffusion coefficient of the microporous layer of polymer electrolyte membrane fuel cells, J. Power Sources. 207 (2012) 70–80. doi:10.1016/j.jpowsour.2012.02.003.